

Deformation and Fracture of Tough Microstructured Hydrogels

Présentée le 25 novembre 2022

à la Faculté des sciences et techniques de l'ingénieur
Laboratoire de la matière molle
Programme doctoral en science et génie des matériaux

pour l'obtention du grade de Docteur ès Sciences

par

Michael David KESSLER

Acceptée sur proposition du jury

Prof. P. Bowen, président du jury
Prof. E. Amstad, directrice de thèse
Prof. N. Holten-Andersen, rapporteur
Dr R. Style, rapporteur
Prof. J. Kolinski, rapporteur

Acknowledgments

I would like to thank many warm-hearted people I've encountered during my PhD, whereby the list will surely remain incomplete.

First of all, thank you Esther Amstad, my supervisor, for your warm welcome in the SMaL lab. I am very glad for the respectful working environment that you have fostered, you were extremely supportive and motivational! The lab is well organized, which tremendously simplified my life and allowed me to focus on my research.

A big share of the friendly environment in SMaL is also due to Mercedes Quintas, who was very responsive and quickly helping me out when I had some administrative inquiries. Thank you also for the many friendly chats we've had!

I would like to thank the whole SMaL crew, which made my stay in the lab fun, stimulating and enriching, including Gianluca, Antoine, Du, Mathias, Aysu, Alvaro, Matteo, Alex, Gaia, Ran, Pauline, Chuen-Ru, Eva, Francesca, Tianyu, Lorenzo, Rocio, and all other members of the lab. I would also like to thank all my students, especially Quentin, Isabelle, Marine, and Constance, I've learned a lot from you!

I've had the pleasure to collaborate with few people outside of SMaL, including François, Hervé, John, Chenzhuo, Selman, Ken, Rob, Alice, Stephen, Derek, Véronique, thank you so much for broadening my horizon!

I would like to thank the jury members of the private defense John, Rob and Niels for a stimulating discussion and for pushing my limits, I've enjoyed it very much!

A big thank you to my Lausanne friends that made my stay here unforgettable, including Garbo, Félix, Noaf, Eva, Nico, Niko, Bärni, Martin, Bernardo, Zander, Luca, Claire, Sybille, Joey, Greg, and many more!

Thanks also to my Bern friends Simon, Manuel, Lukas, Simon, Max, and Kevin for your everlasting friendship and for distracting me from my PhD during holidays and parties!

Last but not least, I would like to thank my parents Stephan and Cécile and my sister Laura for your endless and unconditional support, I would not have been able to do what I did without you!

Abstract

Many natural materials are structured on different length scales. This structuring often leads to an intricate interplay between soft and stiff components, which significantly improves the fracture energy of these materials. A class of soft material that is frequently employed by natural organisms as load-bearing elements, such as tendons, are hydrogels. These are polymeric materials that are swollen with large amounts of water. However, in contrast to their natural counterparts, synthetic hydrogels often suffer from intrinsic tradeoffs between mechanical properties, such as stiffness and toughness. These limitations hamper the use of hydrogels for more advanced applications, for example in soft robotics or biomedical engineering. The current weaknesses of synthetic hydrogels are, to a big share, related to their homogeneous structure. A promising, bio-inspired route to design tough and load-bearing synthetic hydrogels is hence to introduce microstructures into them.

In this dissertation, I investigate how the microstructure of bulk hydrogels that are reinforced with hydrogel microparticles, microgels, influences their ability to resist deformation and fracture. I show that the fracture energy of microgel-reinforced hydrogels (MRHs) is independent of the size of reinforcing microgels, and only depends on their effective volume fraction regardless of their degree of swelling. In contrast, the stress at break of MRHs is dependent on the microgel-size. I demonstrate that the microstructure in soft and tough materials is key to improve their stiffness and work of extension. To precisely control this important parameter, I present a microfluidic trapping device that allows to introduce abrupt local compositional changes into thin hydrogel sheets on the 100 μm length scale.

I believe that the field of soft materials will strongly benefit from the insights gained in this thesis to develop stiffer and tougher soft materials by introducing microstructures into them, which will likely open up new applications in the fields of biomedical science and soft robotics. Further, the introduction of abrupt, local compositional variations into soft materials likely enables the development of advanced soft actuators, electrical switches or hydrogel batteries.

In summary, I show that the microstructure of soft, tough materials is an important design parameter to improve their stiffness and strength, and introduce a microfluidic device to precisely control it.

Keywords: *hydrogels, mechanics of soft materials, microgel-reinforced hydrogels, microfluidics*

Zusammenfassung

Viele natürliche Materialien sind auf verschiedenen Längenskalen strukturiert. Diese Strukturierung führt oft zu einem ausgeklügelten Wechselspiel zwischen weichen und steifen Komponenten, was die Bruchzähigkeit dieser Materialien erheblich verbessert. Eine Klasse weicher Materialien, die von natürlichen Organismen häufig als tragende Elemente, wie z. B. Sehnen, verwendet wird, sind Hydrogele. Dabei handelt es sich um Polymermaterialien, die mit großen Mengen an Wasser geschwollen sind. Im Gegensatz zu ihren natürlichen Vorbildern leiden synthetische Hydrogele jedoch häufig unter einem inhärenten Kompromiss zwischen mechanischen Eigenschaften wie Steifigkeit und Zähigkeit. Diese Einschränkungen verhindern den Einsatz von Hydrogelen für anspruchsvollere Anwendungen, zum Beispiel in der Weichrobotertechnik oder der Biomedizintechnik. Die derzeitigen Schwächen synthetischer Hydrogele hängen zu einem großen Teil mit ihrer homogenen Struktur zusammen. Ein vielversprechender, von der Biologie inspirierter Weg, um zähe und belastbare synthetische Hydrogele zu entwickeln, besteht daher darin, Mikrostrukturen in sie einzuarbeiten.

In dieser Dissertation untersuche ich, wie die Mikrostruktur von Hydrogelen, die mit Hydrogel-Mikropartikeln (Mikrogelen) verstärkt sind, deren Steifigkeit und Bruchfestigkeit beeinflusst. Ich zeige, dass die Bruchzähigkeit von mikrogelverstärkten Hydrogelen (MRHs) nicht von der Größe der verstärkenden Mikrogele abhängt, sondern nur von ihrem effektiven Volumenanteil, unabhängig von ihrem Schwellungsgrad. Im Gegensatz dazu ist die Bruchspannung von MRHs von der Mikrogelgröße abhängig. Ich zeige, dass die Mikrostruktur in weichen und zähen Materialien ein wesentlicher Faktor zur Verbesserung ihrer Steifigkeit und Dehnungsarbeit ist. Um diesen wichtigen Parameter präzise zu kontrollieren, stelle ich ein mikrofluidisches System vor, mit dem sich die Zusammensetzung von dünnen Hydrogelschichten auf einer Längenskala von 100 μm abrupt ändern lässt.

Ich glaube, dass der Forschungsbereich der weichen Materialien stark von den in dieser Arbeit gewonnenen Erkenntnissen profitieren wird, um steifere und zähere weiche Materialien durch die Einführung von Mikrostrukturen zu entwickeln, was voraussichtlich neue Anwendungen in den Bereichen der Biomedizin und der Weichrobotertechnik ermöglichen wird. Darüber hinaus ermöglicht die Einführung abrupter, lokaler Zusammensetzungsvariationen in weiche Materialien wahrscheinlich die Entwicklung fortschrittlicher weicher Aktuatoren, elektrischer Schalter oder Hydrogel-Batterien.

Zusammenfassend zeige ich, dass die Mikrostruktur weicher, zäher Materialien ein wichtiger Gestaltungsparameter ist, um ihre Steifigkeit und Zähigkeit zu verbessern, und stelle ein mikrofluidisches Gerät vor, mit dem sich diese Struktur präzise steuern lässt.

Schlüsselwörter: *Hydrogele, Mechanik weicher Materialien, Mikrogel-verstärkte Hydrogele, Mikrofluidik*

Résumé

De nombreux matériaux naturels sont structurés à différentes échelles de longueur. Cette structuration entraîne souvent une interaction sophistiquée entre les composants souples et rigides, ce qui améliore considérablement la résistance à la rupture de ces matériaux. Les hydrogels constituent une classe de matériaux souples souvent utilisés par les organismes naturels comme éléments porteurs, tels que les tendons. Il s'agit de matériaux polymères gonflés par de grandes quantités d'eau. Cependant, contrairement à leurs modèles naturels, les hydrogels synthétiques souffrent souvent d'un compromis inhérent entre les propriétés mécaniques telles que la rigidité et la ténacité. Ces limitations empêchent l'utilisation d'hydrogels pour des applications plus exigeantes, par exemple dans la robotique souple ou le génie biomédical. Les faiblesses actuelles des hydrogels synthétiques sont en grande partie liées à leur structure homogène. Une voie prometteuse, inspirée de la biologie, pour développer des hydrogels synthétiques rigides et tenaces consiste donc à y incorporer des microstructures.

Dans cette thèse, j'étudie comment la microstructure des hydrogels renforcés par des microparticules d'hydrogel (microgels) affecte leur rigidité et leur résistance à la rupture. Je montre que la résistance à la rupture des hydrogels renforcés par des microgels (MRHs) ne dépend pas de la taille des microgels de renforcement, mais uniquement de leur fraction volumique effective, indépendamment de leur degré de gonflement. En revanche, la contrainte de rupture des MRHs dépend de la taille des microgels. Je montre que la microstructure dans les matériaux souples et tenaces est un facteur essentiel pour améliorer leur rigidité et leur travail de déformation. Pour contrôler précisément ce paramètre important, je présente un système microfluidique qui permet de modifier abruptement la composition de couches minces d'hydrogel sur une échelle de longueur de 100 μm .

Je pense que le domaine de recherche des matériaux souples bénéficiera grandement des connaissances acquises dans ce travail pour développer des matériaux souples plus rigides et plus tenaces grâce à l'introduction de microstructures, ce qui permettra vraisemblablement de nouvelles applications dans les domaines du biomédical et de la robotique souple. De plus, l'introduction de variations locales et abruptes de la composition dans les matériaux souples permettra probablement de développer des actionneurs souples avancés, des interrupteurs électriques souples ou des piles à base d'hydrogel.

En conclusion, je montre que la microstructure des matériaux mous et tenaces est un paramètre de conception important pour améliorer leur rigidité et leur ténacité, et je présente un appareil microfluidique qui permet de contrôler précisément cette structure.

Mots clés : *hydrogels, mécanique des matériaux souples, hydrogels renforcés par des microgels, microfluidique*

Contents

Acknowledgments	1
Abstract	2
Zusammenfassung	3
Résumé	4
Contents.....	5
Chapter 1: Introduction.....	9
1.1 The Intrinsic Limitations of Conventional Hydrogels.....	9
1.2 Designed Hydrogel Networks	11
1.2.1 Ideal Networks & Sliding Crosslink Networks for Strong Hydrogels	11
1.2.2 Multimodal Polymer Networks	12
1.3 Energy Dissipation in Double Network Gels	16
1.4 Fracture Mechanics of Soft and Tough Solids	19
1.4.1 Nonlinear Strain Fields During Fracture of Tough Materials	19
1.4.2 Nonlinear Elastic and Dissipative Length Scales	19
1.4.3 Intrinsic and Dissipative Fracture energy	21
1.5 Fracture of Double Network Hydrogels.....	22
1.5.1 Damage Zone in Double Network Hydrogels	22
1.6 Microstructured Hydrogels.....	23
1.6.1 Bio-Inspired Microstructuring of Hydrogels	23
1.6.2 Molding for Bio-Inspired Wet Adhesion	24
1.6.3 Photolithography for Plant-Inspired Patterned Self-Shaping Materials.....	25
1.6.4 Patterning using Physical Properties of Liquids.....	27
1.6.5 Patterning via 3D Printing.....	28
1.7 Compartmentalization to Fabricate Microstructured Hydrogels	29
1.7.1 Inspiration from the Mussel Byssus.....	29

1.7.2 Processing of the Mussel Byssus	30
1.7.3 Microgels as Building Blocks	31
1.7.4 Fabrication of Microgels	32
1.7.5 Assembly of Microgels	33
1.8 Mechanics of Tough, Microgel-Reinforced Hydrogels	34
1.9 Applications of Engineered Hydrogels	35
Chapter 2: Scope of the Dissertation	37
Structure of the Dissertation	37
Chapter 3: Does the Size of Microgels Influence the Toughness of Microgel-Reinforced Hydrogels?	38
3.1 Abstract	40
3.2 Introduction	40
3.3 Experimental Section	42
3.3.1 Microfluidic Device Fabrication	42
3.3.2 Microgel Production	42
3.3.3 Microgel Characterization	42
3.3.4 Microgel Swelling	43
3.3.5 Fabrication of Microgel-Reinforced Hydrogels (MRHs)	43
3.3.6 Microgel Volume Fraction Measurements	43
3.3.7 Tensile Testing	43
3.3.8 Bulk Swelling Measurements	44
3.3.9 Rheological Measurements	44
3.4 Results and Discussion	45
3.4.1 Fabrication of Microgel-Reinforced Hydrogels (MRHs)	45
3.4.2 Microgel Volume Fraction	46
3.4.3 Processing of Microgel-Loaded Precursor Solutions into MRHs	48
3.4.4 Mechanical Properties of MRHs	50
3.4.5 Toughening of MRHs	54
3.4.6 Influence of Microgel Size on Energy Dissipation in MRHs	56

3.5 Conclusion	59
Chapter 4: The Influence of Swelling on the Stiffness and the Fracture Energy of Microgel-Reinforced Hydrogels	61
4.1 Abstract.....	62
4.2 Introduction	62
4.3 Experimental Section.....	64
4.3.1 Microgel Production	64
4.3.2 Swelling Ratio of Microgels	64
4.3.3 Fabrication of MRHs	64
4.3.4 Fabrication of Double Network Hydrogels	64
4.3.5 Simple Extension Tests (SET)	65
4.3.6 Analysis of SET curves.....	65
4.3.7 Tensile Testing	65
4.3.8 Bulk Swelling Measurements.....	66
4.4 Results and Discussion.....	66
4.4.1 Fabrication and Swelling of MRHs.....	66
4.4.2 The Influence of Swelling on the Mechanical Properties of MRHs	67
4.4.3 Swelling Ratio of MRHs.....	68
4.4.4 Microgel Connectivity in MRHs: The Bridging Effect.....	69
4.4.5 The Effective Microgel Volume Fraction in MRHs.....	70
4.4.6 The Influence of Microgels on the Crack Propagation in MRHs.....	72
4.5 Conclusion	75
Chapter 5: Everything in its Right Place: Controlling the Local Composition of Hydrogels Using Microfluidic Traps	77
5.1 Abstract.....	79
5.2 Introduction	79
5.3 Experimental Section.....	80
5.3.1 Fabrication of the Microfluidic Devices	80

5.3.2 Formation of Water-In-Oil Emulsion Drops.....	81
5.3.3 Measuring Critical Flow Rates of Traps	81
5.3.4 Fabrication of Structured Hydrogel Sheets	81
5.3.5 Surface Evolver Simulations	82
5.4 Results.....	82
5.4.1 Influence of Trap Width.....	83
5.4.2 Simulations of Drop Shapes at Equilibrium	84
5.4.3 Influence of Trap Depth	85
5.4.4 Calculations of Surface Area Change Upon Trapping	86
5.4.5 Description of Model for Drops Relaxing into Spherical Microfluidic Traps	88
5.4.6 Influence of the In-Plane Trap Geometry on the Critical Flow Rate.....	90
5.5 Discussion	92
5.5.1 Application to the Design of Hydrogels with Locally Varying Compositions	93
5.6 Conclusion	96
Chapter 6: Conclusion & Outlook.....	97
Bibliography	99

Chapter 1

Introduction

1.1 The Intrinsic Limitations of Conventional Hydrogels

Hydrogels are polymeric networks swollen with water or aqueous solutions. [1] In a conventional hydrogel network, permanent covalent crosslinks greatly outnumber entanglements and physical or reversible bonds. [2] These networks can uptake lots of water, which makes them useful for moisturizing purposes as desired in diapers or for contact lenses. However, as all crosslinked polymeric networks, they intrinsically suffer from tradeoffs in terms of mechanical properties: Consider a volume of a gel V that contains a number of elastically active polymer chains n . A polymer chain is defined as the chain between two crosslinks, and consists of N monomers of length b , as illustrated in Figure 1.1a. [2] Thereby, the volume conservation for dry gels, in which the polymer occupies most of the space, gives

$$nNv = 1, \quad (1.1)$$

with v being the volume of a monomer. [2] The shear modulus of the gel can be written, by using equation 1.1, as

$$G = nk_B T = N^{-1}v^{-1}k_B T, \quad (1.2)$$

where k_B and T are the Boltzmann constant and the absolute temperature, respectively. [2], [3] For incompressible materials, such as hydrogels, the shear modulus G relates to the tensile modulus E , also called Young's modulus, as

$$E = 3G. \quad [4] \quad (1.3)$$

These last two relations stem from the affine model proposed by Kuhn in 1946, [5] which assumes that the macroscopic and molecular deformation modes are the same and that polymer chains undergo affine deformation. [4] It further assumes that the energy to deform polymer chains is much smaller compared to the energy needed to change the volume of the solvent the polymer chains are surrounded with, or to squeeze it out of the network. [4] This is the reason that hydrogels are considered as incompressible. In the phantom model proposed by James and Guth in 1949 [6] a correction factor that accounts for several polymer chains connecting to the same two crosslinks is introduced. [4] Equation 1.2 can be re-written as

$$G = \zeta k_B T, \quad (1.4)$$

where ζ is defined as the amount of independent elastic cycles per volume. [4] However, for simplicity I will use the term n in the following, and not ζ . The strain at break is written as

$$\varepsilon_b = \frac{Nb}{\sqrt{Nb}} = \sqrt{N}, \quad (1.5)$$

which is the ratio between the lengths of a polymer chain in its fully stretched and its relaxed state. [2] A polymer chain in its relaxed, and its fully stretched state is shown in Figure 1.1a.

The intrinsic fracture energy Γ_0 , that is, according to the Lake-Thomas model, the energy required to break all the polymer chains that transverse an area, is defined as

$$\Gamma_0 = n\sqrt{Nb}NU_f = nbU_fN^{3/2}, \quad (1.6)$$

where U_f is the energy required to break one monomer, NU_f the energy required to break one polymer chain, and $n\sqrt{Nb}$ the number of chains that transverse the area in their initially relaxed state. [2], [7] Note that NU_f includes the relaxation of all monomers a ruptured polymer chain consists of, thereby dissipating energy. [7], [8] As at the moment of chain scission all monomers the chain consists of are fully stretched, not only U_f is needed to break the chain, but NU_f . This correction was introduced because the theoretical fracture energy that only took the bond scission into account was much lower than experimental values of the intrinsic fracture energy. [7]

The variables n and N are related via equation 1.1, such that equation 1.6 can be rewritten as

$$\Gamma_0 = \sqrt{Nb}U_f v^{-1} = \sqrt{Nb}U_f \rho M_w^{-1}, \quad (1.7)$$

with ρ the polymer density and M_w its molecular weight. [9] By comparing equations 1.2, 1.5 and 1.7 we find that Γ_0 , ε_b and G are related to the chain length N , and relate among each other as

$$\varepsilon_b \sim \Gamma_0 \sim G^{-0.5}, \quad (1.8)$$

which nicely points out the intrinsic property trade-off between the strain at break, the intrinsic fracture energy and the shear modulus conventional hydrogels suffer from. [2] An increase in modulus can hence be achieved by increasing the density of crosslinks and thereby reducing the length of polymer chains N , which results, however, in a decrease of the strain at break and the intrinsic fracture energy of the gel. This applies also to gels that are swollen to equilibrium. We define the polymer chain swelling ratio ε_s , which is the ratio between the end-to-end distances of a polymer chain in its swollen relaxed and dry relaxed state. [2] For swollen gels, the strain at break ε_b and the shear modulus G are reduced by ε_s . The fracture energy Γ_0 is reduced by a factor ε_s^2 as the amount of polymer chains per area is reduced by this factor. [2]

Additionally, conventional hydrogels are often fabricated using random radical polymerization, which leads to an imperfect network that includes defects, [10]–[12] such as dangling bonds or loops, [13], [14] as illustrated in Figure 1.1b. These defects limit the strength a gel can achieve, as not all the polymer chains are contributing to bearing the load. The strength of a gel is herein defined and measured as the stress at break σ_b . Further, the functionality

of different crosslinks, f , which is the number of chains connected to a crosslink, is strongly varying, as illustrated in Figure 1.1b.

Another limitation of conventional hydrogels, that arises from random radical polymerization, is the large distribution of the chain lengths N . When a gel gets stretched, the individual chains will align until they have reached their fully stretched length Nb . If the chains are further stretched, they will break. As different chains reach their strain at break ε_b at different macroscopic stretches, they will rupture one after the other, starting with the shortest chains. This non-cooperative breakage due to stress concentrations on the shortest polymer chains limits the maximum stress a gel volume can withstand prior to catastrophic failure. [2], [15] It is as if short and long chains were coupled in series, and the network domain is as strong as its weakest part, as illustrated in Figure 1.1c. I will, in the next subchapter, review an attempt to resolve this limitation and to get closer to an ideal gel network.

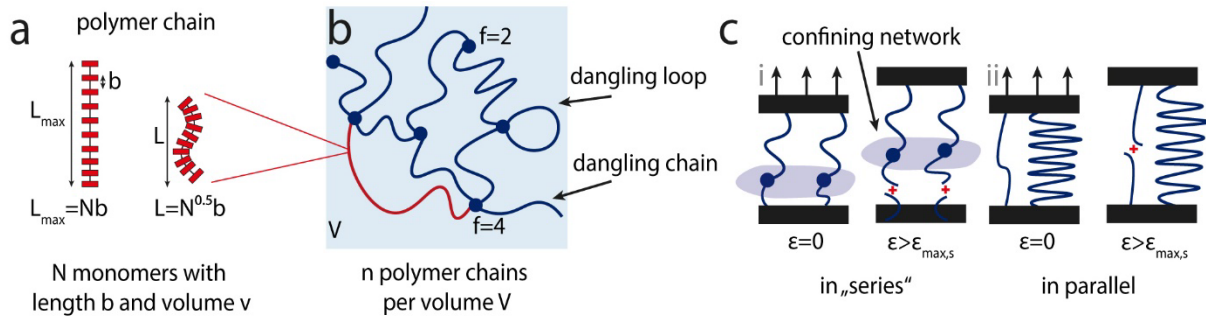


Figure 1.1: Conventional hydrogel network architecture. (a) A polymer chain consisting of N monomers with length b and volume v in its fully stretched (left) and relaxed (right) state with indicated end-to-end distances L_{max} and L , respectively. (b) An illustration of a conventional hydrogel network showing large variations in chain length, as well as dangling loops, dangling chains, and different crosslink functionalities. (ci-cii) A model of a conventional hydrogel featuring long and short chains at zero strain (left) and when stretched to a strain that exceeds the strain at break of the short chains (right). (ci) A hydrogel in which short and long chains are connected in series is as strong as its weakest part. The confining network that prevents the long chains from stretching to remove the stress from the short chains is visualized by the dark blue area. (cii) A hydrogel in which short and long chains are connected in parallel does not undergo catastrophic failure when the short chains rupture.

1.2 Designed Hydrogel Networks

1.2.1 Ideal Networks & Sliding Crosslink Networks for Strong Hydrogels

To reach a high stress at break a network should be engineered in a way that a large number of chains contributes to bearing the applied load simultaneously. [2] A wide chain length distribution is hence unfavorable to synthesize strong hydrogels. Fortunately, this limitation that arises from random radical polymerization was to a big extent overcome, and ideal networks were achieved by using macromolecules with a well-defined chain length N and functionalized end groups as the building blocks of the networks. A prominent example was presented in 2008, in which researchers use two symmetrical tetrahedron-like macromolecules to achieve a homogeneous network. [15] They could nicely show that the highest stress at break of the gel is reached at a stoichiometric ratio of 1 between the two molecules and that even slight deviations from this molar equality strongly decrease the strength of the

gel. [15] This result proves that an ideal network with a low density of defects and a narrow chain length distribution can indeed strongly enhance the stress at break of gels. The most common macromolecule used for the formation of ideal networks is tetra-PEG, [2] which has been functionalized with different end groups. [16]–[18] Please note that gel network models such as the affine and the phantom network models are based on ideal hydrogel networks.

Another method to avoid stress concentrations on short network chains is to introduce mobile crosslinks that can slide along the polymer chains to equilibrate polymer chain lengths during deformation. [2] Ideally, in a so-called sliding crosslink hydrogel, all the chains break simultaneously after the sliding crosslinks moved to form polymer chains of all the same length N_{final} . This leads to a high stress at break. Gels that exhibit sliding crosslinks are often synthesized from cyclodextrin-based polyrotaxanes, [2] and a pioneering example that features the “pulley-effect” due to figure-of-eight crosslinks was reported in 2001. [19] However, while ideal networks and sliding crosslinks can greatly increase the stress at break of polymeric networks by reducing the stress concentrations on short chains the property tradeoff mentioned in the first chapter between stiffness or fracture energy and extensibility still applies to them.

Ideal networks and sliding crosslink networks are classified as unimodal polymer networks, as the chain length distribution is unimodal. [20] This is opposed to another family of networks called multimodal polymer networks that show a multimodal distribution of chain lengths. [20] We will see in the next chapter how the intrinsic tradeoff between stiffness and extensibility can be decoupled using multimodal networks.

1.2.2 Multimodal Polymer Networks

Multimodal polymer networks are defined as networks that feature different chain length distributions within the same network. [20] Swollen multimodal networks would typically break at the strain at break of the longest chains

$$\varepsilon_b = \sqrt{N_{max}\varepsilon_s^{-1}}, \quad (1.9)$$

with N_{max} being the number of monomers of the longest chains in the system and ε_s the polymer chain swelling ratio. [2] The shear modulus G and the intrinsic fracture energy Γ_0 for swollen multimodal systems are given as

$$G = \sum n_i k_B T \varepsilon_s^{-1} \quad (1.10)$$

$$\Gamma_0 = \sum n_i b_i N_i^{3/2} U_i T \varepsilon_s^{-2}, \quad (1.11)$$

respectively. [2] Equations 1.9 and 1.10 show nicely that for a multimodal network, the strain at break and the modulus are decoupled: while short chains lead to a high modulus the long chains are responsible for the strain at break, a feature that has not been possible for conventional or unimodal polymer networks. While unimodal networks simply break at ε_b , multimodal network architectures can be designed so that the short chains break while the long ones still maintain the mechanical integrity of the network. Going one step back to conventional networks one could intuitively reason that in a conventional network, which has an extremely multimodal polymer chain

length distribution, the same would apply and small chains can fracture prior to longer ones without the network breaking. But this is obviously not what is observed. What is the difference between a multimodal network and a conventional network? To clarify this question, we will picture network components being either linked in parallel or in series: conventional networks can be seen as connected in series, with the weakest element breaking and thereby leading to catastrophic failure of the network domain, as illustrated in Figure 1.1ci. However, for multimodal networks, short and long chains are connected in parallel, which allows the long chains to take up the load after breakage of the short chains. Long and short chains acting in parallel are shown in Figure 1.1cii.

Multimodal polymer networks can be fabricated, among others techniques on which I will not focus here, using interpenetrating networks or networks with high-functionality crosslinks. [2] An interpenetrating network is defined as two or more individual, crosslinked networks that are not crosslinked among each other but physically entangled to the point that they cannot be separated without breaking them. [2] In polymer networks featuring high-functionality crosslinks, a large number of chains binds to the same crosslinker, whose functionality, f , is hence large. This results in several polymer chains with different lengths that connect two crosslinkers. [2] Typical examples of such multi-functional crosslinks are crystalline domains [21]–[23] or micro- or nanoparticles [24]–[27], to only name a few.

The concepts of unimodal and multimodal polymer networks was very nicely illustrated by Zhao et al., [2] here adapted as Figure 1.2. Unimodal networks, such as ideal networks or networks that feature sliding-ring crosslinks, fail once the chains have reached their ε_b , as illustrated in Figure 1.2a. This is in contrast to multimodal polymer networks, in which short chains break at their ε_b , while long chains, that are coupled in parallel to the short ones, take up the load, thereby preventing catastrophic failure of the network, as illustrated in Figure 1.2b.

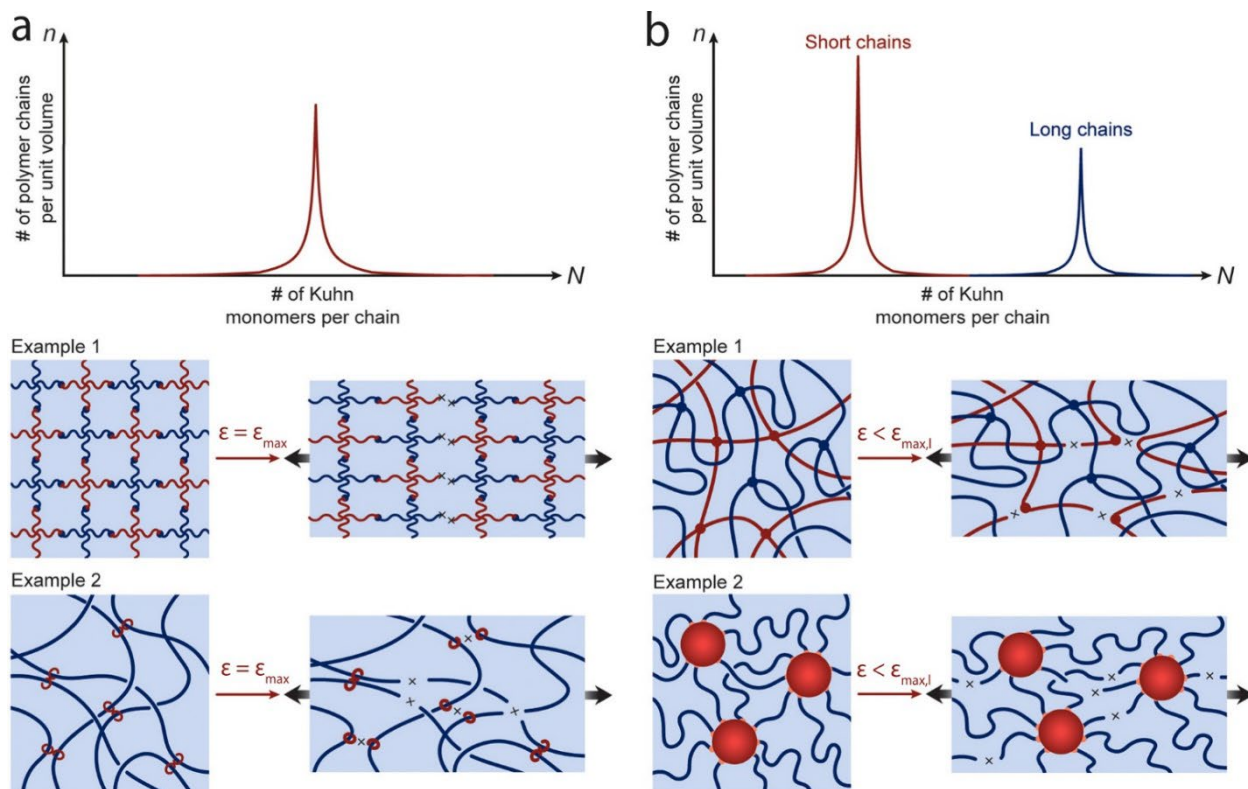


Figure 1.2: Unimodal vs. multimodal polymer networks. (a) In unimodal networks the polymer chain length N is uniformly distributed (top), which results in catastrophic material failure at the strain at break of the chains. (b) In multimodal networks the polymer chain length N is multimodally distributed (top), which results in breakage of short chains without catastrophic failure of the network segment. Adapted from [2] with permission. Copyright 2021 American Chemical Society.

The breakage of the short chains requires energy, which is dissipated during the network extension in the form of internal damage in the material. Such energy dissipation is of great interest for engineering materials that are more resistant to fracture, called tough materials. Multimodal polymer networks are hence excellent candidates to design tough hydrogels.

1.2.3 Elastic vs. Tough Materials

In the next chapter I will discuss the difference between elastic and tough materials, and its implications on the design of soft materials. To do so, I first need to define a few terms, elasticity, work of extension, fracture energy and resilience. In the chapter thereafter, I will discuss energy dissipation in a famous example of multimodal networks, double network hydrogels.

Elasticity

An elastic material is defined as a material that linearly deforms upon loading. Linear elasticity is best described using Hooke's law that says "as the extension so the force". [28] Upon elastic deformation the microstructure of the material is not altered and upon unloading the material goes back to its original shape without permanent, *plastic* deformation. [29] The initial slope of the linear loading-elongation curve, also called stress-strain curve, is

defined as the Young's modulus, which is the measure of stiffness of the material under tensile or compression loading in the unit Pa:

$$E = \frac{\sigma}{\varepsilon} = 3G. \quad (1.12)$$

In a perfect elastic deformation, there is hence no energy dissipated, but the material acts as a spring that stores elastic energy, which is released upon unloading. Many materials, also tough ones, feature an elastic regime below a certain strain threshold. An elastic deformation and how the Young's modulus can be deduced from these curves are illustrated in Figure 1.3a.

Work of Extension

The work of extension, herein called work to break W_b , is a metric of how much energy needs to be provided to a volume of material for it to undergo catastrophic failure. [30] It is defined, in the unit J m^{-3} , as

$$W_b = \int_0^{\varepsilon_b} \sigma d\varepsilon. \quad (1.13)$$

with ε_b being the strain at break and σ the stress applied to the material. In experiments, W_b can be measured as the area under the stress-strain curve. However, as the material is not undergoing any unloading, but is stretched up to fracture, the work to break does not distinguish whether energy was stored elastically or whether it has been dissipated in the material. For gels, W_b is defined as

$$W_b = nNU_f, \quad (1.14)$$

which is the number of chains per volume multiplied with the amount of energy required to break a polymer chain. [3], [8]

Fracture Energy

The fracture energy is defined as the energy required to advance a crack by a unit area, with the units J m^{-2} . It describes how resistant to fracture a material is.

Resilience vs. Toughness

Resilience is the ability of a material to regain its initial shape after unloading, without energy being dissipated during the loading-unloading cycle. Elastic materials are according to this definition truly resilient. The counterpart to resilience is toughness. Tough materials dissipate energy during a loading-unloading cycle, as illustrated in Figure 1.3b. The hysteresis, shown as the grey area between the loading and the unloading curve, depicts the dissipated energy U_{hys} . The red area below the unloading curve represents the elastic energy that is regained upon unloading, U_{el} . The ratio between the dissipated energy during a cycle and the total work done on the material during the cycle can be calculated using the hysteresis ratio H , which is given as

$$H = \frac{U_{hys}}{U_{hys} + U_{el}}. [2] \quad (1.15)$$

The resilience of a material for a given cycle is defined as

$$R = \frac{U_{el}}{U_{hys} + U_{el}}. [2] \quad (1.16)$$

Those two numbers are simply related as

$$R = 1 - H. \quad (1.17)$$

This illustrates that, if the dissipative mechanism is irreversible, which is the case for covalently crosslinked hydrogels, there always is a tradeoff between energy dissipation and the ability of a gel to undergo cyclic loadings with persistent performance.

Mullins effect

For tough materials, the amount of dissipated energy is strongly related to the strain a material element undergoes. During a first loading-unloading cycle to a defined strain the material dissipates energy, thereby undergoing internal damage or alterations in its structures. When the material is subsequently loaded to the same strain a second time, its loading curve will follow the unloading curve of the previous cycle, hence it is much softer. Upon stretching to larger strains than during the first cycle the stress-strain curve will at these higher strains follow the one from the virgin material. This effect is called the Mullins effect [31]–[33] and is illustrated in Figure 1.3c.

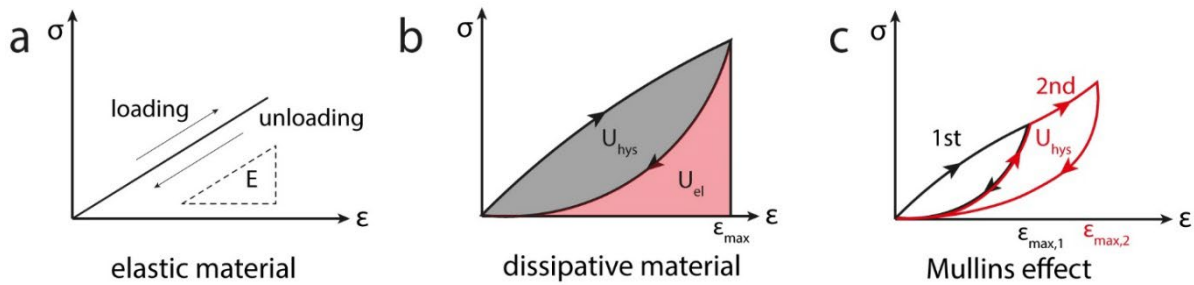


Figure 1.3: Elastic vs. dissipative materials. (a) A loading-unloading cycle of an elastic material. The slope of the curve indicates the Young's modulus E . (b) A loading-unloading cycle to strain ϵ_{max} of a tough material. The grey area depicts the dissipated energy U_{hys} . The red area depicts the elastic energy that is regained after unloading U_{el} . (c) An illustration of two subsequent cycles on the same material with $\epsilon_{max,1} < \epsilon_{max,2}$. The phenomenon that the loading curve of cycle $n+1$ follows the unloading curve of cycle n is called Mullins effect.

I will now review deformation and internal fracture of a type of multimodal networks, the double network hydrogels (DN's).

1.3 Energy Dissipation in Double Network Gels

Double networks are a famous example for an interpenetrating network that were introduced in 2003 by the group of Jian Ping Gong. [34] The classical double networks are fabricated in a two-step process: A stiff and highly crosslinked first network, often made of 2-Acrylamido-2-methylpropane sulfonic acid (AMPS) monomers, which is

a polyelectrolyte, is fabricated. This first network can be strongly swollen in the precursor solution of the second network, often made from acrylamide (AAm), despite its high crosslink density and hence short polymer chains N . The second network is composed of very long polymer chains and few crosslinks. [35]

In another prominent example, an extremely tough and extensible DN hydrogel was fabricated in a one-step process: acrylamide monomers and alginate were dissolved in water, together with a crosslinker and a photoinitiator to covalently crosslink the acrylamide, and calcium sulphate to ionically crosslink the alginate. [36] In this hydrogel system, the alginate acts as sacrificial first network, as it is highly crosslinked, while the second network is formed from polyacrylamide. It bears the advantage that it is fabricated using a one-step process and that the ionically crosslinked network can heal over time. [36] However, it has the disadvantage that it cannot be used under physiological conditions as salts weaken the coulombic interactions within the ionically crosslinked network. [9]

When a double network hydrogel is stretched, the short chains of the first network lead to a high initial modulus E , while the long polyacrylamide (PAAm) chains lead to a high strain at break ε_b . This is a typical decoupling of mechanical properties for multimodal polymer networks, as it has been introduced in chapter 1.2. Further, the short chains the first network is composed of break if the material element is stretched to higher strains than their ε_b . If the double network hydrogel, however, is properly designed the long chains take over the load and homogeneously distribute the stress throughout a large damage zone, thereby reducing stress concentrations. It was shown that this toughening mechanism works regardless if the two networks are covalently coupled to each other or not, if the amount of crosslinker of the second network is properly adapted. [37] However, during a classical DN synthesis, the two networks usually feature inter-network crosslinks. [37] A double network with both networks being truly independent can be achieved by passivating excess crosslinkers present in the first network before the second network is polymerized. [37] In all cases it has been shown that the two networks of DN's are highly entangled. [38] However, there are two schools with different visions on how the first network of DN's undergoes internal damage:

The DN structure is pictured by Gong as highly heterogeneous. The first network is composed of tiny islands of gels that are held together through some elastic strands. [39] It was shown that during cyclic loading with increasing maximum strain ε_{max} for every cycle, the initial stiffness of a DN rapidly decreases with increasing ε_{max} , as shown in Figure 1.4a. [39] This softening was assigned to the initially fractured PAMPS chains, which are supposedly the elastically active ones that connect the microgels in the direction of pull. The microstructure of the first network composed of gel island connected to each other through few strands is illustrated in the inset of Figure 1.4a. [39] The connecting strands are thought to be responsible for the continuity of the first network and hence the initial stiffness. [39] In another study it was found that if only 1% of the PAMPS chains break, 80% of the elasticity of the first network is lost, which further hints at the proposed morphology of the first network. [31] Hence, as soon as DN gels start to yield the first network becomes discontinuous, which significantly softens the materials, and the

microgels fracture into smaller and smaller clusters, thereby dissipating energy. [39] The cluster size was measured to be around 1.5 μm in size according to a SANS study. [40] The energy dissipation and the re-swelling after deformation are, in contrast to the initial stiffness, less dependent on the connecting strands in the direction of pull. That is why these parameters follow a linear trend as a function of ε_{max} throughout the necking process, as shown in Figure 1.4b and 1.4c. A sketch by Gong [35] that illustrates her vision is reprinted in Figure 1.4d.

According to the model of Brown [41] the first network of DN's does not fracture into clusters, but it suffers damage in the form of microcracks that only coalesce when catastrophic failure occurs. [41] It was indeed observed that upon cyclic loading of a multi-network elastomer, the initial stiffness does not decrease as much as in the case of the DN hydrogel, as shown in Figure 1.4e. [42] Using mechanochromic molecules Creton and coworkers showed that during necking only 9% of the first network chains that were loaded at the onset of necking would rupture, as shown in Figure 1.4f. [43] They interpreted that the first network still carries a significant amount of load during the necking process. An illustration by Creton [43] on how the first network breaks, in response to the sketch by Gong, is reprinted in Figure 1.4g.

It might very well be that this difference, which can be considered a detail, arises from the fact that hydrogels and elastomers do have different load transfer mechanisms between the networks, or that the measured elastomer networks were not truly independent, while truly-independent DN's were studied. [43] However, it is of interest to understand how the first network breaks, to then also link its structure to the way these materials undergo catastrophic failure.

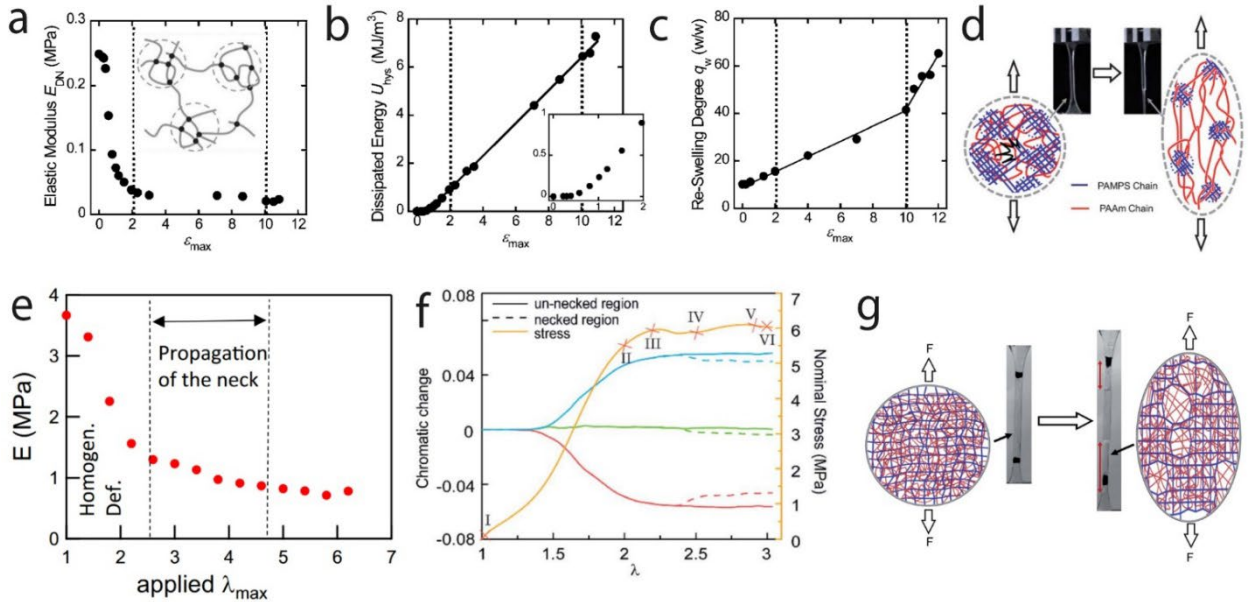


Figure 1.4: Rupture of the first network in multi-network gels. (a-d) Vision and data of Gong and co-workers and (e-g) of Creton and co-workers. (a) Young's modulus of a double network hydrogel composed of two truly independent networks during cyclic loading as a function of the cycle's maximum strain ε_{max} . Inset: Illustration of the heterogeneous structure of the first network featuring gel islands that are sparsely connected. (b) Dissipated energy per loading-unloading cycle as a function of the cycle's maximum strain ε_{max} . (c) Re-swelling of the sample as a function of the cycle's maximum strain ε_{max} . (a-c) The dotted lines mark the transitions between the regions pre-necking, necking, and hardening. (d) Illustration by Gong on how the first network breaks into clusters. (e) Young's modulus E (MPa) as a function of applied λ_{max} . The plot shows a sharp drop in modulus during necking, labeled 'Propagation of the neck'. (f) Chromatic change and Nominal Stress (MPa) as a function of λ . The plot shows the evolution of the first network (red) and second network (blue) during necking, with regions I-VI marked. (g) Illustration by Creton on how the first network breaks, showing the first network (red) and second network (blue) chains.

clusters before necking. (e) Young's modulus of a multi-network elastomer during cyclic loading as a function of the cycle's maximum strain ε_{max} . (f) Chromatic change of mechanochromic molecules contained in the first network as a function of the applied strain. There is only little change between the necked (discontinuous line) and the un-necked (continuous line) region above 250% strain (g) Illustration by Creton on how the first network still holds a significant amount of load during necking. (a-c) adapted from [39] with permission. (d) Adapted with permission from [35]. (e) Adapted with permission from [42]. (f-g) Adapted from [43] according to the Creative Common License.

1.4 Fracture Mechanics of Soft and Tough Solids

1.4.1 Nonlinear Strain Fields During Fracture of Tough Materials

Tough materials dissipate a significant amount of energy when strained. The amount of dissipated energy strongly depends on the maximum strain a material element is subjected to. [31]–[33] This is not only the case for materials that are homogeneously strained to well-controlled strain values, but gains even more importance during the fracture of tough materials. Ahead of the crack tip, the material undergoes complex and nonlinear strain fields and the maximum strain a material element undergoes is non-trivial to predict. [44]–[46] I will now investigate the influence of the presence of high local strains and energy dissipation in DN's on how these tough materials undergo catastrophic failure.

1.4.2 Nonlinear Elastic and Dissipative Length Scales

In contrast to linear elastic fracture mechanics (LEFM), in which materials are considered to behave mainly linearly elastic with a tiny fracture zone around the crack tip, the fracture of soft materials includes strong nonlinear elasticity. [8] Nonlinear deformation around a crack tip has been nicely visualized using digital image correlation (DIC) for soft elastomers [47] and double network hydrogels. [45] The intrinsic material length scale that defines the size of the zone around the crack tip in which nonlinear elasticity arises is called the elasto-adhesive length scale [3] or the nonlinear elastic length scale, [8] and is defined as

$$l \sim \frac{\Gamma}{E}. \quad (1.18)$$

Here, Γ is the fracture energy and E the Young's modulus. l can be understood as the distance from the crack tip where surface energy and bulk elastic energy become similar, or in other words, below which surface effects can cause large material deformation. [3]

Interestingly, it was found that in soft materials l can be related to the crack tip opening displacement (CTOD) δ , as

$$\delta \sim \frac{\Gamma}{E} \sim l. \quad [8], [47] \quad (1.19)$$

However, for tough gels the CTOD needs to be corrected with an exponential factor as $\delta \sim \left(\frac{\Gamma}{E}\right)^\alpha$, with $\alpha \sim 0.8$ -1.1 being close to unity, making the use of l still reasonable. The elasto-adhesive length scale is hence not only useful to predict the nonlinear zone around a crack tip, but can also be measured on the macroscopic scale as the crack tip opening displacement. However, for stretchy and dissipative gels, such as DN's, it has been shown that under

dynamic conditions the CTOD deviates from the parabolic shape predicted by LEFM. [48] From the observed CTOD a rate-dependent length scale

$$l(v) \sim \frac{U_{el}}{G} \quad (1.20)$$

has been derived that shows that the observed CTOD and hence $l(v)$ are linearly dependent on the elastic energy stored in the material U_{el} . [48] Here, G is the shear modulus.

The fact that soft and tough materials not only deform nonlinearly, but also dissipate energy adds another level of complexity to the problem of their fracture. I define a second intrinsic material length scale, which describes the failure zone around the crack tip in which stress and strain fields vanish because they are dissipated within the material. [8] It can be written as

$$\zeta \sim \frac{\Gamma}{W_b}. \quad (1.21)$$

The two numbers l and ζ were nicely presented by Long et al. [8], here adapted as Figure 1.5a. ζ has been established as the fractocohesive length. [49] As all the stress fields within a zone of length ζ around the crack tip are dissipated it makes the material insensitive to cracks that are smaller than the fractocohesive length. This is illustrated in Figure 1.5b. It has been observed that ζ , calculated from equation 1.21, is of the same order of magnitude as the surface rugosity of newly formed cracks in natural rubbers. [50].

An overview of different materials and their nonlinear elastic and fractocohesive length scale is shown in Figure 1.5c. It is interesting to note that steel, which is highly ductile, can e.g. be found above the $l = \zeta$ diagonal, while Tetra-PEG gels, which we have encountered in chapter 1.2.1, and which are highly elastic but not dissipative, are found below the diagonal. For brittle conventional gels like PAAm we find $c \gg l \gg \zeta$. [8] Thereby, the fractocohesive length depends on the crosslinking density and can vary between 1 mm for loosely crosslinked, [12] and 20 μm for highly crosslinked PAAm [51]. For double network hydrogels we find $l \gg \zeta \sim c$, with c being a crack length. [8]

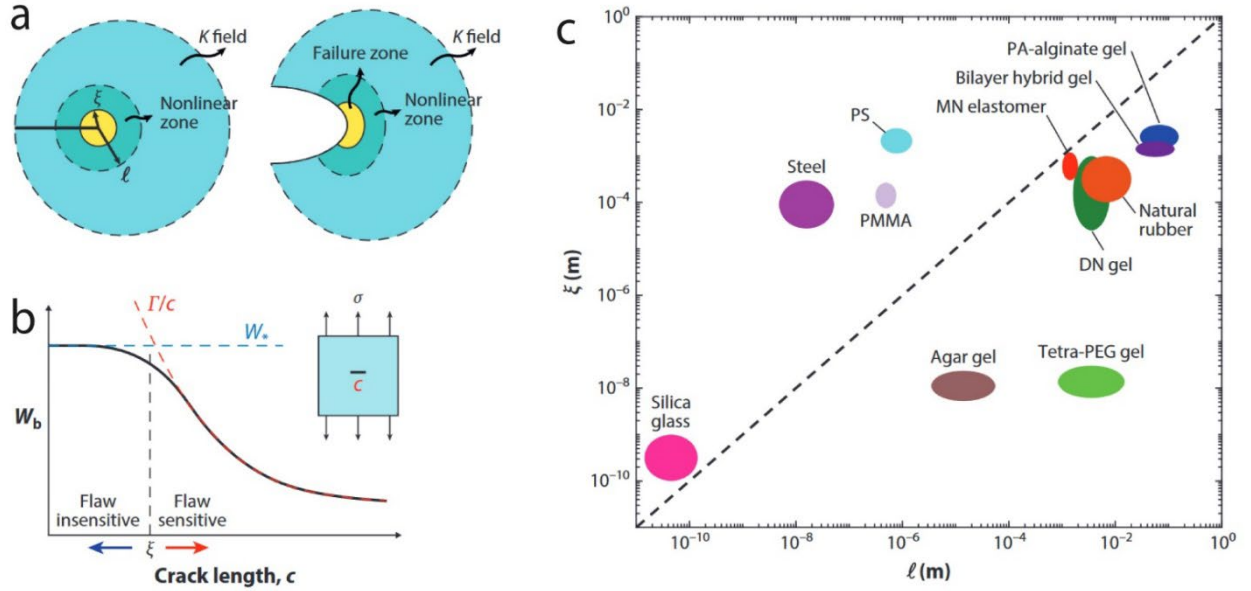


Figure 1.5: Two intrinsic material length scales. (a) The nonlinear elastic length scale l and the fractocohesive length ζ are defined in the undeformed and the deformed states around a crack tip. (b) The work to break W_b as a function of the crack length c . The fractocohesive length ζ indicates the crack length below which the material is insensitive to them. (c) An Ashby plot that relates l and ζ for different materials. (a-c) are adapted from [8] with permission.

1.4.3 Intrinsic and Dissipative Fracture energy

In chapter 1.1 I have presented the intrinsic fracture energy Γ_0 . It quantifies the energy required to break polymer chains to create new surfaces. However, when tough materials break, there is a substantial amount of energy dissipated in the bulk material. Remember e.g. the breakage of short chains in multimodal polymer networks while the long ones in parallel to them maintain the mechanical integrity of the material. The fracture energy can hence be divided into two components:

$$\Gamma = \Gamma_0 + \Gamma_D, \quad (1.22)$$

with Γ_D being the dissipative part of the fracture energy. [8], [44], [52] For tough gels usually $\Gamma_0 \ll \Gamma_D$. [52] However, in tough hydrogels the intrinsic fracture energy still cannot be neglected, and the fracture energy Γ was shown, using experiments and simulations, to be linearly related to it as

$$\Gamma = \frac{\Gamma_0}{1 - \alpha h_{max}}. \quad [52] \quad (1.23)$$

Here, $0 \leq \alpha \leq 1$ is a dimensionless number related to the size of the hysteresis area during cyclic loading and $0 \leq h_{max} \leq 1$ is the ratio between the dissipated energy and the applied external stress. [52] They are hence directly linked to Γ_D . To design tough materials, the ratio between the dissipated energy and the applied mechanical load should hence be high, and dissipation should be activated at low strains. [52] The linear relation between Γ and Γ_0 can be intuitively understood as if the second network is brittle cracks easily propagate while the load cannot be transferred to the surrounding first network.

1.5 Fracture of Double Network Hydrogels

1.5.1 Damage Zone in Double Network Hydrogels

In tough materials, the loading history and the amount of strain encountered by a material element strongly influences how much energy it dissipates. [31], [44] Indeed, during fracture of double networks the encountered strain of a material element is highly dependent on its distance to the crack measured perpendicular to it. [44] This relationship was shown using digital image correlation, [45] here shown in Figure 1.6a. The question arises whether there is a way to predict how much energy will be dissipated during crack propagation in a double network hydrogel?

In attempts to predict the fracture energy of DN's, which was measured in 2005 for the first time, [53] Tanaka [54] and Brown [41] independently came up with physical models. They both assume that there exists a local damage zone around the crack tip with width h . All the material elements inside the damage zone are exposed to the maximum strain arising in the system, which makes them dissipate energy, while outside of the damage zone, the material elements remain in their elastic regime and no dissipation occurs. [41], [44], [54] This hypothesis is supported by experiments performed in the group of Gong, in which they could visualize a distinct damage zone, as shown in Figure 1.6b. The elastic behavior and the dissipation mechanism outside and inside the damage zone, respectively, as proposed by Tanaka and Brown, are illustrated in Figure 1.6c. The fracture energy was estimated as

$$\Gamma = k\sigma_c\varepsilon_ch. [55] \quad (1.24)$$

Here, k is a geometrical factor around unity, while σ_c and ε_c are the yielding stress and the strain at which strain hardening occurs, as schematically shown on a simplified stress-strain curve in Figure 1.6d. Although the fracture energy was overestimated by a factor six, Gong could nicely show that $\Gamma \propto h$, as shown in Figure 1.6e. Interestingly, by omitting k , which is reasonable because it is close to unity, [55], and by assuming $\sigma_c\varepsilon_c \sim W_b$ we find the fractocohesive length ζ as

$$h \sim \frac{\Gamma}{\sigma_c\varepsilon_c} \sim \frac{\Gamma}{W_b} \sim \zeta. \quad (1.25)$$

By inserting $W_b \sim 10 \text{ MJ m}^{-3}$ and $\Gamma \sim 1000 \text{ J m}^{-2}$, which are reported experimental values, [35] a fractocohesive length of $\zeta \approx 100 \text{ }\mu\text{m}$ is estimated, which is in the same order of magnitude as the experimentally observed h . [8] However, when DN's undergo dynamic fracture, ζ can be significantly larger than $100 \text{ }\mu\text{m}$. [48], [55]

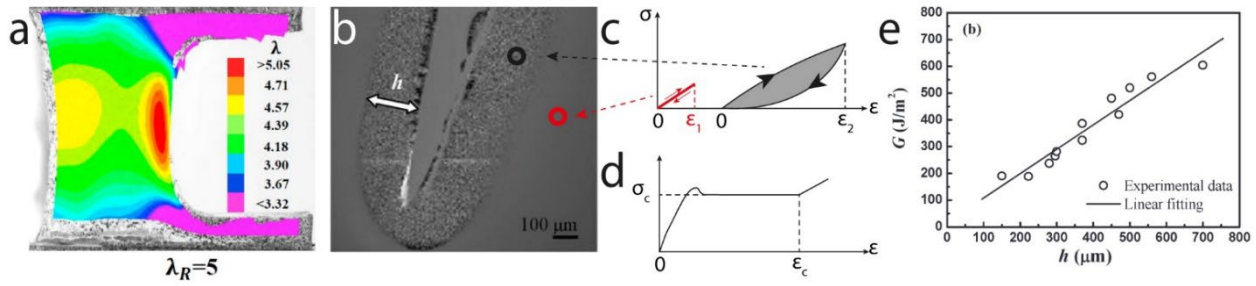


Figure 1.6. Energy dissipation in double network hydrogels (DN's) upon crack propagation. (a) Micrograph of a DN hydrogel showing the strain field ahead of the crack tip, visualized using digital image correlation. The sample was pre-stretched to 400% before imaging. Sample width = 6 mm. (b) Micrograph taken with a color 3D violet laser scanning microscope, showing a clearly distinct damage zone around a crack in a DN hydrogel. (c) Schematic illustration of the stress-strain cycles a material element inside (black) and outside (red) of the damage zone underwent. (d) An idealized stress-strain curve of a DN hydrogel with indicated yield stress σ_c and the strain at which hardening occurs ϵ_c . (e) The measured fracture energy as a function of the damage zone width, which is indicated in (b). (a) adapted from [45] with permission. Copyright 2014 Elsevier. (b,e) Adapted from [55] with permission. Copyright 2009, American Chemical Society.

We have just seen that in double network hydrogels a propagating crack is often surrounded by a large damage zone. [55] The phenomenon of a large damage zone in which strong dissipation occurs applies to several families of materials, such as polymeric materials, [56] ceramics, [57] metals, [58] or fiber-reinforced composites. [59] Also many natural materials feature energy-dissipative mechanisms to resist fracture. [60] In the field of hydrogels, toughening strategies on different length scales were carefully reviewed. [61]

The field of deformation and fracture of soft and tough materials is rapidly evolving. Interestingly, the field includes studies that address the different length scales ranging from the molecular level, [7], [62], observations of dissipation mechanisms on the mesoscale [55], [63], to studies of the macroscopic crack opening, crack tortuosity and deformation. [45], [47], [48], [64] A particularly interesting length scale, on which I will focus in the following, is the μm to 100's μm length scale. It has been shown that in DN's the first network breaks into clusters with a size around 1 μm [40], while the damage zone in DN's was visualized to be in the order of 100 μm , [55] staking out a length scale that is indeed worth closer examination. In a recent study on 3D printed elastomers featuring engineered porosity, it has been shown that differences in the pore structure only had an effect on the crack propagation if pores were not larger than 1 mm. [64]

1.6 Microstructured Hydrogels

1.6.1 Bio-Inspired Microstructuring of Hydrogels

We will now, in response to the findings described above, for a moment leave the field of mechanics of hydrogels to deepen our knowledge on the fabrication of hydrogels that are structured on the tens to hundreds of μm length scale and the advantages that can be achieved thereby. Materials that are structured on these length scales can also be found in nature. An example comes from the field of adhesion science: several animals fabricate adhesive pads with features on the microscale to improve their adhesion underwater or to wet surfaces. [65]–[67] Such structures were copied by researchers to harvest the favorable adhesive properties that arise from the

microstructuring observed in natural materials. This approach is called bio-inspired design or bio-mimicry, [68], [69] and spans a wide range of natural materials, such as spider silk, [70], [71] nacre, [72] or fibrous plant tissues. [73] Bio-inspired design is a fascinating topic, as nature produces a huge variety of materials from a limited set of elements and often under benign conditions to enable life of the creatures fabricating them. As in evolution, the fittest survive and as an efficient adaption to the current environment is crucial, nature conducted millions of years of research and development to provide us with time-tested recipes to fabricate materials.

In the next chapter I will hence review microstructures that are found in nature and how they were successfully reproduced by researchers using current techniques that are available to them, including molding, [65]–[67] photolithography, [74], [75] shaping of materials using surface and interfacial forces, [76]–[78] and 3D printing. [79] The most important discoveries in the engineering of hydrogels on different length scales has also been broadly reviewed. [80]

1.6.2 Molding for Bio-Inspired Wet Adhesion

An example in which a certain functionality of natural materials was successfully mimicked by microstructuring hydrogels is taken from the field of adhesion science. It has been observed that animals capable of undergoing strong underwater adhesion rely on hexagonal patterns on their foot. Prominent examples are the clingfish [67], the tree frog [65] and the octopus [66]. A photograph of a clingfish adhesion disc and a scheme of its hexagonal pattern are shown in Figure 1.7a and 1.7b, respectively. Researchers used micromolds as substrates to synthesize hydrogels featuring a hexagonal patterning with side lengths of 10 μm [65] or 0.875–1.75 mm [67], and to pattern cylinders with a diameter of 100 μm [66]. It was shown that the size of the hexagonal microstructure strongly influences the adhesion performance, as too large hexagonal pads would trap water underneath their center, while an optimal, smaller size ensures increased actual contact area, leading to improved adhesion. [67] Molded large and small hexagonal facets are shown in Figure 1.7c. Another inspiration for adhesion using patterned features is the octopus and its arms, here shown in Figure 1.7d. A study reproducing its cylindrical adhesion pads showed that too small pads do not lead to sufficient suction underwater, resulting in an optimal feature diameter of around 100 μm . [66] Additionally, the curvature of the groove on the pads was shown to strongly influence the adhesion properties with the highest curvature showing the strongest suction and hence adhesion. [66] Micro-engineered octopus-inspired cylindrical adhesion pads with a high inner curvature are shown in Figure 1.7e.

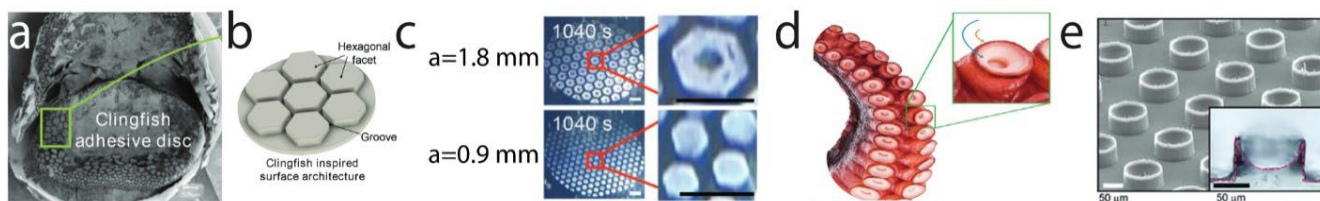


Figure 1.7: Bio-Inspired microstructures for underwater adhesion fabricated via molding. (a) Clingfish showing adhesive pads with hexagonal patterns that served as inspiration. (b) Scheme of a hexagonal clingfish-inspired adhesive surface. (c) Micrographs of engineered hexagonal patterns with a side length of 1.8 mm (top) and 0.9 mm (bottom). The larger pads entrap water in their center, which reduces the effective adhesion surface. Scale bars = 4 mm (d) Sketch of an octopus arm covered with cylindrical pads with a cavity in their center for effective suction. (e) Micrographs of engineered cylindrical pads made using molding. Inset: The red line shows the inner curvature of the cavity, which proves to be an important factor for the adhesion strength of the pads. (a-c) are modified from [67] with permission. (d-e) are modified from [66] according to the Creative Common License.

A well-defined microstructure found in the human body featuring strong anisotropy is the myocardium, the muscular tissue of the heart. Researchers used an elastomeric poly(dimethylsiloxane) (PDMS) mold to produce microgrooves with a depth, width, and spacing of 50 μm into a conductive hydrogel to achieve topological similarity with the myocardium structure. [81] Cells organized and aligned on top of the micropatterned platform to result in tissues acting very similarly to the natural myocardium. [81], [82]

Molding is a facile and ready-to-use method to introduce surface patterns on the microscale into bulk hydrogels. Molds can be fabricated with resolutions down to 10's of micrometers, e.g. using photoresists like SU8. [83] These photoresists are very often cured, as the name indicates, using UV light and a photomask. However, while the use of molds allows to pattern the surface of hydrogels, their bulk compositions cannot be controlled. Further, molding is often limited to one type of hydrogel, with one set of mechanical properties. If different degrees of crosslinking are desired within the same hydrogel sheet, or gradients of properties are required, molding faces its limitations. One method that enables the control of the bulk composition of hydrogels, and allows to introduce compositional gradients into them, is photolithography, which I will present in the next subchapter.

1.6.3 Photolithography for Plant-Inspired Patterned Self-Shaping Materials

Patterning in Two- and Three-Dimensions Using Light

Photolithography techniques to crosslink hydrogels with spatial complexity and concentration gradients were first used in the late 2000's. Instead of using a photomask to pattern a mold on which the hydrogel is subsequently cured, light is employed to selectively crosslink hydrogel precursor solutions. With UV light and a photomask patterns with a resolution down to 100's of micrometers were introduced into already prepared bulk hydrogels that were previously soaked with a photosensitive precursor, as shown in Figure 1.8a. [84] Photolithography is hence not limited to the surface of the hydrogel, but the light travels through the entire sample thickness, thereby crosslinking the precursors. Using this technique, stripes with varying stiffnesses were introduced into soft bulk hydrogels, as well as continuous stiffness gradients. [85] A stripy hydrogel sample with locally varying stiffness is shown in Figure 1.8b. A more recent example uses orthogonal photolithography with distinct precursor molecules

to either trigger the polymerization of one or two kinds of monomers. [64] This complex chemistry is used to produce a mussel byssus inspired 2D structure with a soft, porous core and a stiff surrounding. [64]

However, when using flood UV light and a photomask, the spatial control of the process is limited to two dimensions. To gain control over three dimensions, a laser can be employed in a two-photon lithography process, with which the z-dimension of the resulting pattern can be controlled. [86] This approach was applied to guide cell growth in three dimensions, [86] or to pattern proteins within preformed hydrogels [87], which is shown in Figure 1.8c. However, while these approaches allow for very high resolution in three dimensions, they rely on advanced chemistries and the patterning of centimeter-scale surfaces is time-consuming.

Patterned Stimuli-Responsive Hydrogels for Self-Folding Sheets

Another source of inspiration that comes from the natural world are stimuli-responsive self-morphing plants and their products. For example, conifer pinecones close their scales when exposed to wet environments to protect the seeds contained in them, and reopen when the environment dried. [88] A pinecone in its closed and its open form is shown in Figure 1.8d. Hydrogels are excellent candidates to fabricate self-morphing structures from them due to their stimuli-responsiveness. Their swelling, which means water uptake, is highly dependent on material factors such as the number of monomers per chain, N , or the hydrophilicity of the employed monomer. Further, depending on the employed monomer, hydrogels show strong responses to external stimuli such as ionic strength, temperature, or pH. The degree of swelling under different conditions and external stimuli can be abruptly engineered over short length scales, e.g. by introducing a patterned functional network into a primary gel sheet using photolithography. When thin hydrogel sheets with locally varying stimuli-responsiveness are subjected to external stimuli, stresses will develop due to local swelling gradients. These stresses will cause the sheet to deform to equilibrate them, as illustrated in Figure 1.8e. The class of materials that leverages local internal stresses, induced by engineering the local composition of a 2D material, to attain a desired shape in two or three dimensions upon exposure to a certain stimulus are called self-morphing materials. For example, two-dimensional hydrogel sheets with engineered locally varying stimuli-responsiveness morphed into three-dimensional structures upon external stimuli, including ionic strength, pH or temperature, as shown in Figure 1.8f and 1.8g. [74], [75] This concept was further explored to produce highly complex surfaces that deform in three dimensions from temperature-responsive photopatterned hydrogel sheets. [89]

Photolithographic techniques have hence been used to guide cell growth, to assemble proteins in a bulk hydrogel in three dimensions, or to pattern two-dimensional sheets for shape-morphing materials. A recent improvement of photolithographic techniques is the introduction of digital micro-mirror devices (DMD's). These devices that employ tiny mirrors that either reflect or transmit light have the potential to be of use for rapid prototyping and to replace expensive and, very often, single-use photomasks. [90]–[92]

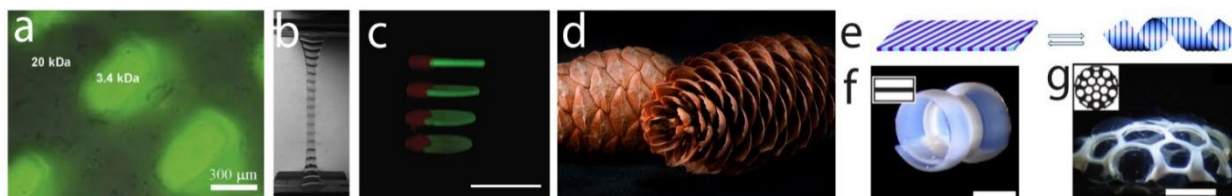


Figure 1.8: Photolithography techniques and plant-inspired self-morphing. (a) A hydrogel sheet composed of poly(ethylene glycol) diacrylate (PEGDA) with gradients in stiffness that were fabricated using photolithography. (b) Photograph of a PEGDA-based sample into which stripes with different stiffnesses were introduced. (c) 3D patterning of different proteins into a prefabricated hydrogel using two-photon chemistry and a laser. (d) Pine cones open or close their scales depending on the humidity of their environment. (e) Scheme of a patterned 2D hydrogel sheet that was produced using photolithography. Upon stimuli (arrows) the 2D sheet reversibly transforms into a 3D structure to equilibrate internal stresses that arise from local differences in the degree of swelling. (f-g) Complex 3D structures that self-morphed from a patterned 2D sheet upon stimulus. The patterns that were introduced into the 2D sheets are shown as insets. (a-b) Adapted with permission from [85]. (c) Adapted with permission from [87]. (e) Adapted with permission from [74]. Copyright 2013 American Chemical Society. (f-g) Adapted with permission from [75].

1.6.4 Patterning using Physical Properties of Liquids

While the structuring techniques mentioned above make use of hydrogel precursor solutions that are polymerized either on a patterned surface or in a spatially controlled way using light, they are not making use of any fluid properties the precursor solutions could provide to shape the final material. By contrast, the surface tension of the precursor solution was used in an open microfluidic system for layer-by-layer production of complex hydrogel shapes. [78] The meniscus of the precursor solution is pinned between the previously formed gel layers and a suspended mold, with which the shape of the meniscus is defined, prior to the polymerization of the monomers, as illustrated in Figure 1.9a. [78] Built structures using this open-microfluidics method are shown in Figure 1.9b. However, while the thickness of the layers can be as low as 100 - 500 μm and overhanging structures can be printed due to the water-air interfacial tension, the in-plane resolution is only on the millimeter scale. [78]

Another method that uses the physics of fluids to pattern materials is to employ a laminar flow, which leads to well-defined liquid-liquid interfaces if two liquid phases meet. Laminar flow is observed at low Reynolds numbers, a nondimensional number defined as $Re = uD/\nu$, with u being the flow rate of the fluid, D the characteristic length scale of the system, and ν the kinematic viscosity of the fluid. In a recent example, a Hele-Shaw cell, which is defined as a microfluidic cell with a thickness being much smaller than its width and length, [93] is used to pattern 2D elastomer sheets. Different viscous elastomer precursor solutions are poured into the Hele-Shaw cell from prefabricated holes in the ceiling, from where they start to slowly flow until the menisci of the two different solutions meet. [76] Due to very low Reynolds numbers, the phases form a stable interface when they meet to form a continuous elastic sheet after curing, as shown in Figure 1.9c. [76]

The deformation of liquids can also be used to pattern hydrogels by forming monodisperse water-in-oil emulsion drops that are stabilized with surfactants. Monodisperse drops self-assemble in a well-ordered hexagonal close-packed lattice. [77] When the oil between the aqueous drops evaporates, drops start to deform to form a prismatic

hexagonal pattern, in which the planar interfaces are stabilized by the surfactants. [77] The patterned structure with locally varying compositions and stiffness gradients across the grain boundaries can thereafter be cured using UV light, as shown in Figure 1.9d. [77]

However, these presented techniques that make use of the physics of fluids to pattern materials are again limited to two dimensions. A common method to fabricate soft materials in three dimensions is extrusion-based 3D printing, which I will address in the next subchapter.

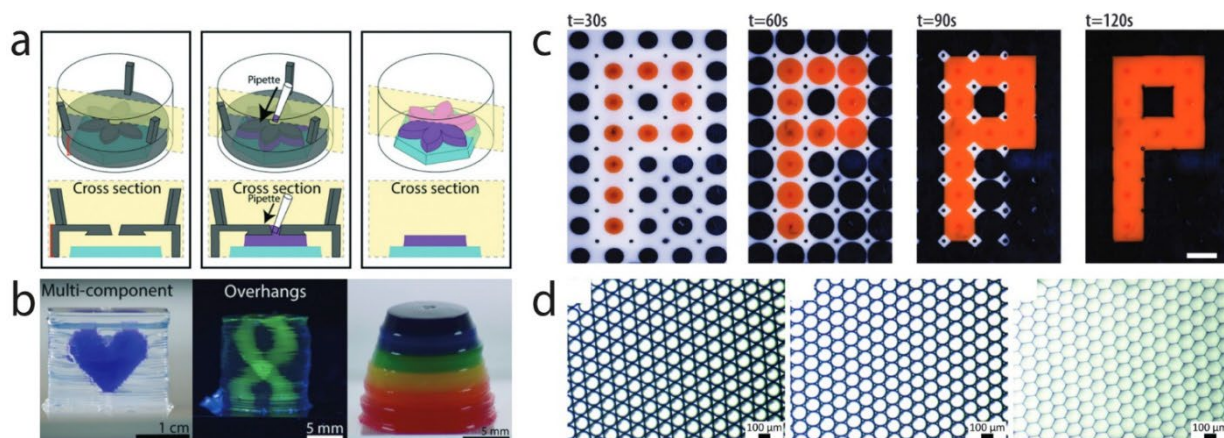


Figure 1.9: Structuring of materials using surface tension and flow. (a-b) An open microfluidic method employs (a) a freestanding mold to guide the meniscus of an aqueous phase that is subsequently polymerized to form (b) multi-component, overhanging structures, as well as material gradients. (c) Elastomer patterning inside a Hele-Shaw cell using laminar flow. Scale bar = 2.5 cm. (d) Hexagonal patterning of surfaces using water-in-oil drops. The drops self-assemble in a hexagonal close-packing (left) before the oil starts to evaporate (center), leading to a continuous hexagonal pattern after the oil is fully evaporated (right). (a-b) Adapted with permission from [78]. Copyright 2022 Royal Chemical Society. (c) Reprinted with permission from [76]. (d) Adapted with permission from [77]. Copyright 2022 American Chemical Society.

1.6.5 Patterning via 3D Printing

A technique that allows to shape hydrogels in three dimensions is extrusion-based 3D printing. [94], [95] There are well-defined rheological requirements for a precursor to be printable into a freestanding structure. An extrudable ink needs to yield at a pressure the printer is able to exert onto the ink. It needs to be shear-thinning, which means that the viscosity of the ink decreases with increasing pressure. Finally, an ink must be shape-retaining at atmospheric pressure, meaning that it stops to flow as soon as the pressure that is applied during the extrusion is removed. These rheological properties can be obtained by adding rheological modifiers, such as nanoparticles, clay or nanofibrils, to only name a few, to the precursor-containing solution. [95] One prominent example of such an ink is composed of a hydrogel precursor solution that contains cellulose nanofibrils. Upon extrusion the nanofibrils align parallel to the printing nozzle. [96] This leads to the desired rheological properties for printing, as upon alignment of the fibrils the viscosity decreases. Additionally, aligned nanofibrils lead to anisotropic swelling of the resulting crosslinked hydrogel and hence internal stresses upon swelling, which cause a deformation in three dimensions. The concept of cleverly structuring 2D films to obtain complex 3D structures via self-morphing, which I have reviewed in a previous subchapter, is hence translated to the world of 3D printing. [96] More detailed

information on this concept, called 4D printing [97], or more generally on 3D printing [79] can be found in recent reviews.

So far I have reviewed fabrication processes to structure hydrogels on the micrometer scale that are accomplished using one step: precursor solutions, that may contain hard fillers such as fibers, are brought into a desired shape before polymerization, or are locally selectively polymerized. This one-step processing strongly limits the control over the local chemical composition and mechanical properties, such as stiffness or toughness, within 3D printed materials.

Nature can fabricate materials with very well defined, abruptly changing compositions and structures. In the next chapter, I will closer examine an intricate structure fabricated by an animal that features spatial variations in composition and structure on the micron to submicron scale. It shows extremely advantageous mechanical properties such as stiffness and toughness, which is caused by complex chemistry, but to a big share by its locally varying compositions. Its fabrication process shows both temporal and spatial complexity, and adds yet another mechanism to the fabrication process: compartmentalization of precursors that are subsequentially assembled.

1.7 Compartmentalization to Fabricate Microstructured Hydrogels

1.7.1 Inspiration from the Mussel Byssus

A prominent example of a natural hydrogel that shows exceptional fracture energy is the mussel byssus, an acellular holdfast with which mussels attach themselves to the rocky seashore. The byssus strands are composed of a fibrous core that is surrounded and protected from abrasion by a cuticle layer, which is fivefold harder than the fibrous core while still being fairly stretchy. [98]–[101] It has been observed that mussel species living in the peaceful subtidal region produce a cuticle that undergoes catastrophic failure at around 30% strain, while the cuticle of species that are exposed to heavy waves in the intertidal zone only breaks at around 70% strain, as shown in Figure 1.10a and 1.10b, respectively. [100] A fundamental difference between the cuticles produced from subtidal and intertidal species is their microstructure. Subtidal species produce a spatially homogeneous cuticle. In contrast, the cuticle of intertidal species that withstands higher stretches shows a granulated microstructure consisting of stretchy and soft inclusions surrounded by a continuous matrix, as shown in Figure 1.10c. [100], [102]. Interestingly, prior to catastrophic failure of the granulated cuticle, microcracks form within the matrix, which are blunted by the granules. [98], [100] These microcracks, also called tears, are shown in Figure 1.10d. The crack arresting leads to voids and cavities that eventually coalesce at high strains. This crack blunting mechanism induced by the granulated microstructure may hence explain the high strain at break compared to unstructured cuticles.

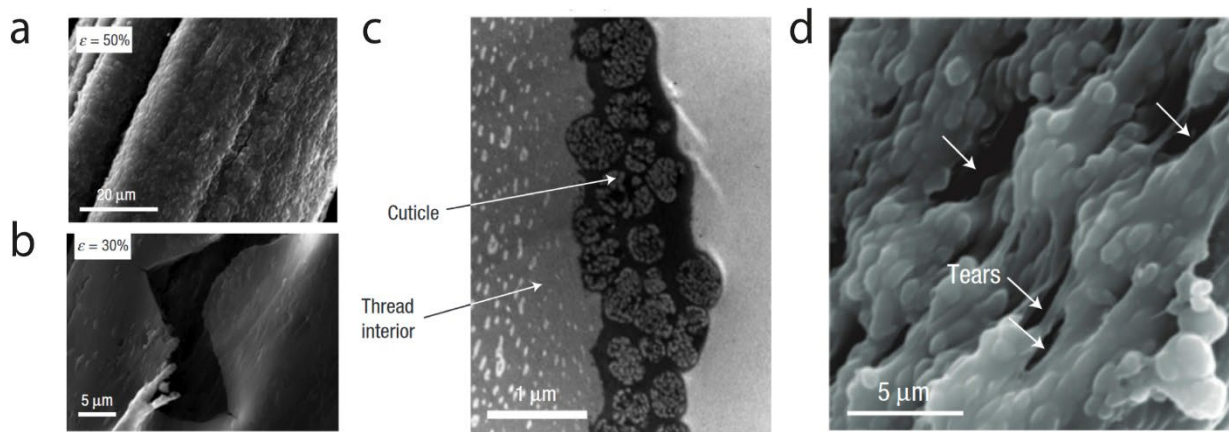


Figure 1.10: The microstructure of the mussel byssus and its cuticle layer. (a,b) SEM images of a mussel byssus strand of a (a) intertidal species at 50% strain and (b) a subtidal species at 30% strain that underwent catastrophic failure. (c) TEM image of a cross-section of the mussel byssus showing the thread interior and its protective microstructured cuticle. (d) SEM image of a granulated cuticle with microcrack formation and void opening. (a-d) Reprinted and adapted with permission from [100].

The intrinsic tradeoff between hardness and extensibility, that many biological and industrial coatings suffer from, is overcome in the byssus cuticle by a granulated microstructure. As similar types of crosslinks are used inside and outside of the granules, which are covalent and coordinated crosslinks, [103], [104] the interface is strong and does not weaken the material.

1.7.2 Processing of the Mussel Byssus

The question arises how the mussel produces such a tough and strong material at atmospheric pressure, solely with the resources available in their direct environment. Additionally, the byssus fabrication is rapid, it takes only a couple of minutes. [105] An important factor that leads to the microstructure as well as the strong interfaces is the use of prefabricated precursors that are stored at high concentrations within compartments. Upon material production, these precursors are released and self-assemble into superstructures. Thereby, the precursors used for the core, the cuticle, or the plaque, which is responsible for strong adhesion to rocks, are separately produced and stored and can be locally released. [99]

The fibrous core is built from liquid crystalline precursors that are pre-ordered via self-assembly during storage in the secretory vesicles. [99] Those precursors are subsequently assembled on larger scales in the foot groove via a biologically controlled process that includes mechanical forces to form the fibrous core, reminiscent of a fiber pulling process. [99] Similarly, the membrane-bound precursors of the cuticle are pre-assembled in the cuticle glands and consist of two immiscible protein phases: a proto-granule, rich in DOPA proteins, surrounded by the proto-matrix, rich in sulfur. [106] Similar to the precursors of the core, the pre-assembly of the liquid-liquid core-shell structures in compartments is guided by a thermodynamic process, which is phase separation. [106] A cross-section of the mussel foot that shows the cuticle vesicles full of precursors is shown in Figure 1.11a. Upon secretion into the mussel foot and onto the fibrous core, the proto-matrix coalescences and the precursors spread to result

in a continuous granular coating. [106] Coalescing proto-matrices in a cuticle gland prior to release onto the core are shown in Figure 1.11b. Thereby, the proto-granules retain their shape. Note that there is a clear temporal sequence between core and cuticle formation. [99] Further, the mechanical reinforcement of these protein-based structures through the formation of metal ion coordination bonds takes place during a second step via infiltration of metal ions, including iron and vanadium. [106] The process of precursor secretion, assembly, coalescence and reinforcement with metal ions has been nicely summarized by Jehle et al., as shown in Figure 1.11c [106].

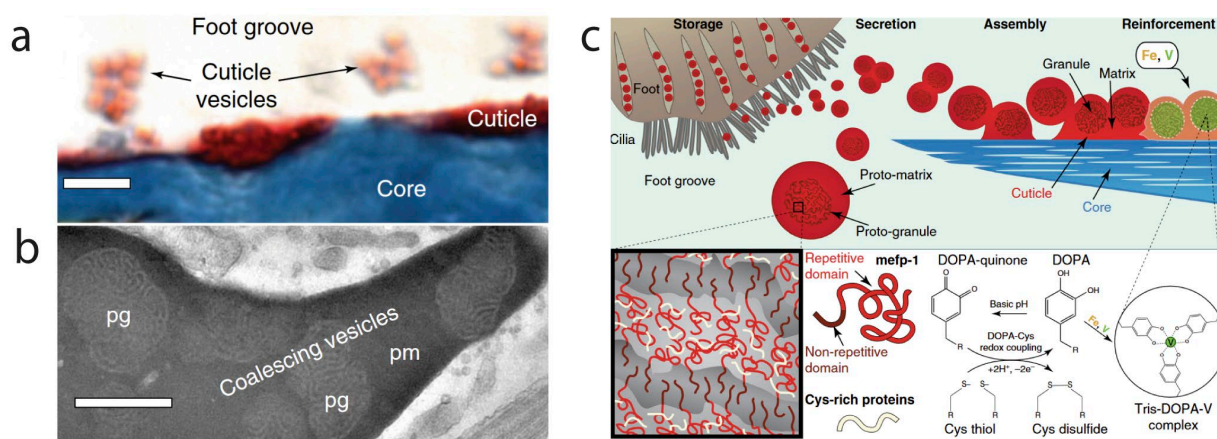


Figure 1.11: Fabrication of the mussel byssus cuticle. (a) Histological longitudinal thread section showing coalescing cuticle precursors inside the cuticle vesicles and spreading on the core. (b) TEM image of a cuticle gland showing vesicles that are about to be released onto the core. While the proto-granules remain in their shape the surrounding proto-matrix is coalescing. (c) Schematic illustration of the cuticle fabrication process. Stored cuticle precursors are secreted onto the fibrous core where they spread to build a continuous coating. The cuticle is mechanically reinforced in a second step by metal ion coordination complexes. Adapted from ref. [106] under the Creative Commons License.

The mussel developed a highly intricate process to fabricate mechanically strong and tough polymeric materials, which includes the formation of precursors via thermodynamic processes, their assembly through temporal and spatial sequences, and biologically guided processing steps such as fiber drawing. Key to this process is the compartmentalization, in which precursors are first produced and separately stored at high concentrations before they are assembled into a bulk, highly structured material. A process that bears not the same complexity as the one employed for the fabrication of the mussel byssus, but resembles it in terms of prefabrication of components, followed by their assembly, is microgel-based fabrication of bulk hydrogels.

1.7.3 Microgels as Building Blocks

The IUPAC definition of microgels reads as “particle of gel of any shape with an equivalent diameter of approximately 0.1 to 100 μm .” [107] They start to be heavily used in biomedical engineering [108] especially in cell culturing, [109] but more recently also in adhesion science [110] and soft robotics. [111]

Microgels are pre-fabricated and assembled into a macroscopic structure in a second step. This two-step process bears a great advantage in terms of design freedom, as microgels can be pictured as individual and modular building blocks that are assembled to form a designer bulk material. This freedom of design to fabricate three-dimensional structures using microgels with different functionalities like LEGO® building blocks was nicely demonstrated: in a proof-of-concept example magnetic, thermo-responsive, and light-sensitive microgels were assembled into a multifunctional superstructure. [112] The structure can reversibly contract upon light exposure or heating to move through restrictions, re-swell to grip cargo, while it is steered through a maze using a magnetic field. [112] In another example, host-guest interactions and hydrogen bonds are employed to assemble different batches of microgels with different compositions and functionalities that are used for cell culturing and to build an optoelectronic device. [113]

1.7.4 Fabrication of Microgels

Microgels can be prefabricated using various methods that have been thoroughly reviewed and were nicely presented by Daly et al., [108] here reprinted as Figure 1.12. I will present some essential methods and give examples in which they have been employed. The most common method to fabricate microgels is batch emulsification, in which an aqueous hydrogel precursor solution is emulsified to form water-in-oil drops. The monomers contained in the drops are subsequently polymerized using UV light, to transform drops into microgels before the microgels are washed. [108] This method has a relatively high throughput and is easily applicable to the production of spherical microgels that are polydisperse. However, the degree of control over the size of the microparticles is limited. [114] An emulsion-based method to obtain monodisperse, spherical drops that can be converted into microgels with well-controlled sizes is to employ microfluidic devices. Water-in-oil drops are produced using micron-sized channels that to a big extent determine the size of the resulting drops. [115]–[117] However, microfluidic methods still suffer from relatively low throughputs. Hence, the throughput must be traded off with the microgel size control. I would like to point out that the fabrication methods presented above, such as molding or photolithography are also applicable for the fabrication of microgels: molded, highly anisotropic microgels were used to guide the alignment of nerve cells for injectable reconstituting implants. [118] A microfluidic technique is used to fabricate large, anisotropic, cell-laden microgels that can be directly printed into tissue engineering platforms using the outlet tubing. [119] A photolithographic technique is used to pre-fabricate cell-laden microgels that are subsequently assembled into superstructures within an oil bath. [120] However, while these last three methods allow to fabricate designer microgels, even with controlled aspect ratios, they suffer from a limited throughput.

A high throughput method to produce microgels is mechanical fracturation. However, compared to other methods presented so far, this technique offers very limited control over the microgel size and shape. Nevertheless, ball milling has been used to fabricate a microgel-based bio-inspired glue for haemostatic sealing. [110]

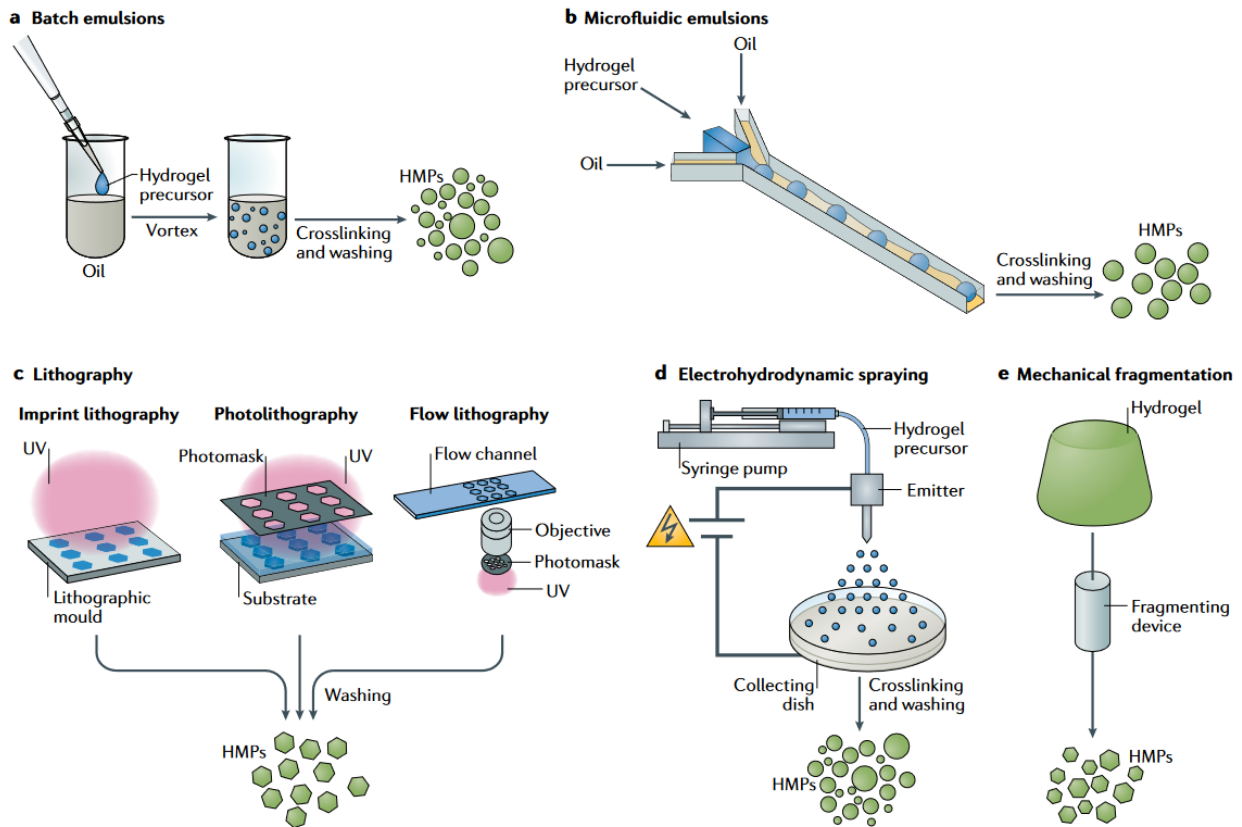


Figure 1.12: Summary of the production of hydrogel microparticles (HMPs), herein called microgels. Reprinted from [108] with permission. Copyright by Springer Nature 2020.

1.7.5 Assembly of Microgels

There are different methods to assemble microgels into three-dimensional structures, as has been shown in a recent review. [108] This includes, for small scale assemblies, the use of acoustic waves [121], tiny robots [122], or microfluidic rails [123] or channels. [113] However, for the assembly of microgels into bigger structures molding or extrusion-based 3D printing are often employed. To enable 3D printing, microgels are often up-concentrated until they touch each other and hence, experience inter-microgel friction. These jammed microgels are indeed excellent inks for 3D-printing as they fulfill the rheological conditions for extrusion that I have presented above: [108], [124] Due to inter-microgel friction, they resist gravity and do not undergo spontaneous flow. When a pressure that exceeds the yield stress of the jammed microgel is applied, microgels start to flow, which leads to a shear-thinning behavior. Once the pressure is removed, the friction between microgels prevents them from flowing, which makes them shape-retaining. [125] The shape and size distribution of microgels influences their rheological behavior if jammed: non-spherical microgels show a higher yield stress and display more friction than spherical ones. [114] Due to these rheological properties, microgels can be directly printed into free-standing structures [126] or they can be used as supportive bath to support other printed structures before their solidification. [127], [128]

The implementation of microgels, which can be pictured as pre-fabricated precursors of the bulk hydrogel, somewhat resembles the two-step fabrication process of the mussel byssus with spatial and temporal complexity. Additionally, bulk hydrogels fabricated from microgel templates intrinsically feature a microstructure that can be controlled by tuning the properties of the microgels. Using microgels as building blocks for the fabrication of bulk hydrogels is hence a straight-forward mean to study the influence of the microstructure on the mechanical properties of bulk hydrogels. I will now discuss how microgels can be used to fabricate microstructured hydrogels that feature the double network toughening mechanism.

1.8 Mechanics of Tough, Microgel-Reinforced Hydrogels

Traditional double networks are usually fabricated in a two-step process that includes swelling of the molded first network in the precursor of the second network, before the second network is polymerized. [34] The swelling of the first network limits the dimensional control of the final piece and complex shapes cannot be achieved. A way to overcome this swelling step after molding is to introduce the first network not as a continuous bulk hydrogel, but as microgels. [129] This allows to fully swell the microgels in the precursor solution of the second network prior to molding. The swelling step is hence done prior to the shape-giving process such that it does not compromise the shape fidelity of molded or 3D printed parts.

From a mechanical point of view, it was observed that two independent PAMPS sheets can be strongly linked together purely by the second network. [130] Peeling tests revealed that if the crosslinker concentration of the second network is optimized, the hydrogel with the discontinuous first network could match the fracture energy of a double network with a continuous first network. [130] Two distinct PAMPS hydrogel sheets strongly linked together solely by the second network during a peeling test are shown in Figure 1.13a. The same mechanically strong linkage of non-continuous PAMPS components by the second network also takes place if not two distinct PAMPS hydrogel sheets are used, but if the first network is added as a fine powder of microgels instead. [130] Interestingly, if the crosslinker density of the second network is properly adapted, the fracture energy of the microgel-reinforced hydrogels can even exceed the fracture energy of a classical bicontinuous double network, as shown in Figure 1.13b. [130] The continuity of the first network is hence not needed to reach a high fracture energy. [130] This was, for example, demonstrated on microgel-reinforced hydrogels composed of PAMPS microparticles that were embedded in a second PAAm network. The volume fraction of the microgels and the molar ratio between the PAMPS and the PAAm inside the microgels are the important factors that determine the mechanical properties of the resulting material. [131] Using cyclic loading experiments it was revealed that the ratio between the total dissipated energy and the amount of present PAMPS chains is more than threefold higher for microgel-reinforced hydrogels compared to bicontinuous DN's. The dissipated energy per cycle normalized by the number of available PAMPS chains is shown as a function of the maximum strain of each cycle in Figure 1.13c. [132] Further, the bulk double network is initially much stiffer than the granular counterpart. However, already after having been stretched to 200%, the stiffnesses of the bicontinuous double network and the microgel-reinforced hydrogels are similar.

[132] The initial moduli of bicontinuous DN's, pure PAAm and microgel-reinforced hydrogels as a function of the maximum strain a sample underwent during the previous cycle are shown in Figure 1.13d. This may strengthen the view of Gong that initially load-bearing PAMPS chains aligned in direction of pull break, causing the rapid decrease of Young's modulus as a function of the maximum strain per cycle.

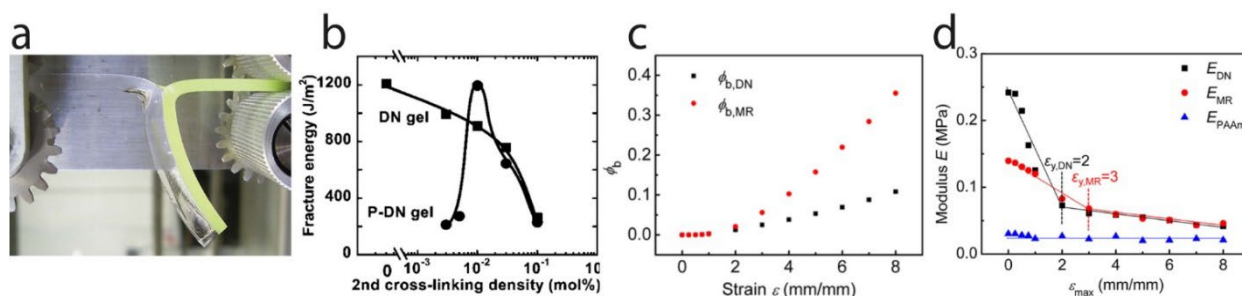


Figure 1.13: Double network hydrogels with discontinuous first networks. (a) Image of a peeling test of a sample consisting of two separate PAMPS sheets that are connected by the second network. The same fracture energy is obtained as for a bicontinuous double network hydrogel. (b) Fracture energy as a function of the crosslinking density of the second network for a bicontinuous double network (DN gel) and a hydrogel with a particle-based first network (P-DN gel), herein called microgel-reinforced hydrogel (MRH). (c) Cumulative fraction of broken c-c bonds in the first network during cyclic loading for a double network hydrogel (black) and a microgel-reinforced hydrogel (red) as a function of the maximum strain of every cycle. (d) Evolution of the Young's modulus during cyclic loading for a double network hydrogel (black), a microgel-reinforced hydrogel (red), and pure polyacrylamide (PAAm) as a function of the maximum strain of every cycle. (a-b) are adapted from [130] with permission. Copyright 2011 American Chemical Society. (c-d) are adapted from [132] with permission. Copyright 2012 American Chemical Society.

1.9 Applications of Engineered Hydrogels

Traditional human-made robots and machines often rely on feedback loops that consist of a sensor to sense environmental factors, a computer to analyse the recorded data and to steer a third, active component that will move or react. These components, as well as the electronic data transmission between them, often rely on stiff and bulky components, which makes the entire system unsuitable for many applications. This is in stark contrast to many plants, in which small local changes in soft components lead to macroscopic actuation. [133] Concept-wise, it would hence, also for human-made machines and robots, be favourable to make use of machine building blocks that locally sense their environment and at the same time react to it. Many soft materials do show this desired feature and are intrinsically responsive to their environment, making them fascinating building blocks for smart systems, [134], [135] or physically intelligent systems. [136] For soft robots and machines, hydrogels are excellent candidates for this endeavour, [137], [138] as they react to stimuli such as temperature [92], [139]–[142], ionic strength [143], pH [144] or, when properly designed, to light [90] or magnetic fields [145], [146]. Hydrogel “machines” [137], [138] can hence be used for applications such as soft robots [147]–[149], microgrippers, [90], [92] microswimmers [145], [146], or drug delivery vehicles. [150] However, only the recent progress in terms of mechanical properties of hydrogels, such as stiffness and toughness, enabled their more frequent use in real-life applications. [2], [61]

Hydrogels that are strong and tough are, due to their high water content, also brilliant candidates for interfaces between the human body and artificial systems. This includes the interface between the human body and electronic devices, and has been widely reviewed, [151] or with a focus on conductive hydrogels. [152] Additionally, tough hydrogels are excellent candidates to be used as wound sealing, which has been shown using a bulk hydrogel tape [153] or particle-based hydrogel wound sealings. [110] Lots of fascinating developments have been done in the field of tough hydrogels, opening up daily life applications society will benefit from. Thereby, microgel-reinforced hydrogels, or more generally, granular hydrogels, show great advantages in terms of design freedom and processing. In my thesis I will address how the size and shape of microgels influence the stiffness and toughness of microgel-reinforced hydrogels.

Chapter 2

Scope of the Dissertation

Progress in engineering domains, such as biomedical engineering or soft robotics, often goes hand in hand with the development of new materials that can withstand more load than their predecessors. A lot of ongoing research efforts are therefore devoted to the development of advanced soft materials that are strong and tough. To achieve this endeavor, nature is a constant source of inspiration, as natural soft materials are still superior in terms of combining stiffness and toughness, compared to their synthetic counterparts. A major difference between natural and synthetic soft materials is their structuring. While natural materials are often structured on different length scales, many synthetic soft materials still lack structuring on the micro and meso length scales and have only well-defined structures on the molecular level. In this dissertation, I investigate how the microstructure of hydrogels influences their mechanical properties, such as stiffness and toughness, and introduce a microfluidic device that provides superior control over the microstructure of hydrogel sheets. I hope that the present work will contribute to the advancement of stiff yet tough hydrogels, and to introduce functionalities into them.

Structure of the Dissertation

The dissertation is divided into four following chapters. In chapter 3, I investigate how the size and volume fraction of reinforcing microgels influence the processing and the resulting strength and energy-dissipative mechanisms of microgel-reinforced hydrogels. In chapter 4, I address how the volume fraction of microgels, their size, and degree of swelling influence the stiffness and fracture energy of microgel-reinforced hydrogels. In chapter 5, I present a microfluidic Hele-Shaw cell featuring capillary traps that enables the fabrication of hydrogel sheets with abrupt compositional changes on the 100 μm length scale. The chapters 3 and 5 are based on published, peer-reviewed papers, to which I contributed as a first author. Chapter 4 is adapted from a manuscript that is in preparation for submission, to which I contributed as a first author. Finally, I conclude the present work with a conclusion and an outlook on future research in chapter 6.

Chapter 3

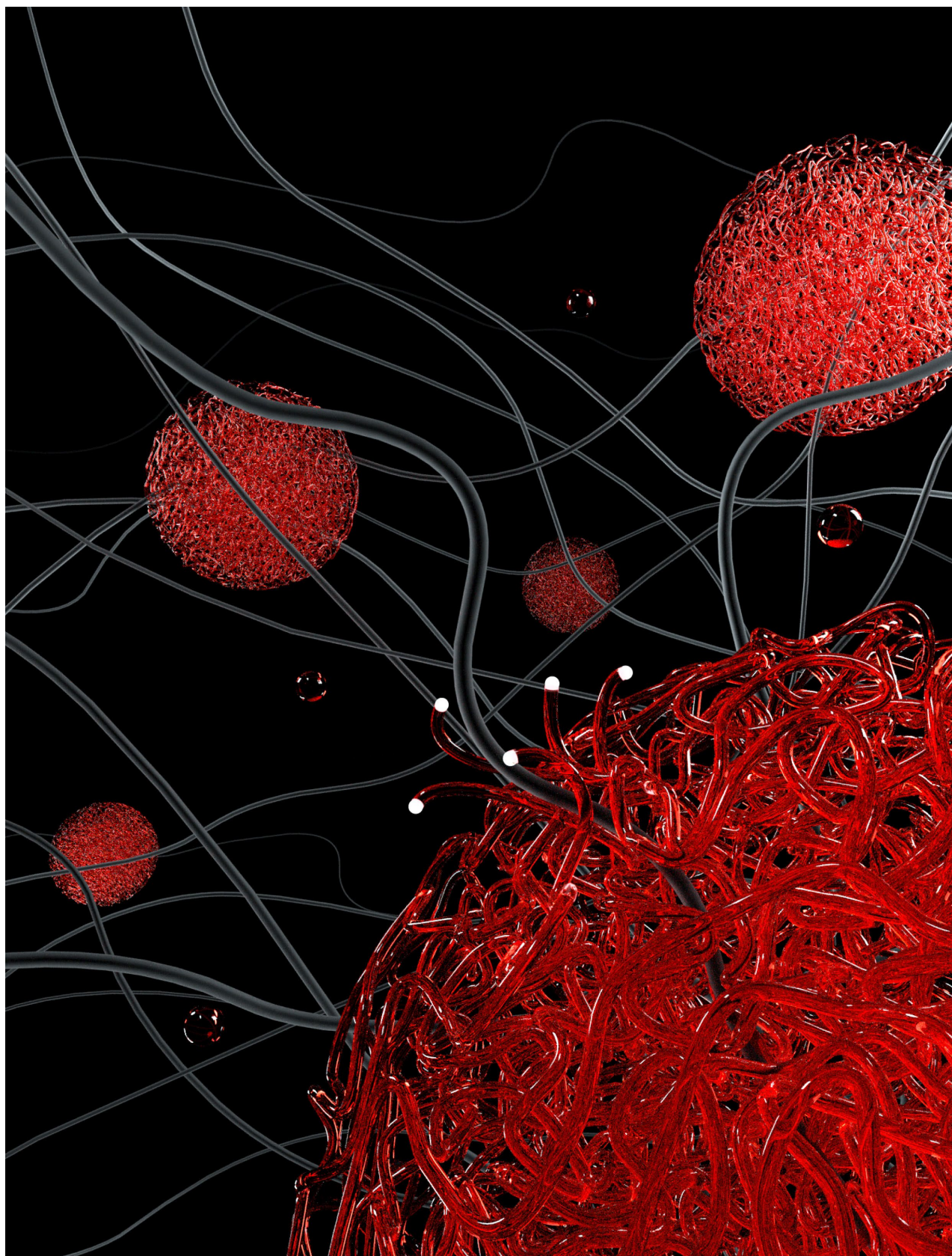
Does the Size of Microgels Influence the Toughness of Microgel-Reinforced Hydrogels?

In this chapter we investigate how the size and the size distribution of microgels influence the rheological properties of the hydrogel precursors and hence their processing, and the mechanical properties such as stiffness and toughness of the resulting hydrogels. We find that the stiffness and the bulk swelling of microgel-reinforced hydrogels are insensitive to the microgel size. By contrast, the energy dissipation and the stress at break of hydrogels reinforced with microgels depend on their size.

The chapter is adapted from the published paper “Kessler, M., Nassisi, Q. and Amstad, E. (2022) ‘Does the Size of Microgels Influence the Toughness of Microgel-Reinforced Hydrogels?’, *Macromolecular Rapid Communications*, n/a(n/a), p. 2200196. doi:[10.1002/marc.202200196](https://doi.org/10.1002/marc.202200196)., authored by Michael Kessler, Quentin Nassisi, and Esther Amstad.

Michael Kessler and Esther Amstad designed the study. Michael Kessler and Quentin Nassisi performed the experiments, Michael Kessler and Esther Amstad analyzed the data and wrote the manuscript.

We would like to thank Alice Cont from the UPPERSAT lab, EPFL, for assistance with the confocal microscope. We thank Constance Bouquerel for experimental help and Matteo Hirsch, Alvaro Charlet, Mathias Steinacher, Huachuan Du, and Robert Style for fruitful discussions. This work was financially supported by the Swiss National Science Foundation (SNSF, 200020_182662).



Cover design made by Tianyu Yuan, SMaL, accepted for the front cover of the journal issue.

3.1 Abstract

Rapid advances in the biomedical field increasingly often demand soft materials that can be processed into complex 3D shapes while being able to reliably bear significant loads. Granular hydrogels have the potential to serve as artificial tissues because they can be 3D printed into complex 3D shapes and their composition can be tuned over short length scales. Unfortunately, granular hydrogels are typically soft such that they cannot be used for load-bearing applications. To address this shortcoming, individual microgels can be connected through a percolating network, such that they introduce the double network toughening mechanism into granular hydrogels. However, the influence of the microgel size and concentration on the processing and toughness of microgel-reinforced hydrogels (MRHs) remains to be elucidated. Here, we demonstrate that processing and toughness depend on the inter-microgel connectivity, while the stress at break is solely dependent on the microgel size. These findings offer an in-depth understanding of how liquid- and paste-like precursors containing soft, deformable microgels can be processed into bulk microstructured soft materials and the effect of the size and concentration of these microgels on the mechanical properties of microgel reinforced hydrogels.

3.2 Introduction

Double network hydrogels (DN's) are among the first manmade hydrogels to combine high stiffness and toughness, thereby resolving an intrinsic trade-off between extensibility and stiffness crosslinked single-network hydrogels suffer from. [34], [154] Double network hydrogels are composed of a first sacrificial network that dissipates a significant amount of energy when covalent bonds contained in it are broken, and a second network that is loosely crosslinked to maintain the mechanical integrity of the hydrogel. [35] This mechanism introduces an exceptional combination of toughness and stiffness to hydrogels. [34], [36] Bulk DN's are fabricated in a two-step process: The first network is often formed by pouring a precursor solution into a mold before the precursors are polymerized. This network is swollen in a second precursor solution that is subsequently polymerized. Yet, due to this two-step process that includes swelling of the initial bulk material, dimensional control of the resulting sample is lost, limiting the field of applications of DN's. To overcome this limitation, microgel-reinforced hydrogels (MRHs) have been introduced. [129], [131], [132], [155] Microgels are hydrogel microparticles with diameters in the range of 1-1000 μm . [108] They reinforce bulk hydrogels if embedded in the same [156] or a different type [129], [157] of a percolating bulk hydrogel. MRHs are produced by swelling pre-fabricated microgels in the precursor solution of the matrix that is optionally processed into an appropriate shape before the precursor solution is solidified by polymerizing the precursors contained in it. [157] This microgel prefabrication step offers the distinct advantage that the dimensions of the resulting sample can be controlled as the swelling of the first network takes place before the desired shape is fixed, as opposed to classic DN processing.

The processing of microgel-loaded precursor solutions depends on the microgel volume fraction Φ : Precursor solutions containing low volume fractions of microgels behave as liquids. [129] By contrast, precursor solutions containing microgel volume fractions above a jamming threshold, which is $\geq 58\%$, depending on the microgel

characteristics, behave as pastes. [130], [158] Precursor solutions constituted of jammed microgels are shear-thinning, display a low yield stress and a fast shape recovery such that they are excellent inks for extrusion-based 3D printing. [108], [124] The rheological properties of jammed microgels strongly depend on their shape and size: non-spherical microgels fabricated via mechanical fragmentation have a higher shear modulus G' compared to spherical microgels due to increased inter-microgel friction. [114] Further, monodisperse microgels show a higher G' than their polydisperse counterparts. [114] This feature arises from the higher effective volume fraction of monodisperse microgels, defined as the ratio of the volume fraction and the maximum packing fraction, that is caused by the lower maximum packing fraction. [159] Lastly, small microgels offer a better printing fidelity than larger counterparts. [160] However, if not contained within a percolating hydrogel matrix, the resulting 3D printed granular hydrogels are soft because adjacent microgels are weakly or sparsely connected. We recently introduced 3D printable load-bearing double network granular hydrogels (DNGHs) composed of jammed poly(2-acrylamido-2-methylpropane sulfonic acid) (PAMPS) microgels that are connected through a percolating poly(acrylamide) (PAAm) network. The percolating network interpenetrates the microgels, thereby distributing the stress much more homogeneously throughout the material than inter-microgel links that are limited to their surfaces do. [125] As a result, the DNGHs are at least 4-fold stiffer than any other previously reported 3D printable hydrogel. Unfortunately, little is known on how the microgel size affects the mechanical properties of microgel-reinforced materials. The stiffness, stress and strain at break, and work to break of dilute systems containing microgel volume fractions below 30% is primarily determined by the molar ratio between PAMPS and PAAm and the microgel volume fraction. [131] The toughening of MRHs caused by the microgels is mainly due to internal damages occurring within individual microgels. The extent to which microgels toughen MRHs depends on the size of microgels and the stress concentration around them. [155] It has been nicely shown that adjacent microgels show pronounced, highly localized damage in the close vicinity of their neighboring microgels. [155] However, these effects were solely analyzed optically on the microscale such that their effect on the macroscopic mechanical properties of MRHs remains to be elucidated. Moreover, the influence of the dimensions and concentration of microgels on the rheological properties that determine the processability of the precursor solutions remains to be determined.

In this chapter, we study the influence of the microgel size and inter-microgel connectivity on the stiffness and toughening mechanism of MRHs. We demonstrate that the stress at break of microgel-reinforced hydrogels is directly related to the microgel size. The microgel size also affects the rheological properties of the precursor solution and hence, its processability: larger microgels lead to a higher stress at break of MRHs because these microgels break over a wider strain range compared to their smaller counterparts. By contrast, small microgels predominantly break at low strains if contained at high volume fractions within a bulk hydrogel because they are strongly connected through it. As a result of the strong inter-microgel connections, MRHs reinforced with small microgels yield and hence display a low stress at break. These findings open up new routes for advanced design and processing of MRHs that might enable their use as artificial tissues or soft robots.

3.3 Experimental Section

3.3.1 Microfluidic Device Fabrication

We produce a microfluidic millipede device from poly(dimethylsiloxane) (PDMS) (Sylgard 184, Dow Corning, USA) using soft lithography. The height of the nozzles is fixed to $h = 10\text{ }\mu\text{m}$, to result in emulsion drops with diameters of $58 \pm 3\text{ }\mu\text{m}$. [116] The surface of the PDMS device is made fluorophilic by injecting a HFE7500 solution (Novac, 3M, USA) containing 2 vol% trichloro-(1H,1H,2H,2H-perfluorooctyl)silane into the channels. The solution is kept in the channels for 15 minutes before being removed with compressed air.

3.3.2 Microgel Production

Microgels are produced from water-in-oil emulsion drops. The aqueous phase contains 20 wt% 2-Acrylamido-2-methylpropane sulfonic acid (AMPS) monomer (Sigma-Aldrich, USA), 3 wt% of N,N-methylene bisacrylamide (MBAA) (Carl Roth, Germany), a crosslinker, and 5 $\mu\text{l/ml}$ of 2-hydroxy-2-methylpropiophenone (Sigma-Aldrich, USA), a photo-initiator. The oil phase is composed of light mineral oil (Sigma-Aldrich, USA) containing 4 wt% Span80 (TCI Chemicals, Japan), a commercial surfactant. To produce small, polydisperse emulsions, we add the oil and aqueous phase at a volume ratio of 3:1 into a 50 ml falcon tube and agitate this tube with a vortex mixer during three times 30 seconds. To produce large, monodisperse emulsions, we employ microfluidic devices. We reduce the surfactant concentration in the oil phase to 1 wt%. We inject the water-phase into the microfluidic millipede device at a flow rate $Q = 1\text{ ml h}^{-1}$ and the oil phase at $Q = 2\text{ ml h}^{-1}$ using syringe pumps (Cronus Sigma 1000, Labhut, UK). The produced drops are collected in a vial containing mineral oil with 4 wt% Span80 to ensure good drop stability during collection. Emulsion drops are converted into microgels by polymerizing the monomers contained in them for 5 minutes using a UV lamp ($320\text{ nm} < \lambda < 500\text{ nm}$, $P = 100\text{ W}$) (Omnicure S 1000, Lumen Dynamics, Canada) at a distance of 5 cm between the emulsion surface and the light guide. After polymerization, the excess oil is removed and the microgels are washed three times with pure mineral oil to remove the surfactant. The hydrophilic microgels are then transferred into water, which is changed three times to remove unreacted monomers. The fully swollen microgels are frozen using liquid nitrogen and placed in a freeze-dryer (FreeZone 2.5, Labconco, USA) at 0.03 mbar and -53°C for at least five days to fully dry the microgels. A white powder is obtained, which is thereafter protected from humidity until its utilization.

3.3.3 Microgel Characterization

The size distributions of the different microgel batches as-prepared, swollen in water, or swollen in the matrix precursor solution are measured from optical microscopy images. The diameters of the microgels and their size distribution are analyzed using imageJ and $N > 100$ microgels for each dataset. Images of the freeze-dried microgels are taken using a scanning electron microscope (Gemini, Carl Zeiss, Germany). The microgels are fixed on the sample holder with carbon tape and coated with 20 nm of Au (Q150 Plus, Quorum Technologies, UK). The

energy of the electron beam is set to 3 kV and the working distance to 6 mm. The images are recorded using a secondary electron detector.

3.3.4 Microgel Swelling

The swelling ratio r is defined as D_{sw}/D_{ap} . Here, D_{sw} is the microgel diameter if fully swollen in water and D_{ap} that in the as-prepared state if dispersed in oil.

3.3.5 Fabrication of Microgel-Reinforced Hydrogels (MRHs)

To fabricate MRHs the required amount of dried microgels is weighted in an Eppendorf tube using a microbalance. An aqueous acrylamide (AAM) (Sigma-Aldrich, USA) solution containing 30 wt% AAm, 0.1 wt% MBAA relative to the monomer concentration, and 1 μ l/ml of photo-initiator is pipetted into the Eppendorf. The resulting solution is protected from light with aluminum foil and left overnight at ambient temperature to ensure that the microgels swell to equilibrium in a solution containing AAm.

Depending on their rheological behavior, the solutions are either pipetted or poured into molds to fabricate MRH samples. The monomers contained in the precursor solution are polymerized in an UV oven ($\lambda = 365$ nm, $P = 2$ mW cm^{-2}) (UVP CL-1000, Analytik Jena, Germany). Molded samples for mechanical testing and bulk swelling experiments are produced in PTFE molds that are covered with glass slides. The monomers are polymerized for 15 minutes. 3D printed samples are manufactured using a commercial bio 3D printer (BIO X, Cellink, Sweden) and are subsequently polymerized for 15 minutes.

3.3.6 Microgel Volume Fraction Measurements

The microgel volume fractions in the samples are measured using a confocal microscope (Nikon Eclipse Ti2-E inverted microscope). Sheet-like samples are produced in a customized mold made of two glass slides that are separated by scotch tapes. To image samples reinforced with small, polydisperse microgels we employ 60 μ m thick spacers, to image those reinforced with large, monodisperse microgels we use 300 μ m thick spacers. To render the microgels fluorescent, we add 5 μ g of Cresyl Violet Perchlorate (Sigma-Aldrich, USA) per mg of microgels to the AAm solution. The samples are illuminated with UV light for 5 minutes for crosslinking the matrix precursor solution. Z-stacks are recorded using a confocal microscope and the area fraction is found by thresholding each z-slice. The volume fractions are calculated as the average of all the z-slices of a z-stack. Three z-stacks are recorded and analyzed for each dataset.

3.3.7 Tensile Testing

For mechanical testing dogbone-shaped samples with a thickness and width of 2 mm and 5 mm, respectively, and a gauge length of 10 mm are produced. They are tested with a Universal Tensile Test Machine Zwicky 5 kN (Zwick Roell, Germany) with a 50 N load cell. The samples are gripped with a pressure of 3.5 bar using a hydraulic clamping system. The test speed is 100 mm/min and a preload of 0.005 N is applied before the start of the test. For stress-

strain curves at least two precursor solutions are produced per data point and at least three samples are tested for each precursor solution type. For stress-strain curves of MRHs containing 40 wt% AAm at least three samples per datapoint are tested. Young's moduli are analyzed by linearly fitting the data curves between 5 and 15% strain. The work to break W_b is defined as the area under the stress-strain curve of an un-notched sample. For cyclic testing the samples are loaded to ε_{max} of a given cycle and then unloaded to $\varepsilon = 0$. The sample is left to relax for 10 seconds and then loaded to ε_{max} of the next cycle, until rupture of the sample. The dissipated energy ΔU_{hys} of a given cycle is calculated as the area between the loading and unloading curve between $\varepsilon = 0$ and ε_{max} of any given cycle. The compressive stress at $\varepsilon = 0$ is recorded as the first value of the loading curve. For cyclic testing at least three samples are produced and measured for each datapoint.

3.3.8 Bulk Swelling Measurements

To measure the bulk swelling of MRHs, discs with a diameter of 7.7 mm are produced. They are soaked in deionized water for a week and their swollen diameter is measured using a digital caliper. The swelling ratio is defined as the diameter ratio between the fully swollen and as-prepared disks. For each datapoint three disks are produced and analyzed.

3.3.9 Rheological Measurements

Rheological measurements were performed at room temperature using an 8 mm diameter parallel plate geometry and a gap of 1 mm. Frequency sweeps were performed at 0.5% oscillation strain. Amplitude sweeps were performed at an angular frequency of 1 rad/s. Three experiments were conducted per microgel concentration.

To determine the contribution of the inter-microgel friction to the overall sample stiffness, we perform an *in situ* gelation experiment on the rheometer. An AAm precursor solution containing 25 g/l microgels is loaded on the rheometer at room temperature and its storage modulus G' is measured. At $t = 50$ s the UV lamp is switched on to initiate the polymerization of the PAAm network while G' is recorded. We use a DHR-3 TA Rheometer with an 8 mm diameter parallel plate steel geometry and the gap is set to 800 μm . The strain is fixed to 1% strain and the frequency to 10 rad s^{-1} .

3.4 Results and Discussion

3.4.1 Fabrication of Microgel-Reinforced Hydrogels (MRHs)

To control the size of microgels, we fabricate them from water-in-oil emulsion templates. Large emulsion drops are produced in a parallelized microfluidic device, the millipede device [116], as depicted in Figure 3.1a. Small emulsion drops are made by mixing an aqueous solution containing the microgel precursors with the oil containing surfactants and vortexing it, as schematically shown in Figure 3.1b. To prepare microgels that strongly swell such that they can be loaded with a large quantity of the matrix precursors we employ an electrolyte monomer, AMPS. We use mineral oil as a continuous phase because it has a much lower O_2 -solubility than the fluorinated oils that are more commonly used in microfluidics. [161], [162] Too high concentrations of O_2 tend to terminate radical polymerization reactions and hence hamper the conversion of emulsion drops into integral microgels. The fabrication process of microgel-reinforced hydrogels starting from emulsion templates is depicted in Figure 3.1c. Emulsion drops are converted into microgels by exposing them to UV light to initiate the radical polymerization of the precursors contained in them. The resulting microgels are washed and fully swollen in water before they are freeze-dried to obtain a fine powder, as shown on SEM images in Figure 3.1d and 3.1e. The obtained powder can be precisely weighted to control the microgel content within MRHs. The dried microgels are swollen overnight in the acrylamide (AAM)-based matrix precursor solution, as depicted in Figure 3.1c and shown in the optical micrographs in Figure 3.1f and 3.1g. The resulting mixtures are molded or printed before the matrix precursors are polymerized to obtain MRHs with controlled microgel volume fractions. The diameter of large microgels is $147 \pm 15 \mu\text{m}$, resulting in a coefficient of variation (CV) of 10%, whereas their small counterparts are five-fold smaller and more polydisperse with diameters of $32 \pm 10 \mu\text{m}$ and a CV of 30%, as shown in Figure 3.1h and 3.1i. The microstructures of the resulting MRH samples reinforced with large or small microgels are schematically shown in Figure 3.1j and 3.1k, respectively. Note that while small microgels do not show sedimentation we observe sedimentation of the large microgels over tens of minutes. However, the relatively fast polymerization process used here ensures that microgels are homogeneously distributed within our MRHs.

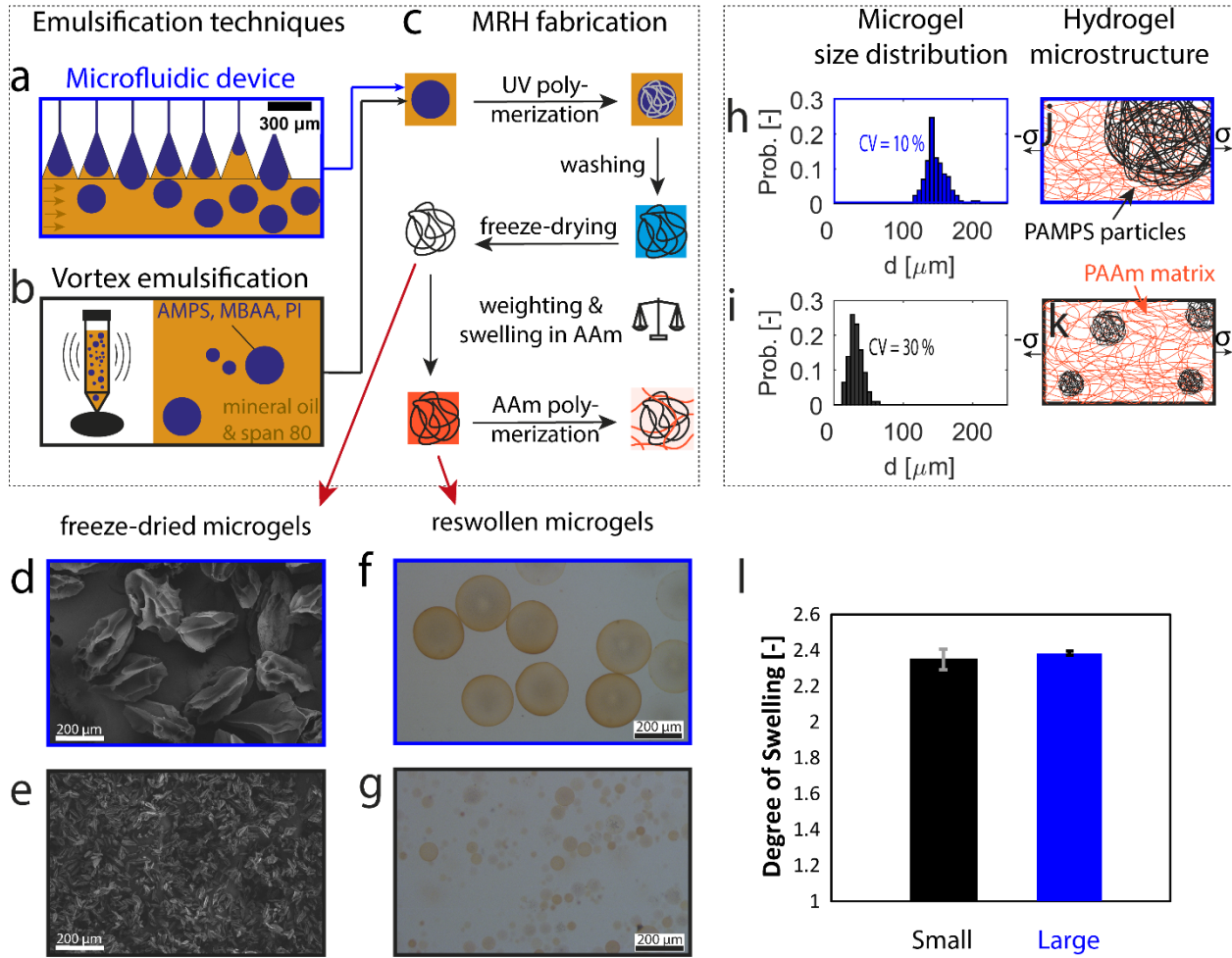


Figure 3.1. Fabrication of microgel-reinforced hydrogels (MRHs). (a-b) Schematic illustrations of the emulsification (a) with a microfluidic millipede device to produce large water-in-oil drops and (b) through vortexing to produce small, polydisperse water-in-oil drops. (c) Drops are converted into microgels through UV polymerization of the monomers contained in them. Microgels are washed, freeze-dried, weighted and swollen in an acrylamide (AAm) solution, which is subsequently polymerized. (d-e) SEM images of freeze-dried microgels for (d) large and (e) small microgels. (f-g) Optical micrographs of reswollen (f) large and (g) small microgels. (h-i) Size distribution of the (h) large and (i) small microgels swollen in deionized water. (j-k) Schematic illustrations of the resulting microstructure of MRH reinforced with (j) large and (k) small microgels. (l) Microgel degree of swelling for small microgels and two different batches of large microgels. Reproduced from [163] under the Creative Common License.

To study the influence of the microgel size on the stiffness and toughness of MRHs their stiffness must be identical. Because our microgels are produced from identical precursor solutions their stiffness is inversely proportional to their swelling ratio, as their osmotic swelling is solely limited by the stiffness of their network. [14] To test if the size of emulsion drops influences the degree of polymerization of precursors contained in them and hence the stiffness of microgels, we quantify their swelling ratio as a function of their size, as detailed in the subchapter 3.3.4. We do not observe any influence of the microgel size on their swelling ratio, as shown in Figure 3.1l. Hence, we can exclude any effect of the drop size or emulsification method on the stiffness of our microgels.

3.4.2 Microgel Volume Fraction

The stiffness and toughness of MRHs strongly depends on the microgel volume fraction. [131] To enable systematic studies of the microgel size on the stiffness and toughness of MRHs, we must ensure equal microgel volume

fractions Φ . The experimental parameters that affect Φ are the microgel swelling ratio, the initial monomer content and the mass of dry microgels that is added to the sample. These factors are found after following calculations.

Theoretical Calculation of Microgel Volume Fraction

The volume fraction of microgels is calculated as the volume occupied by them divided by the sample volume. The volume occupied by fully swollen microgels V_{sw} can be calculated as:

$$V_{sw} = \frac{m}{\rho_{sw}}. \quad (3.1)$$

Here, m is the polymer mass of the microgels, and ρ_{sw} is the polymer mass per volume of swollen microgels. The polymer mass in a microgel population can be calculated from the as-prepared, unswollen state:

$$m = \rho_{ap} V_{ap}. \quad (3.2)$$

Here, ρ_{ap} is the polymer mass per volume of as-prepared microgels when dispersed in oil (wt%/vol%), which is the monomer weight added per volume of the aqueous solution. V_{ap} is the volume of as-prepared microgels. As the polymer weight in a microgel population is the same in the as-prepared and the swollen state we find

$$\frac{\rho_{ap}}{\rho_{sw}} = \frac{V_{sw}}{V_{ap}} = r. \quad (3.3)$$

Here, r is defined as the volume swelling ratio between the swollen and the as-prepared state of microgels. The resulting volume occupied by a microgel population is hence

$$V_{sw} = \frac{m \cdot r}{\rho_{ap}}. \quad (3.4)$$

Because the swelling ratio of the two microgel batches is equal, we expect them to yield in the same Φ if equal amounts of dry microgels are added to the precursor solutions. To test our expectation, we perform confocal microscopy on our MRHs. To facilitate visualization of the microgels, we fluorescently label them with a positively charged dye, cresyl violet, as exemplified in Figure 3.2a. [164] We find that Φ indeed linearly increases with increasing mass of added microgels, independent of their size, as summarized in Figure 3.2b. The slightly higher datapoint for large microgels at 5 g/l can be attributed to preferential spreading of the aqueous matrix precursor solution along the hydrophilic glass mold, an effect that is inhibited by the higher apparent viscosity precursor solutions containing higher microgel volume fractions display. Representative thresholded z-slices for samples reinforced with large and small microgels with different volume fractions are shown in Figure 3.2c-h.

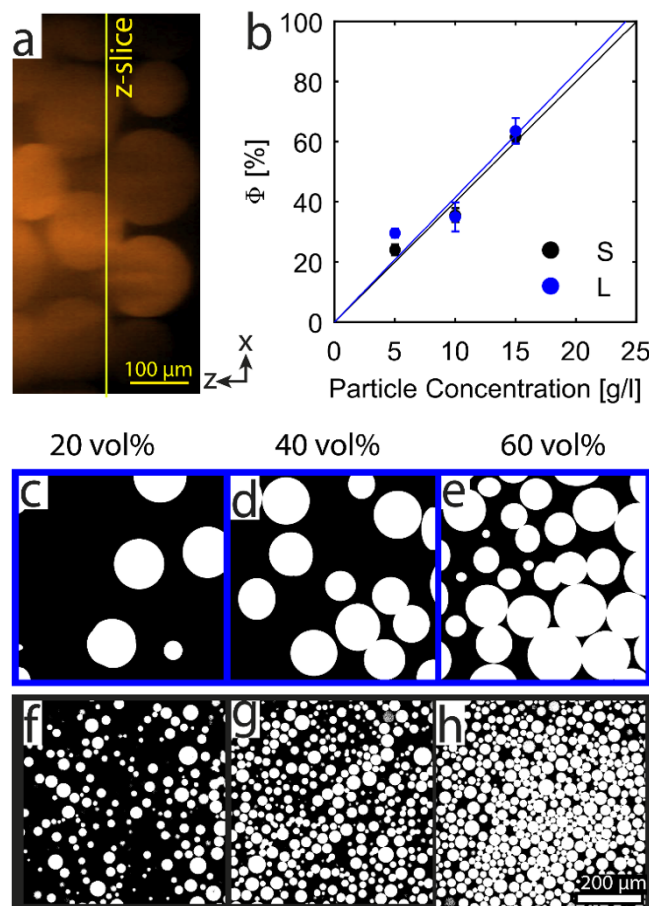


Figure 3.2. Microgel volume fractions. (a) Confocal microscopy image of a MRH reinforced with 60 vol% stained large microgels. The yellow line indicates a z-slice. (b) Microgel volume fraction ϕ as a function of the added dry microgel mass. The solid lines are linear fits of the experimental data. (c-h) Thresholded z-slices of MRHs reinforced with (c-e) large or (f-h) small microgels. The images correspond to (c,f) 20 vol%, (d,g) 40 vol%, and (e,h) 60 vol% microgels. Note that the presented images are z-slices where the microgels appear more polydisperse than they are in three dimensions, as not all of them are imaged in their center. Reproduced from [163] under the Creative Common License.

3.4.3 Processing of Microgel-Loaded Precursor Solutions into MRHs

The processing of microgel-containing precursor solutions depends on their rheological properties. For example, liquid-like mixtures can be readily injection-molded whereas paste-like mixtures are excellent inks for 3D printing as they are shape-retaining and shear-shinning. [108] To assess the processability of our precursor solutions we quantify the jamming transition of microgels swollen to equilibrium in the matrix precursor solution as a function of the microgel volume fraction. Solutions containing 20-40 vol% small microgels behave as liquids. Increasing the volume fraction of these microgels to 60% or above results in a paste-like behavior, as qualitatively shown in Figure 3.3a. This jamming transition is supported by the rheology of our microgel-loaded precursors: the plateau modulus G_p , defined as the plateau value of G' at small amplitudes, abruptly increases when Φ exceeds 40 vol%, as shown in Figure 3.3b. Remarkably, for matrix precursors containing large microgels, the liquid-solid transition occurs at a higher microgel volume fraction: while precursor solutions containing small microgels display the solid-liquid transition at 60 vol%, those containing large microgels show this transition only at 80 vol% microgels, as qualitatively

shown in Figure 3.3c. Indeed, G_p of these precursors increases 550-fold when Φ is increased from 60 to 80 vol%, as shown in Figures 3d. The viscosities for small and large microgels follow a similar trend, as shown in Figure 3.4a and 3.4b, respectively. The threshold volume fraction above which microgels start to jam depends on their shape [114], polydispersity [114], external conditions such as pressure and temperature, [14] and most likely also on their size. Here, we change two parameters simultaneously: the size and polydispersity. However, monodisperse microgels [15] and colloidal particles [24] jam at lower volume fractions than their polydisperse counterparts because they possess a lower maximum packing fraction and hence, higher effective volume fraction. [16] Nevertheless, in our case, small, polydisperse microgels jam at lower volume fractions than large monodisperse counterparts despite their polydispersity. From this observation we deduce that smaller microgels jam at lower volume fractions, due to an increased inter-microgel contact area and hence friction. This increased friction for smaller microgels also manifests itself in the values of G_p : While precursors containing large microgels have a G_p of 3525 ± 490 kPa, the G_p of their small counterparts is 1.5-fold higher, 5280 ± 330 kPa.

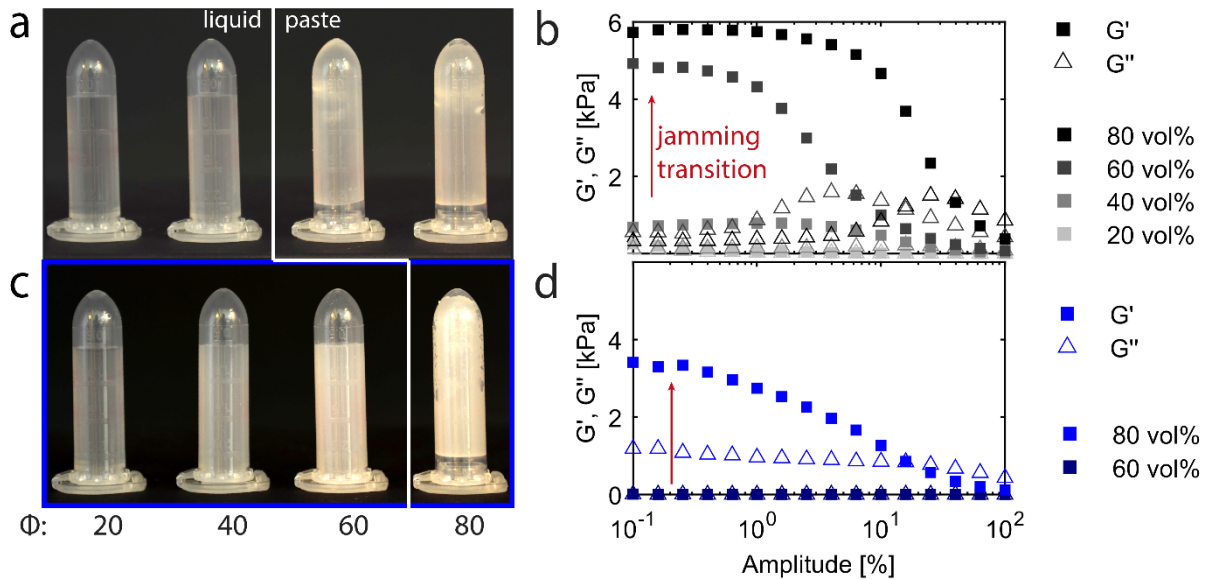


Figure 3.3. Rheological properties of microgel-loaded precursor solutions. (a,c) Precursor solutions containing varying volume fractions of (a) small or (c) large microgels. (b,d) Representative amplitude sweeps of precursor solutions containing (b) small or (d) large microgels as a function of the microgel volume fraction. (b,d) The red arrows indicate the jamming transition. Reproduced from [163] under the Creative Common License.

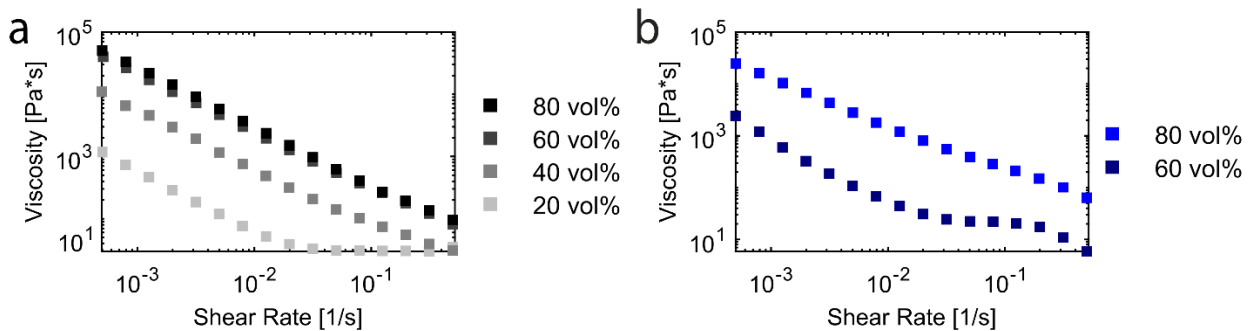


Figure 3.4. Representative frequency sweeps of precursors containing different volume fractions of (a) small or (b) large microgels. Reproduced from [163] under the Creative Common License.

3.4.4 Mechanical Properties of MRHs

Inter-microgel friction between jammed microgels leads to an elastic material at low strains and a G' of order of 100-1000 Pa. [25] To quantify the contribution from the inter-microgel friction to the stiffness of MRHs, we polymerize a matrix precursor solution containing 25 g/l microgels *in situ* on a rheometer. Upon polymerization of the second network, G' increases by an order of magnitude from 6 kPa to 60 kPa, as shown in Figure 3.5. This result indicates that the inter-microgel friction does not significantly influence the elasticity of MRHs, even if the microgel volume fraction is high.

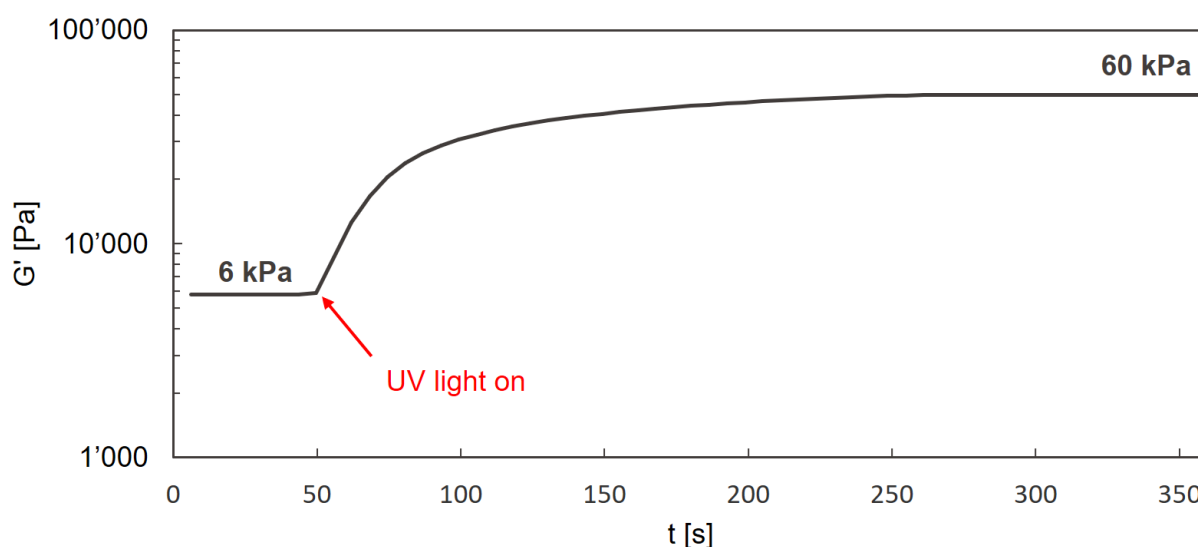


Figure 3.5. G' of a mixture containing 100 vol% small microgels before and after the UV light is turned on to crosslink the second network. Reproduced from [163] under the Creative Common License.

The stiffness of bulk hydrogels reinforced with low microgel volume fractions increases with increasing concentration of microgels contained in these gels. [6] To assess if this is also the case for hydrogels reinforced with much higher volume fractions of microgels, we perform tensile tests on our MRHs. Representative stress-strain curves are shown in Figure 3.6. The stiffness of our MRHs linearly increases with increasing Φ until it reaches 60%, independent of the microgel size, as shown in Figure 3.6 and 3.7a. This result further demonstrates that the two different batches of microgels possess the same stiffness. By contrast, the stiffness of MRHs depends on the particle size if the microgel volume fraction exceeds 60%: the stiffness of MRHs containing small microgels plateaus at 60 vol% and becomes even lower at 80 vol%, as shown by the black datapoints in Figure 3.7a. We assign the reduction in E at 80 vol% to the highly jammed state of the small microgels and the therewith associated high viscosity of the precursor solution that favors air entrapment, and hence the introduction of voids. MRH samples that are void-free and those featuring air entrapments are shown in Figure 3.8a and 3.8b, respectively. Note that the inclusion of air is independent of the processing method as 3D printed samples containing 80 vol% microgels display a similar

stiffness as their molded counterparts, as shown by the star-shaped datapoint in Figure 3.7a. By contrast, the stiffness of hydrogels reinforced with large microgels increases monotonically with Φ , as shown by the blue datapoints in Figure 3.7a. These results suggest that solutions encompassing large microgels entrap air less efficiently and hence, are less prone to introducing defects into MRHs if processed at high volume fractions.

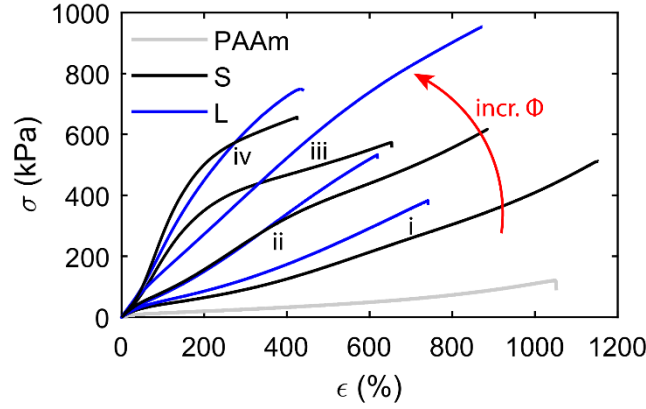


Figure 3.6: Representative stress-strain curves for hydrogels reinforced with small (black) and large (blue) microgels whose volume fraction is $\Phi =$ (i) 20 vol%, (ii) 40 vol%, (iii) 60 vol%, (iv) 80 vol%. Reproduced from [163] under the Creative Common License.

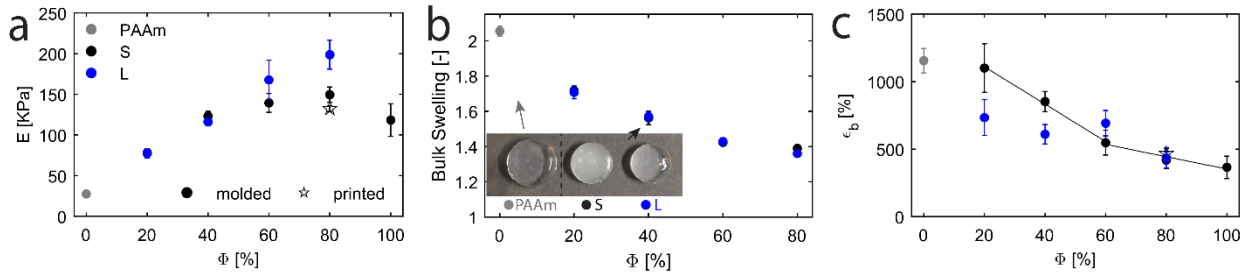


Figure 3.7. Mechanical properties of MRHs. (a-c) (a) Young's modulus E , (b) bulk swelling and (c) strain at break ϵ_b as a function of the microgel volume fraction Φ . Inset in (b): Photographs of fully swollen MRHs made of pure PAAm (left), and reinforced with 40 vol% small (center) or large (right) microgels. (c) The lines are linear fits to the experimental data. Reproduced from [163] under the Creative Common License.

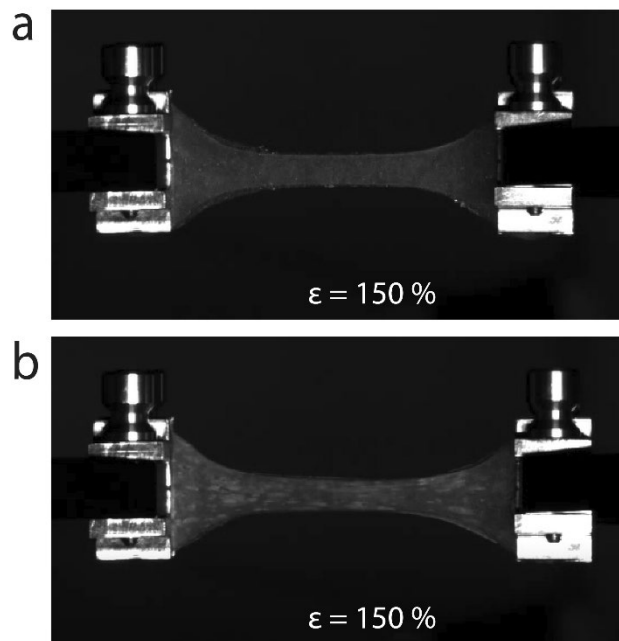


Figure 3.8. Images of MRHs loaded on the tensile tester that are stretched to 150% strain. (a) A homogeneous pore-free MRH reinforced with 60 vol% large microgels. (b) A heterogeneous, porous MRH reinforced with 100 vol% small microgels. Reproduced from [163] under the Creative Common License.

The stiffness of hydrogels typically depends on the density of crosslinks and physical entanglements. [2] The density of entanglements increases with increasing concentration of precursors the hydrogels are made from. [2] To test if this is also the case for our samples, we increase the concentration AAm in the precursor solution from 30 to 40 wt%. Indeed, if the AAm concentration is increased from 30 to 40 wt%, the stiffness increases 1.7-2.5-fold, depending on Φ , as shown in Figure 3.10a.

The stiffness of MRHs that do not encompass air entrapments is independent of the microgel size, and hence a volume property. Because the stiffness of hydrogels is directly related to their degree of swelling, we expect the swelling of MRHs to also be a volume property and hence, be independent of the microgel size. Yet, the degree of swelling of MRHs should linearly decrease with increasing volume fraction of microgels because pre-swollen microgels are stiffer than the free-standing matrix. To test this hypothesis, we fabricate disc-shaped MRHs and swell them in deionized water to equilibrium. We indeed find that the bulk swelling decreases with increasing Φ , independent of the microgel size, as shown in Figure 3.7b. However, we observe a nonlinear decrease of swelling with increasing Φ that goes beyond the rule of mixture. We attribute this difference in swelling behavior to an increased PAAm concentration around the microgels compared to that within the particles, which reduces the swelling of the free-standing matrix: the solubility of AAm within microgels is lower than that in the surrounding such that the AAm concentration within the surrounding increases with increasing volume fraction of added microgels. This increased AAm concentration translates into an increased entanglement density of the polymerized network. A gradient in PAAm concentration across the microgel surface was reported by others and thought to be responsible for light scattering. [5], [6] We also observe an increased turbidity of MRHs reinforced with smaller microgels, compared to their counterparts reinforced with large microgels, as shown in the inset photographs in

Figure 3.7b. However, we assign this increased turbidity to the increased total microgel surface area present in MRHs reinforced with small microgels as these surfaces scatter light.

An important factor that contributes to the toughness of MRHs is their elongation at break ε_b . For hydrogels reinforced with small microgels, ε_b decreases with increasing Φ , as shown in black in Figure 3.7c. While samples containing only 20 vol% small microgels break at 1200%, a value similar to the pristine PAAm, it decreases to 400% strain at 80 vol% microgels. Similar trends are observed for samples made from solutions containing 30 and 40 wt% AAm, as shown in Figure 3.10b. We attribute this observation to the densification of the PAAm outside the microgels, which renders the free-standing matrix more brittle. These results support our findings from the swelling experiments on the heterogeneity of the PAAm matrix. At low microgel volume fractions, ε_b decreases rapidly with increasing Φ of small microgels until the AAm concentration in the surrounding solution saturates. Once saturation is reached, the decrease in ε_b with increasing microgel volume fraction becomes slower, as indicated by the two distinct, monotonically decreasing slopes of the linear fits in Figure 3.7c. Note that a similar trend with two differently decreasing slopes was found for highly polydisperse non-spherical microgels, although this feature has previously not been interpreted. [158]

Our results suggest that MRHs containing a high volume fraction of large microgels are significantly stiffer than those containing the same volume fraction of small counterparts. We attribute the lower stiffness of MRHs reinforced with small microgels to the air inclusions that are present within these samples. However, because tough materials, like our MRHs, are rather flaw-insensitive, defects, such as the observed air inclusions, do not significantly lower the strain at break, such that the microgel size does not influence ε_b , as shown in Figure 3.7c.

Another parameter that influences the toughness of materials is the stress at break σ_b . This parameter increases with increasing volume fraction of small, polydisperse microgels until it reaches 40 vol% where it starts to plateau, as summarized in Figure 3.9a. Note that samples reinforced with 60 or 80 vol% of small microgels start to yield if sufficiently strained, as can be observed in Figure 3.6iii and 3.6iv. This yielding limits σ_b . This behavior is in stark contrast to MRHs reinforced with large microgels for which no yielding is observed such that they display a significantly higher σ_b than MRHs containing small microgels. These results suggest that large microgels stiffen MRHs over a more extended strain range than their smaller counterparts. To assess if this difference can be assigned to the molding process, we 3D printed the samples. 3D printed samples containing 80% small microgels display a similar σ_b as their molded counterparts, indicating that these values are related to the precursor composition and independent of their processing. However, note that the AAm concentration present in the precursor significantly increases σ_b at high Φ , as shown in Figure 3.10c. We attribute this increased σ_b for an increased initial AAm concentration to a higher entanglement density and hence increased sample stiffness.

A measure of the toughness of any material is its work to break W_b , herein defined as the area under the stress-strain curve of an un-notched sample. The work to break of hydrogels reinforced with small microgels displays a

maximum at 40 vol%, as shown in Figure 3.9b. By contrast, W_b of hydrogels reinforced with large microgels reaches a maximum at 60 vol%. We obtain similar results for 3D printed samples, confirming that the processing method does not influence the mechanical properties of MRHs. Remarkably, for both small and large microgels the maxima in W_b are reached for samples made from precursors loaded with the highest microgel volume fraction that still behave as liquids, as can be seen in Figure 3.3a and 3c. Note, that a similar trend with distinct maxima has already been observed, yet these maxima were not correlated to the rheological properties of the precursor solutions. [13] These results suggest that a liquid precursor solution leads to a well-percolated matrix that still provides extensibility to the sample, opposed to samples with higher Φ .

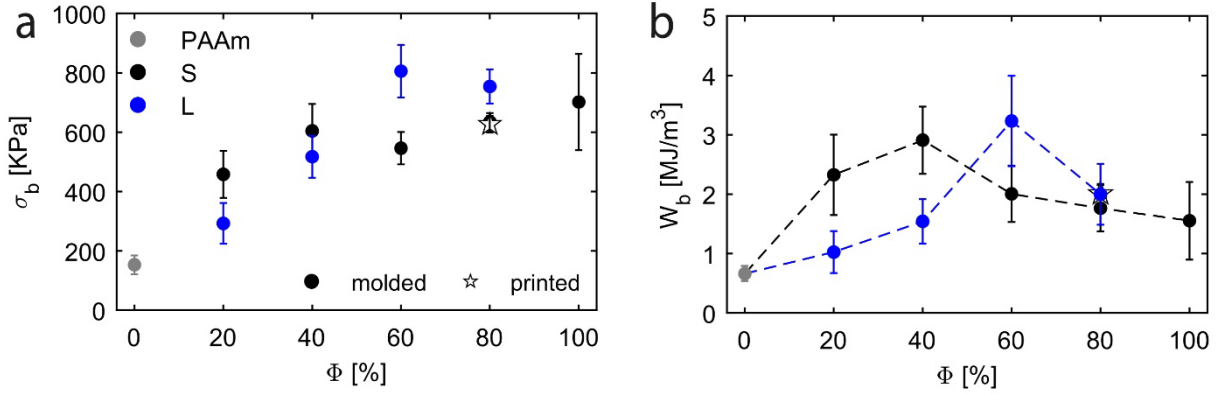


Figure 3.9. Mechanical properties of MRHs. (a) Stress at break σ_b and (b) work to break W_b as a function of the microgel volume fraction Φ (b) The dotted lines are guides to the eye. Reproduced from [163] under the Creative Common License.

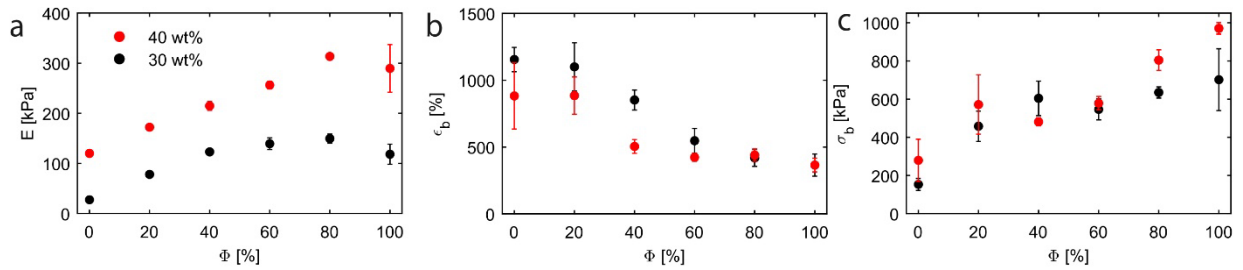


Figure 3.10. Influence of the PAAm concentration on the mechanical properties of MRHs. (a) Young's modulus E , (b) strain at break ϵ_b and (c) stress at break σ_b as a function of the microgel volume fraction Φ . Reproduced from [163] under the Creative Common License.

3.4.5 Toughening of MRHs

Effect of the Microgel Connectivity

To better understand the toughening mechanism and yielding behavior some of the samples display, we calculate the first derivatives of the stress-strain curves, as exemplified in Figure 3.11a. The first derivative is a measure of how much tensile stress needs to be applied to a sample to stretch it by one unit. MRHs typically dissipate stress

by irreversibly breaking PAMPS chains. [5] Microgels contained at low volume fractions within hydrogels have been shown to efficiently break if there are stress concentrations around them; the degree of stress concentration depends on the size of microgels and their connectivity. [8] To test if we observe a similar trend for hydrogels reinforced with a high volume fraction of microgels, we compare samples reinforced with small microgels as a function of their volume fraction. The $d\sigma/d\varepsilon$ curves show clear peaks at $\varepsilon = 100\%$ for samples reinforced with 60 and 80 vol% microgels, as shown in Figure 3.11b. These results suggest that a majority of jammed microgels breaks within a limited strain range. In contrast, we do not observe any clear peak for hydrogels reinforced with 40 vol% small microgels, indicating that dispersed microgels stiffen MRHs over a wide range of ε . Note that at strains $> 230\%$, the dilute sample containing 40 vol% microgels possesses higher $d\sigma/d\varepsilon$ values than those containing higher microgel volume fractions. We assign this remarkable effect to the stress transfer between individual microgels: at volume fractions of 60 vol% or above the small microgels are jammed. The free-standing matrix around the microgels, which is enriched with PAAm, efficiently transfers stress between the different microgels. This effect leads to pronounced breaking of the small microgels already at strains as low as 100%. Samples reinforced with large microgels only display a clear peak of the $d\sigma/d\varepsilon$ curve if they contain 80 vol% microgels, as shown in Figure 3.11c. These observations align well with the ones made for the work to break W_b : samples that show a clear peak in Figure 3.11b and 11c are the ones made from paste-like precursors, which feature high inter-microgel connectivity, efficient load transfer between the microgels and hence efficient breakage of PAMPS chains at relatively low strains.

Effect of the Microgel Size

Our results suggest that the network matrix around the microgels and hence, the efficiency of stress transfer between them strongly affect their breakage and consequently the toughening of MRHs. To test this suggestion and because we expect the degree of stress transfer to strongly depend on the matrix-microgel interactions in proximity to the microgel surface, we analyze the effect of the surface-to-volume ratio of microgels. [7] Samples reinforced with 20 vol% microgels are too soft such that we cannot measure any effect of the microgel size on the $d\sigma/d\varepsilon$ curve, as shown in Figure 3.11d. Hydrogels reinforced with 40 vol% microgels are stiffer at strains $< 320\%$ if small microgels are employed. By contrast, at strains $> 320\%$, hydrogels reinforced with large microgels are stiffer, as shown in Figure 3.11e. These results suggest that at low Φ an increased microgel surface-to-volume ratio favors breakage of PAMPS chains at low strains. In contrast, a smaller surface-to-volume ratio leads to a stiffening of MRHs that extends over a wider strain range. The microgel size is hence an important parameter for the design of MRHs. The same trend is observed for hydrogels reinforced with 60 vol% microgels, as shown in Figure 3.11f. Hydrogels reinforced with 80% microgels, where small and large microgels are jammed, show a clear peak of the $d\sigma/d\varepsilon$ curve for both tested microgel sizes, as shown in Figure 3.11g. However, the peak measured for samples reinforced with small microgels is more pronounced. We assign this difference again to the higher surface-to-volume ratio of these microgels that results in a more efficient stress transfer between them.

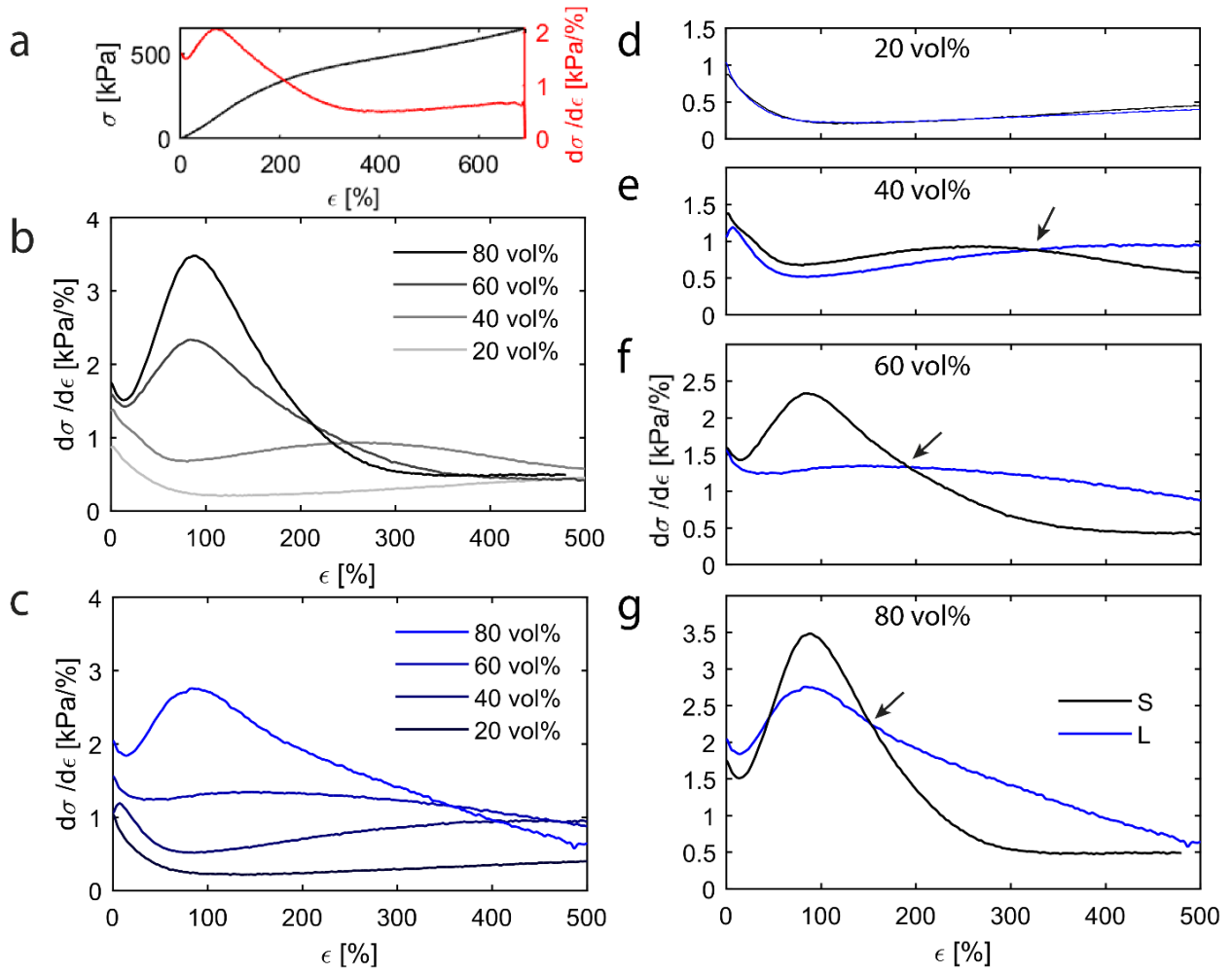


Figure 3.11. First derivatives of stress-strain curves. (a) Representative stress-strain curve (black) and its derivative (red). (b,c) Derivatives of stress-strain curves of MRHs reinforced with (b) small and (c) large microgels. (d-g) Derivatives of stress-strain curves of MRHs reinforced with (d) 20 vol%, (e) 40 vol%, (f) 60 vol%, (g) 80 vol% microgels. The black arrows indicate the crossover of the two lines. Reproduced from [163] under the Creative Common License.

3.4.6 Influence of Microgel Size on Energy Dissipation in MRHs

The derivatives of the stress-strain curves indicate how much stress is needed to increase the strain of a sample by one unit. According to the classic double-network theory, most of the stress is needed to irreversibly break covalent chains contained within the first network. [5] As a result of the irreversible bond breakage, these gels show a pronounced Mullins effect [7], [11], [26] where the enclosed area of the loading and unloading stress-strain curve can be attributed to the dissipated energy. To test whether we see an influence of the microgel size on the energy dissipation efficiency of sacrificial covalent chains and to quantify the dissipated energy of each loading-unloading cycle as a function of its maximum strain ϵ_{max} , we perform cyclic loading tests on our MRHs. As expected, our MRHs show a pronounced Mullins effect, as shown in Figure 3.12a. Hydrogels reinforced with 40% microgels exceed their elastic regime and start to dissipate energy at $\epsilon_{max} \geq 100\%$, as highlighted in Figure 3.12b. The amount of dissipated energy per cycle monotonically increases with increasing ϵ_{max} , as shown in Figure 3.12b. This result agrees well with the observation of dilute microgels that become spindle-like when broken, thereby increasing their

surface available for PAMPS chains to break. [132] At maximum strains below 420%, hydrogels dissipate more energy if reinforced with small microgels, as shown by the black datapoints in Figure 3.12b. By contrast, at strains $> 420\%$, hydrogels reinforced with 40 vol% large microgels dissipate more energy per cycle, as shown by the blue datapoints in Figure 3.12b. The observed trends are amplified in hydrogels reinforced with 60 vol% microgels, as shown in Figure 3.12c. Note that the increase in energy dissipated from hydrogels reinforced with small microgels is much slower if the maximum strains per cycle exceed 200%, as shown by the black datapoints in Figure 3.12c. We again attribute these observations to a more efficient breakage of PAMPS chains contained within small microgels at low strains and an energy dissipation that occurs over a much wider strain range for large microgels.

Our results suggest that the toughening of hydrogels with microgels is more efficient at low strains if small microgels are employed. The opposite is the case at high strains. To further test this finding, we perform cyclic loading experiments and quantify the compressive stresses that are exerted on the tensile tester at $\varepsilon = 0$ after every cycle due to plastic deformation of the sample. During cyclic loading, the elongation of the microgels and hence, the macroscopic sample increases at low strains due to breakage of short, axial chains inside the microgels, as has previously been nicely shown using optical microscopy. [8] The elongation of the macroscopic sample starts to plateau when the long axial and short transversal chains inside the microgels are simultaneously broken. At even higher ε_{max} the long transverse chains are scissioned, which reduces the sample elongation. [8] In agreement with this report, the compressive stress exerted by our hydrogels reinforced with 40 vol% microgels increases with increasing ε_{max} until it reaches a maximum of 7 kPa at $\varepsilon_{max} = 200\%$ for samples reinforced with small microgels and at $\varepsilon_{max} = 250\%$ for samples reinforced with large microgels, as shown in Figure 3.12d. The decrease in compressive stress with increasing ε_{max} thereafter is faster for samples reinforced with small microgels. These observations in bulk sample elongation further confirm our findings that small microgels break more efficiently at low strains while their large counterparts break over a much wider strain range, such that their contribution to the energy dissipation occurs over a wider strain range. Note that the values of ε_{max} above which large microgels dissipate more energy than the small counterparts are approximately 100% higher than the values of ε above which large microgels stiffen the samples more efficiently than small microgels evaluated from the $d\sigma/d\varepsilon$ curves. This shift is expected because pre-stretched PAMPS chains first stiffen the sample, an effect observed in the $d\sigma/d\varepsilon$ curves, before they break and dissipate energy, an effect measured in the cyclic loading tests. Hence, our findings indicate that the processing and mechanical properties of MRHs strongly depend on the microgel size and inter-microgel connectivity, as summarized in Figure 3.13.

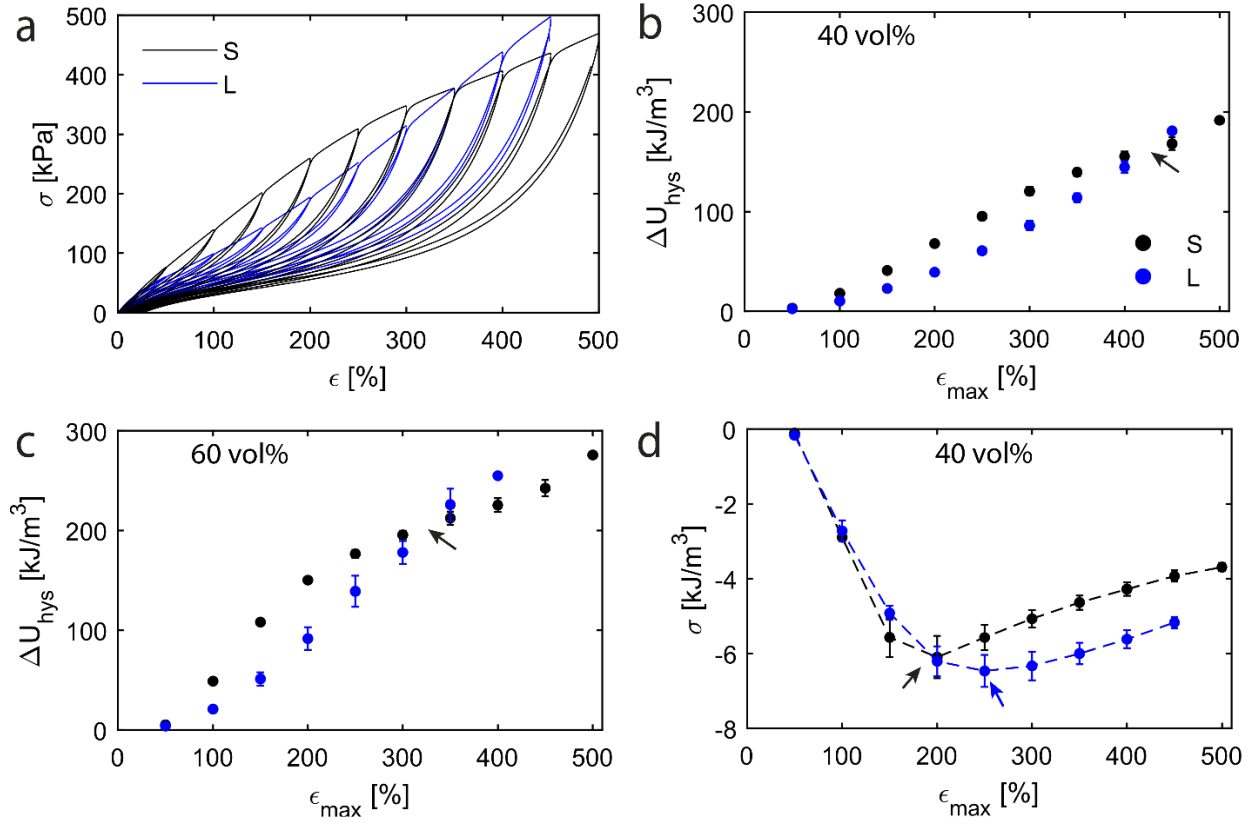


Figure 3.12. Energy dissipation of PAMPS microgels. (a) Representative cyclic loading curves of MRHs reinforced with 40 vol% small (black) or large (blue) microgels. A pronounced Mullins effect is displayed. (b,c) Dissipated energy during each loading-unloading cycle as a function of ϵ_{max} of the corresponding cycle for MRHs reinforced with (b) 40 vol% and (c) 60 vol% microgels. The arrows indicate the crossover of the two datasets. (d) Compressive stress at $\epsilon = 0$ exerted on the tensile tester as a function of ϵ_{max} of the corresponding cycle for MRHs reinforced with 40 vol%. The dotted lines are guides for the eye and the arrows represent the minima of the datasets. Reproduced from [163] under the Creative Common License.

3.5 Conclusion

Microgel-reinforced hydrogels are an attractive alternative to classic double network hydrogels because they combine stiffness and toughness with advanced processability. While paste-like precursors containing jammed microgels are excellent inks for 3D printing, liquid-like precursors encompassing individually dispersed microgels are more suited for molding applications. Small microgels jam at a lower volume fraction than their larger counterparts. Hence, small microgels are better suited for 3D printing applications as they enable tuning the microgel volume fraction and consequently the mechanical properties of the 3D printed structure over a wider range, while remaining in the jammed regime. By contrast, larger microgels are more suited for molding applications because their concentration can be varied over a wider range before they undergo the jamming transition that hampers molding. These findings are generalizable to the processing of a wide range of systems that are composed of soft and deformable microgels.

We demonstrate that at high volume fractions, larger microgels stiffen MRHs over a wider strain range than their smaller counterparts, leading to a higher stress at break. By contrast, small microgels break more efficiently at low strains, rendering MRHs reinforced with them stiffer at low strains. This in-depth understanding of the relation between the toughening effect of MRHs, that is breakage of microgels contained within them, and the macroscopic mechanical response of MRHs might enable the design of the next generation of load-bearing, granular soft materials that combine advanced processing and excellent mechanical properties such as toughness and stiffness.

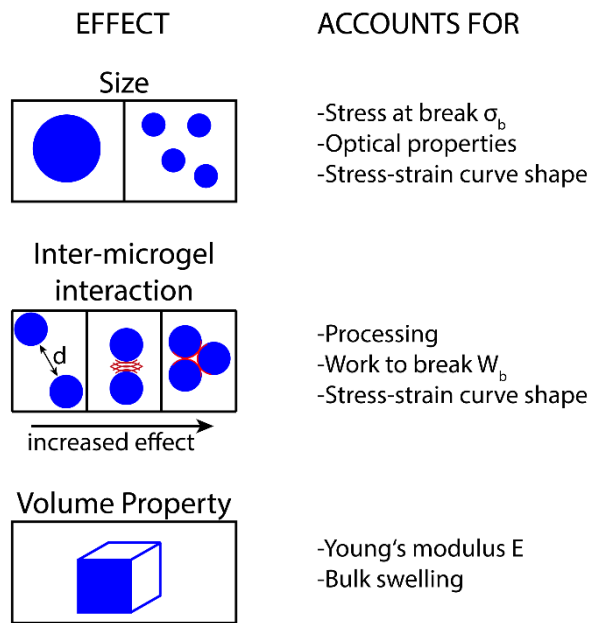


Figure 3.13. Schematic illustration of the influence of size, inter-microgel interactions and volume properties on the processing and mechanical properties of MRHs. Reproduced from [163] under the Creative Common License.

Chapter 4

The Influence of Swelling on the Stiffness and the Fracture Energy of Microgel-Reinforced Hydrogels

In this chapter, I investigate how the degree of swelling of bulk MRHs influences their stiffness and fracture energy. I show that the stiffness of MRHs in their fully swollen state depends on the connectivity of the reinforcing microgels, which is determined by their initial volume fraction prior to swelling of the bulk sample. At high microgel volume fractions we even observe a stiffening of the samples upon swelling that goes beyond linearity. In contrast, the fracture energy of MRHs that have been swollen to different extents linearly increases with the effective microgel volume fraction.

The chapter is adapted from a manuscript that is in preparation for submission.

Michael Kessler and Esther Amstad designed the study with inputs from John Kolinski. Michael Kessler and Tianyu Yuan performed the experiments, Michael Kessler and Esther Amstad analyzed the data and wrote the manuscript.

We thank Chenzhuo Li and the EMSI lab at EPFL for sharing the fluorescence microscopic setup equipped with a self-made tensile tester. We thank Robert Style and John Kolinski for fruitful discussions.

4.1 Abstract

The stiffness and toughness of conventional hydrogels decrease with increasing degree of swelling, making the stiffness-toughness compromise that is inherent to these hydrogels even more limiting, especially for load-bearing applications. The stiffness-toughness compromise of hydrogels can be addressed by reinforcing them with microgels, as we have shown in the previous chapter. However, the influence of the degree of swelling of microgel-reinforced hydrogels (MRHs) on their stiffness and toughness is unknown. To address this shortcoming, we compare the stiffness and toughness of MRHs reinforced with a wide range of microgel volume fractions as a function of their degree of swelling. We find that the initial microgel volume fraction determines the connectivity of the microgels, a nonlinear property that is closely related to the stiffness of fully swollen MRHs. If MRHs are reinforced with a high volume fraction of microgels, they even stiffen upon swelling, likely due to a strain-hardening effect in the matrix. In contrast to the stiffness, the fracture energy is much less dependent on the microgel connectivity and linearly increases with the effective volume fraction of microgels present in the MRHs regardless of their degree of swelling. These findings provide design rules for the fabrication of tough, granular hydrogels that stiffen upon their swelling.

4.2 Introduction

Gels are networks made from polymer chains that are connected through crosslinks. [9] They are omnipresent in a solvent-free, dry state, for example as elastomers, [167] and in a swollen state, such as hydrogels that contain a large fraction of water. [1] Unfortunately, the swelling of conventional gel networks significantly reduces their mechanical properties. While the reduction in strain at break [2] and modulus [168], [169] of a conventional hydrogel upon swelling scales with its linear swelling ratio, [170] its fracture energy is reduced by the areal swelling ratio. [2], [171] The decrease in fracture energy upon swelling matches with the observation by Lake and Thomas that the fracture energy of rubbers depends on the areal density of polymer chains that transverse the fracture plane. [7] Hydrogels are very often used under physiological conditions where they are swollen such that their stiffness and toughness are reduced. [108], [110], [153] This limitation restricts the fields of applications of these hydrogels to fields where soft, highly swelling components are required, such as for contact lenses or diapers. Hydrogels that counteract their swelling through thermo-sensitive monomers such that they do not swell within a certain temperature range have been reported for injection applications. [17] However, in this example the counter-action to the swelling is temperature-dependent.

An established design strategy to improve the resistance to fracture of swollen gels is to introduce dissipative mechanisms into them. [61] A prominent example for tough hydrogels are double network gels (DNs), that consist of a first, highly crosslinked and brittle network, and a second, loosely crosslinked and stretchy one. [34] During fracture of DNs, the first, sacrificial network dissipates a significant amount of energy via breakage of covalent [34],

[35], [39] or ionic [36] bonds, while the second network maintains the mechanical integrity of the material. The design principle is universal, and has been transferred to solvent-free multi-network elastomers. [42], [172] The toughening of DNs arises from breakage of bonds in the first network, as has been demonstrated with mechanophores that were covalently incorporated into multi-network elastomers and through a mechano-radical polymerization in hydrogels. [43], [46], [173] These results indicate that the breakage of bonds within the first, sacrificial network is confined to a damage zone that surrounds advancing cracks. The size of this damage zone linearly scales with the fracture energy of DNs. [41], [53], [54] However, traditional DNs are limited in terms of processing, as their first network must be swollen in the precursor solution of the second network, thereby sacrificing the control over their shape. [34], [35] To overcome this limitation, and to couple excellent toughness and stiffness with advanced processability, microgels have been embedded into single network hydrogels to form microgel-reinforced hydrogels (MRHs) that feature the double network toughening effect. Microgels are hydrogel microparticles of any shape with sizes between 0.1 and 1000 μm . [107], [108] They are swollen in the precursor solution of the second network, herein called matrix, before they are brought into shape via molding, [129] or, at high microgel volume fractions, 3D printing. [174] The matrix is subsequently polymerized to form tough microgel-reinforced hydrogels (MRHs). It has been shown that the microgel volume fraction and the molar ratio of the two networks within the microgels are the most important parameters that influence the toughness of MRHs. [131] In the previous chapter, I have shown that the strength of MRHs in their as-prepared state, which is prior to their swelling to equilibrium, can be increased by increasing the size of the reinforcing microgels. In contrast, their bulk swelling is independent of the microgel size. Unfortunately, little is known on how the bulk swelling of DNs and MRHs influences their mechanical properties. The yield point of DNs, which indicates the onset of major damage in the first network, arises at a yield stress that scales with the areal swelling ratio of DNs whereas the yield strain scales with their linear swelling ratio. [175] However, how the stiffness and fracture energy of tough hydrogels depend on their swelling ratio remains to be determined.

In this chapter, we study the effect of the bulk swelling of DNs and MRHs on their stiffness and fracture energy. We demonstrate that the initial microgel volume fraction in MRHs prior to swelling governs the connectivity of the microgels: if the microgels are up-concentrated and touch each other during the polymerization of the matrix, they become connected. We show that the stiffness of swollen MRHs exceeds the one of as-prepared samples if the microgels are firmly interconnected such that they themselves form a percolating network. We assign this behavior to a strain-stiffening in the matrix caused by its constriction between fully swollen, firmly interconnected microgels. In contrast, the fracture energy of MRHs is much less dependent on the connectivity between microgels, and is independent of their size. We show that the fracture energy linearly scales with the effective microgel volume fraction in MRHs before and after their swelling. These findings relate the fracture energy of MRHs to their microstructure and provide design rules for tough granular hydrogels that stiffen upon swelling.

4.3 Experimental Section

4.3.1 Microgel Production

We produce bulk hydrogels from an aqueous solution containing 20 wt% 2-Acrylamido-2-methyl-1-propanesulfonic acid sodium salt (NaAMPS) (Sigma-Aldrich, USA) monomer, 3 wt% of N,N-methylene bisacrylamide (MBAA) (Carl Roth, Germany), a crosslinker, and 1 $\mu\text{l/ml}$ of 2-hydroxy-2-methylpropiophenone (Sigma-Aldrich, USA), a photo-initiator. The solution is poured into a petri dish and polymerized for 10 minutes in a UV oven ($\lambda = 365 \text{ nm}$, $P = 2 \text{ mW cm}^{-2}$) (UVP CL-1000, Analytik Jena, Germany). The bulk hydrogel is cut into small pieces using scissors and inserted into a stainless steel cylinder of a cryogenic grinder (CryoMill, Retsch) alongside stainless steel milling balls. Cryo-milling is performed using three cycles of 3 minutes each at 30 Hz. To fabricate large microgels, we use a milling ball with a diameter of 25 mm. For the production of small microgels, we take large microgels and grind them further down by employing 12 balls with a diameter of 10 mm for additional three cycles. The obtained powder is fully swollen in water and subsequently freeze-dried (FreeZone 2.5, Labconco, USA) at 0.03 mbar and -53°C for at least three days to fully dry the microgels. The microgels are thereafter stored protected from humidity until their use.

4.3.2 Swelling Ratio of Microgels

The linear swelling ratio, $\lambda^{1/3}$, of non-spherical microgels is determined by measuring the swelling ratio of a bulk NaAMPS hydrogel, which is defined as $\lambda^{1/3} = \frac{X_{swollen}}{X_{as-prep}}$. Here, $X_{swollen}$ and $X_{as-prep}$ are defined as one side length of a rectangular bulk hydrogel in the fully swollen and as-prepared state prior to swelling, respectively. At least three bulk samples are measured for each data point.

4.3.3 Fabrication of MRHs

MRHs are fabricated as presented in chapter 3.3.5. To produce samples for single extension tests, molds with dimensions of $50 \times 10 \times 1 \text{ mm}^3$ are used. To perform tensile tests, dogbone-shaped samples with a thickness and width of 2 mm and 5 mm, respectively, and a gauge length of 10 mm are produced in Teflon molds. The samples are, as indicated in the main text, tested as-prepared or fully swollen in water. Samples that are tested in their as-prepared state are wrapped into cling film to avoid drying before they get tested, while samples that are tested in their fully swollen state are immersed in water for three days to fully swell them prior to testing.

4.3.4 Fabrication of Double Network Hydrogels

To produce bicontinuous double network hydrogels, a NaAMPS solution containing MBAA and a photoinitiator is polymerized in teflon molds, as detailed in chapter 4.3.1. The bulk PAMPS hydrogels are gently removed from the mold and swollen to equilibrium overnight in a AAm solution containing MBAA and photoinitiator, as detailed in chapter 3.3.5. The surplus AAm solution is removed before the samples are polymerized using UV light for 10 minutes. The samples are, as described in chapter 4.3.3, tested as-prepared or fully swollen in water.

4.3.5 Simple Extension Tests (SET)

SET are performed using a Universal Tensile Test Machine Zwicky 5 kN (Zwick Roell, Germany) equipped with a 50 N load cell. The two arms of the samples are gripped using hydraulic clamps and the velocity of the mobile arm is fixed to 100 mm/min, unless stated otherwise. The reported fracture energy is calculated as

$$T = 2 \left(\frac{F\lambda}{t} - W(\lambda)h \right). [44] \quad (4.1)$$

Here, F is the average of all force values on the plateau of the SET curve, λ the stretch of the legs at the plateau level of F , t the thickness of the sample, $W(\lambda)$ the area under the stress-stretch curve between 1 and λ , and h the width of a leg, as illustrated in [44]. This formula corrects for the stretch in the legs during the propagation of the crack when those undergo non-negligible stretch, which is with $1.4 \leq \lambda \leq 2.2$ the case for our samples. As the sample-to-sample variation of h and $W(\lambda)$ within one datapoint are small compared to the variations within the first term of equation (4.1), we estimate the second term of equation (4.1) per datapoint, and plot the error from the first term as error bars only. At least three samples are measured per datapoint.

The stretch of the legs can be avoided by fixing inextensible strips to the legs of the samples, which was not possible for most of our samples due to their surface rugosity. However, if the stretch of the legs is prevented by inextensible strips, or if it is negligible, which means $\lambda = 1$, and $W(\lambda) = 0$, equation (4.1) reduces to

$$T = \frac{2F}{t}, [44] \quad (4.2)$$

which is sometimes used in the literature. [53], [176] To estimate the influence of the leg stretch on our results, we compare our results evaluated with equations (4.1) and (4.2) for our system, and plot this comparison in the Supporting Figure 4.9. While the differences between the results for fully swollen samples obtained with equation (4.1) and (4.2) lie, to large extends, within the experimental error, there is a significant difference for the as-prepared samples if equation (4.1) or (4.2) is used. The use of equation (4.1) is in this case hence required.

4.3.6 Analysis of SET curves

To evaluate the amplitude of the deflections from the plateau value, we use a customized MATLAB® code. The amplitudes of the deflections are first normalized by the plateau value. The curves are then smoothed with an integrated smoothing function to remove the noise of the tensile tester, which is in the order of 0.001 kJ m^{-2} . Hence, the amplitude of the smallest deflections that can be measured relative to the plateau value is around 0.7%.

4.3.7 Tensile Testing

Tensile tests are performed on the same tensile tester with a velocity of 100 mm/min. Young's moduli are calculated from a linear fit to the stress-strain curves between 5 and 15% strain. At least three samples are measured per experiment, and at least two experiments are conducted per datapoint.

4.3.8 Bulk Swelling Measurements

The swelling ratio R_{sw} is defined as

$$R_{sw} = \frac{W_{sw}}{W_{ap}}; \quad (4.3)$$

here W_{sw} and W_{ap} are the hydrogel weight in its fully swollen and as-prepared state, respectively.

The polymer contents in the as-prepared state c_{ap} and in the swollen state c_{sw} are defined as

$$c_{ap} = \frac{W_{ap}}{W_{dry}}, \quad (4.4)$$

$$c_{sw} = \frac{W_{sw}}{W_{dry}}, \quad (4.5)$$

respectively. W_{dry} is the hydrogel weight in its fully dry state. The dry weight is measured after fully drying the hydrogels in an oven for three days. The hydrogels are weighted on a microbalance and at least three samples are measured for every datapoint.

4.4 Results and Discussion

4.4.1 Fabrication and Swelling of MRHs

To fabricate microgel-reinforced hydrogels we produce PAMPS microgels from a bulk hydrogel using a commercial cryo-miller, as reported elsewhere. [110] While this method leads to highly polydisperse and non-spherical microgels, it has a much higher throughput and a shorter processing time than emulsification techniques that require several washing steps. [108], [163], [174] We fully swell the obtained microgels in water and freeze-dry them to obtain a powder that is easily dispersible in the aqueous matrix precursor solution, which contains acrylamide (AAM) monomers, N,N-methylene bisacrylamide (MBAA), a crosslinker, and a photoinitiator. We precisely control the amount of dry microgels that we add to our samples by weighting them on a microbalance. The polymerization of the matrix is initiated by exposing these sample precursors to UV light, resulting in microgel reinforced hydrogels (MRHs). To retrieve the initial microgel volume fraction prior to swelling, ϕ_{init} , as a function of the weight of the dry microgels that is added to the samples, we use an extrapolation curve. The quantification of the swelling ratio of well-defined spherical microgels is more straight forward compared to that of the fragmented counterparts used here. However, we demonstrated that the swelling ratios of spherical microgels is within experimental error independent of their size, as shown in Figure 3.2. We observe the same swelling for the bulk hydrogels used to produce our non-spherical microgels, which is 2.3 ± 0.01 . We therefore use the same extrapolation curve here. Samples that are tested in their as-prepared state are wrapped into cling film to avoid drying prior to their testing. By contrast, samples that are tested in the fully swollen state are transferred into an aqueous solution and kept at room temperature for 3 days, as schematically shown in Figure 4.1. The degree of

swelling of these MRHs depends on their initial microgel volume fraction, ϕ_{init} . If the added microgels are initially in the dilute state, the effective microgel volume fraction present in the swollen samples, ϕ_{eff} , is lower than ϕ_{init} because the matrix swells more than the microgels, as depicted in Figure 4.1a. However, if the microgels are initially in the jammed state, they form a percolating network that limits the swelling of the matrix. In this case, the bulk swelling is equal to the swelling of the microgels and $\phi_{eff} \approx \phi_{init}$, as shown in Figure 4.1b.

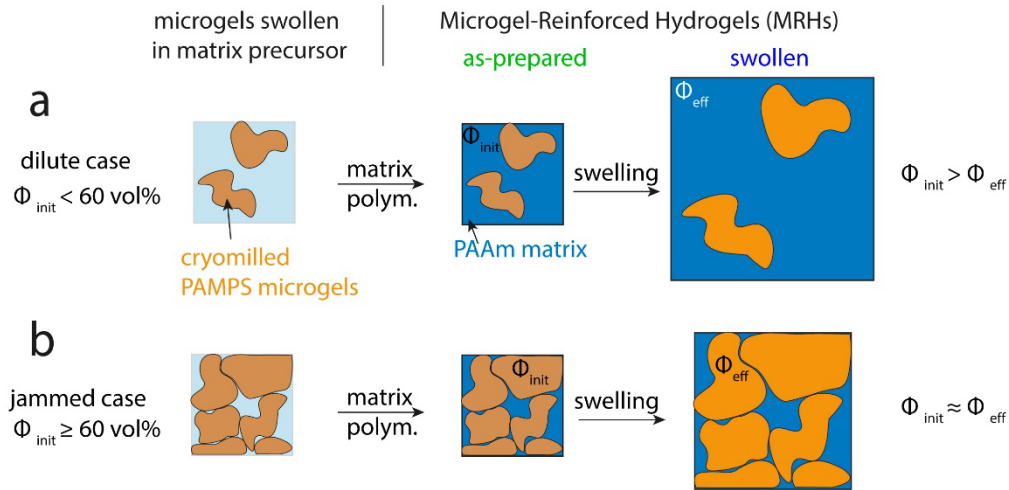


Figure 4.1: Schematic illustration of the swelling of microgel-reinforced hydrogels (MRHs) that depends on the initial microgel volume fraction ϕ_{init} . (a-b) The matrix precursor solution containing fully swollen microgels (left) is polymerized to form a bulk hydrogel (center), which is subsequently tested as-prepared, or fully swollen in water (right). (a) If the microgels are initially in the dilute regime, the swelling is dependent on the swelling of the matrix and that of the microgels, and the effective volume fraction in swollen samples, ϕ_{eff} , is reduced compared to ϕ_{init} . (b) If the microgels are touching each other during the polymerization of the matrix, they form a percolating network. In this case, the swelling is dependent on the swelling of the microgels only and $\phi_{eff} \approx \phi_{init}$.

4.4.2 The Influence of Swelling on the Mechanical Properties of MRHs

To assess the influence of the swelling of MRHs on their stiffness, we perform tensile tests on them in the as-prepared and swollen state and plot the results as a function of ϕ_{init} . The Young's modulus, E , of as-prepared MRHs linearly increases with ϕ_{init} , as shown in Figure 4.2a. By contrast, E of fully swollen samples increases much slower with ϕ_{init} if samples contain $\phi_{init} < 40$ vol% but increases much more steeply if $\phi_{init} > 40$ vol%, as shown in Figure 4.2a. Remarkably, MRHs with $\phi_{init} > 60$ vol% become stiffer upon swelling, as shown in Figure 4.2a. This behavior is in stark contrast to conventional bulk hydrogels that soften upon swelling.

By analogy to the stiffness, the fracture energy of conventional hydrogels decreases with their areal degree of swelling. [2], [171] To assess how the degree of swelling of MRHs influences their fracture energy, T , we use simple extension tests (SETs), as detailed in chapter 4.3.5. We mathematically account for the stretch in the sample legs, as the fixation of inextensible strips onto them was inhibited by their surface rugosity. For as-prepared samples, T linearly increases with ϕ_{init} . Note that T of the pure PAAm that does not contain any microgels, is slightly higher

than what we would expect from the linear trend of the $T(\phi_{init})$ curve. We assign the higher toughness of as-prepared microgel-free PAAM samples to the presence of entangled polymer chains that are not covalently linked to the network and hence, removed during the washing step. By contrast, swollen MRHs display a strong non-linear relation between T and ϕ_{init} , as shown in Figure 4.2b, by analogy to our observations for the stiffness - ϕ_{init} relationship. Note that the increase of the stress at break, σ_b and decrease of the strain at break, ϵ_b , with increasing ϕ_{init} is within experimental error the same for as-prepared and swollen MRHs, as shown in Figure 4.2c and 4.2d, respectively. This result implies that these parameters are mainly determined by the network architecture. By contrast, the swelling can be considered as pre-stretching of the polymer segments such that it does not change the mechanism of rupture of MRHs.

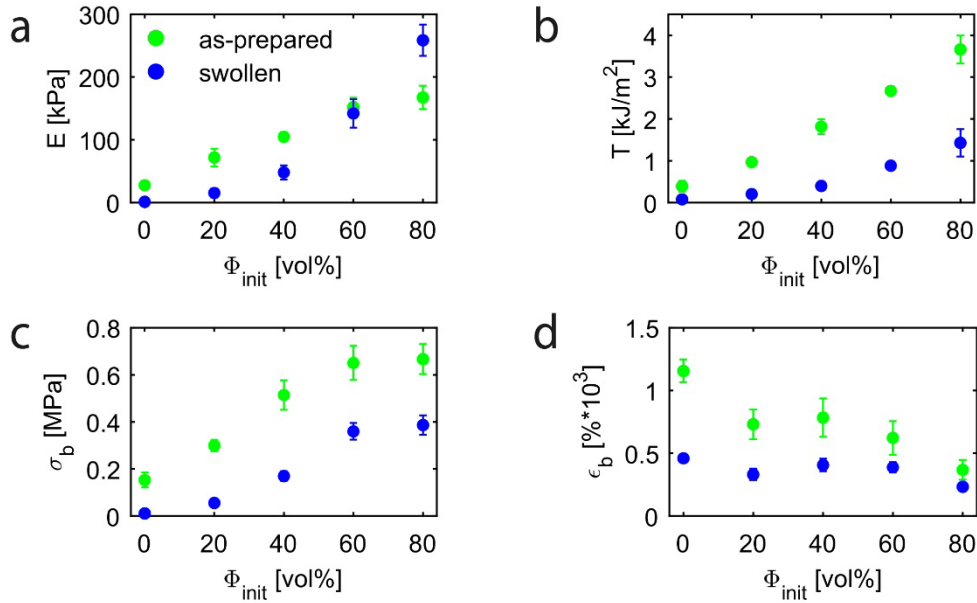


Figure 4.2: Mechanical properties of MRHs in their as-prepared (green) and fully swollen (blue) state. (a) Young's modulus E , (b) fracture energy T , (c) stress at break σ_b , and (d) strain at break ϵ_b as a function of the initial microgel volume fraction prior to swelling ϕ_{init} .

4.4.3 Swelling Ratio of MRHs

We hypothesize that the nonlinear trends observed for E and T in the swollen state are caused by a nonlinear reduction of the swelling of MRH samples with increasing ϕ_{init} . To verify our hypothesis, we perform swelling tests and measure the change in sample weight upon swelling from the as-prepared state to the swelling equilibrium. Pure PAAM gels swell 4.9-fold. The volumetric swelling ratio, λ , is reduced upon addition of microgels, as shown in Figure 4.3a. Interestingly, the swelling ratio of a MRH with $\phi_{init} = 80$ vol% is within experimental error the same as that of a bicontinuous bulk double network, even though the polymer fraction contained within the DN is significantly higher than that of the MRH, as shown in Figure 4.3b. To explain the plateau in λ at $\phi_{init} \geq 80$ vol%, we hypothesize that microgels are firmly covalently crosslinked to each other. The first and second networks of conventional DNs are covalently crosslinked together, as active sites are present in the first network when the second network is formed. [37] In our case, microgels serve as an analogue of the first network. Our results suggest

that we also have active sites in our microgels that, if microgels are densely packed, enable the formation of firm inter-microgel connections. These connections transform individual microgels into a percolating network that confines the matrix and hinders its swelling. The initial weight fraction of microgels, ϕ_{init} , has hence important consequences on their connectivity: If the microgels are jammed during the polymerization of the second network, they are firmly connected, whereas if they are individually dispersed, they are connected through the matrix hydrogel only.

The transition between the dilute and the jammed state is defined as the jamming transition, above which strong inter-microgel friction is present. [124] The jamming transition is accompanied by an increase in viscosity of the precursors. The volume fraction at which it occurs depends on the microgel size, [163] their shape [114] and polydispersity [114], [165], [177]. We observe a gradual increase in viscosity of the precursors at $\phi_{init} \geq 60$ vol%, which matches well with the observed plateau for λ , suggesting that our jamming transition occurs at approximately this microgel volume fraction.

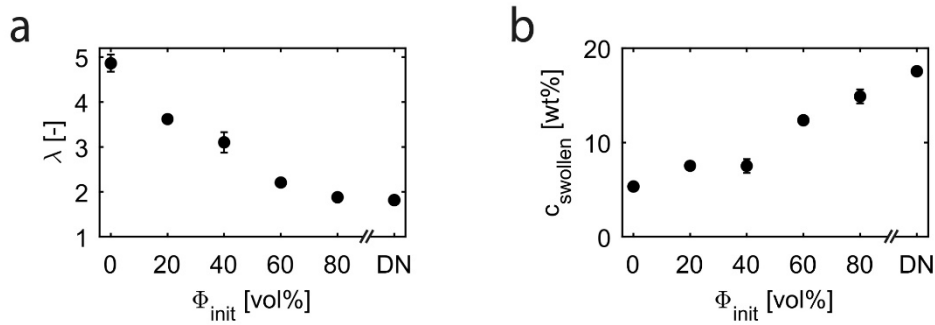


Figure 4.3: Swelling of microgel-reinforced hydrogels (MRHs). (a) Volumetric swelling ratio λ and (b) polymer content in the swollen state as a function of the initial microgel volume fraction prior to swelling ϕ_{init} .

4.4.4 Microgel Connectivity in MRHs: The Bridging Effect

Our swelling data indicate that bridging between microgels arises at $\phi_{init} \approx 80$ vol%. To verify if we indeed observe bridging between microgels, we consult an extreme, well-controllable case and use large, monodisperse microgels fabricated with a microfluidic device, as detailed in chapter 3.3.2 and shown in Figure 3.1. We use a high microgel volume fraction, $\phi_{init} = 80$ vol%, to form MRHs so that the microgels are strongly jammed, as shown in Figure 4.4a. After polymerization of the matrix, the hydrogel sheet is transferred into water where it is not confined so that it can freely swell. Despite the swelling, the microgels still show large contact areas with adjacent microgels, as shown in Figure 4.4b. These results indicate that microgels are indeed covalently crosslinked to each other. This dense packing of the microgels also confines the swelling of the matrix between them. We hypothesize that the confinement of the matrix is responsible for the increase in stiffness upon swelling that we observe for MRHs containing $\phi_{init} \geq 60$ vol%: in the vicinity of the inter-microgel bridges the matrix is strained, which likely leads to a strain stiffening. This observation is well in agreement with recent results reported for an elastomeric composite that encompasses dispersed microgels. [111]

We expect the observed reduction in swelling of bulk MRHs caused by the inter-microgel bridging to also manifest itself in ε_b , σ_b , and T . To test this expectation, we calculate the ratio of the as-prepared state to the swollen state for these parameters as a function of ϕ_{init} . Indeed, ε_b and σ_b display a plateau each, similar to the swelling, although at a lower microgel volume fraction, $\phi_{init} \geq 60$ vol%, as shown in Figure 4.4c. These results suggest that also ε_b and σ_b depend on the connectivity of the microgels. The initial microgel volume fraction is hence an important design parameter that affects how the strain and stress at break of MRHs are reduced upon swelling. In contrast, the ratio of the fracture energy of as-prepared to swollen samples does not show such a pronounced trend. We therefore expect another parameter to dominate the effect of swelling on the fracture energy of MRHs. A possible parameter that influences the fracture energy of MRHs is the effective volume fraction of microgels for each swelling state.

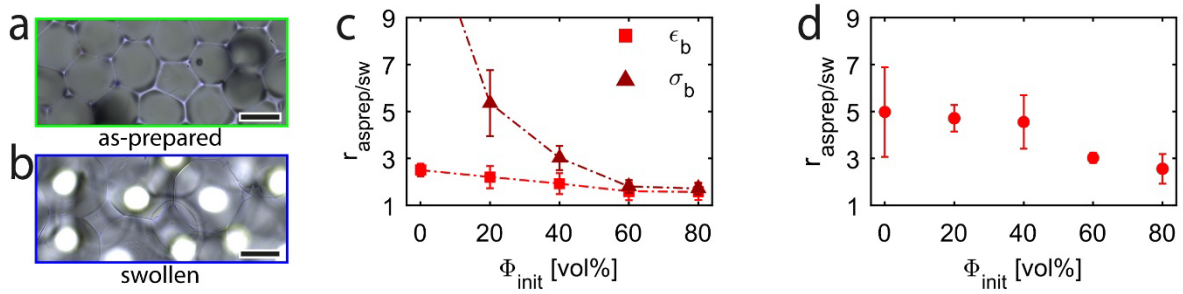


Figure 4.4: Bridging between densely packed microgels. (a-b) Micrographs of MRHs reinforced with large monodisperse microgels in the (a) as-prepared and (b) swollen state. Scale bars = 200 μm . (c) Ratio of the stress at break σ_b (dark red triangles) and strain at break ε_b (red squares) of as-prepared to swollen MRHs as a function of ϕ_{init} . The dashed lines are guides to the eye. (d) The ratio of the fracture energy T of as-prepared to swollen MRHs as a function of ϕ_{init} .

4.4.5 The Effective Microgel Volume Fraction in MRHs

The fracture energy of conventional gels scales with the areal density of polymer chains in the fracture plane. [171] Hence, upon their swelling, the fracture energy of single network hydrogels decreases by $\lambda^{2/3}$, which is the areal swelling ratio. [2], [9] However, in tough hydrogels, such as DN's, the fracture mechanism is more complex such that this scaling does not hold. In these materials, the fracture energy can be separated into an intrinsic and a dissipative part, [61], [178] as not only polymer chains in the fracture plane rupture, but also many sacrificial chains from the first network that are located in the damage zone of the advancing crack. [41], [54], [55]

The toughening mechanism of DNs strongly depends on the first network. Hence, for each swelling state, we expect the fracture energy of MRHs to be governed by the amount of microgels that are *effectively* present in them. To test this expectation, we must estimate the effective microgel volume fraction after swelling. Microgels swell to a similar extent as DNs, as shown in Fig 4.3. Hence, the volumetric swelling ratio λ of the microgels and the DN is the

same. We assign this result to the structure and composition of the first network of each of these systems, which are identical. Hence, we estimate the effective volume fraction, ϕ_{eff} , by using a simple rule of mixture for $20 \leq \phi_{init} \leq 60$ vol%, and by inserting the volumetric swelling ratios of the pure matrix and the microgels of 4.9 and 1.8, respectively. For these cases, ϕ decreases upon swelling, as summarized in Figure 4.1a. By contrast, for MRHs with $\phi_{init} = 80$ vol%, our swelling data indicates that their bulk swelling is equal to the swelling of the microgels, and hence $\phi_{init} \approx \phi_{eff}$, as summarized in Figure 4.1b. We hence correct the microgel volume fraction of swollen samples to ϕ_{eff} , and plot the stiffness and the fracture energy as a function of this parameter.

Re-scaling to ϕ_{eff} enables a comparison of E and T of the swollen and as-prepared samples for the same *effective* microgel volume fraction. The stiffness linearly increases with ϕ_{eff} if $\phi_{eff} < 30$ vol%, independent of the degree of swelling, as shown in Figure 4.5a. By contrast, the datapoint at $\phi_{eff} = 38$ vol% seems to be overcorrected. The jamming transition is gradual and the sample with $\phi_{eff} = 38$ vol% is in this transition regime. This result suggests that our system is sensitive to initial inter-microgel bridging that causes a strain stiffening of the matrix, which leads to a much stronger increase in stiffness than what we would expect from the linear stiffness- ϕ_{eff} correlation. This deviation from linearity is in contrast to the fracture energy, for which we observe a linear increase with increasing ϕ_{eff} over the entire evaluated range, independent of the degree of swelling, as shown in Figure 4.5b. This indicates that the effective microgel volume fraction is indeed a good metric to predict the fracture energy of microgel-reinforced granular hydrogels.

The slope of the linear fit to the $T(\phi_{eff})$ datapoints of the swollen samples decreases by a factor 2.3 with respect to its as-prepared counterpart. It was shown by Lake and Thomas that the fracture energy is dependent on the areal density of the polymer chains in the fracture plane. [7] This indicates that the reduction in T upon swelling for conventional gels is equal to their areal swelling ratio $\lambda^{2/3}$. [2] To test whether this relation also applies to MRHs, we compare the reduction of T upon swelling to $\lambda^{2/3}$ of their components. The reduction found here, 2.3, is between the areal swelling ratios $\lambda^{2/3}$ of the matrix and that of the microgels, which are 2.9 and 1.8, respectively. This result indicates that neither the reduction in areal polymer density of the matrix nor the microgels can fully explain the reduction in T upon swelling. This raises the question whether cracks propagate mostly within the matrix, or within the microgels. To address this question, we perform in-situ crack propagation under the microscope.

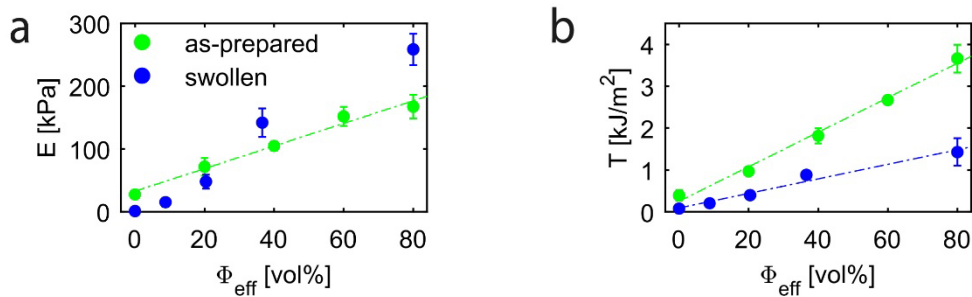


Figure 4.5: Influence of the effective microgel volume fraction ϕ_{eff} on the stiffness and fracture energy of microgel-reinforced hydrogels (MRHs). (a) Young's modulus E and (b) fracture energy T of MRHs in their as-prepared (green) and fully swollen (blue) state as a function of ϕ_{eff} . (a-b) The dashed lines are linear fits to the experimental data. (b) The slope of the linear fit to the swollen dataset is reduced by a factor 2.3 compared to the slope of the linear fit to the as-prepared dataset.

4.4.6 The Influence of Microgels on the Crack Propagation in MRHs

The fracture energy in soft and tough materials, such as DN hydrogels, can be separated into an intrinsic Γ_0 and a dissipative Γ_D component, as presented in equation 1.22, whereby $\Gamma_D \gg \Gamma_0$. [178] However, the intrinsic fracture energy is in theory still an important parameter, as the total fracture energy and its intrinsic component are proportional to each other, $\Gamma \propto \Gamma_0$, as I detailed in equation 1.23. [178] This correlation is directly linked to the crack propagation: if cracks easily propagate through the material, the load cannot be efficiently transferred to the first network to dissipate energy. We reason that if the crack is often deviated by obstacles present in the sample, such as microgels, it follows a tortuous path and the intrinsic component of the fracture energy is multiplied by the additionally created surface area arising from crack tortuosity. This should subsequently linearly augment Γ , following equation 1.23. To investigate how cracks propagate through MRHs, and if they are deviated by the microgels, we perform in-situ crack propagation experiments under the microscope. To distinguish our negatively charged microgels from the matrix, we use a positively charged fluorescent dye, cresyl violet, as detailed in chapter 3.3.6. We indeed observe that cracks are deviated and even split into two if they encounter a microgel, as shown in Figure 4.6ai-av and 4.6b. The split cracks get blunted thereafter, as shown in Figure 4.6av. The entire sample subsequently undergoes high strains prior to catastrophic failure, as illustrated in Figure 4.6av and 4.6ci. At these high strains, voids start to form within the material, which eventually coalesce with neighboring voids or the crack front, leading to catastrophic failure. These voids are very often initiated at the surfaces of microgels from where they open up, as shown in Figure 4.6cii-iv and 4.6d. We assign this behavior to the difference in stiffness between our microgels and the surrounding matrix, and the therewith associated stiffness gradient at the microgel surfaces.

To weaken the effect of stiffness gradients and to investigate whether this influences the mode MRHs catastrophically fail, we employ much smaller microgels with an equivalent diameter of $15 \pm 8 \mu\text{m}$. Indeed, in these MRHs that contain smaller microgels, opening voids grow much more prior to their coalescence, as shown in Figure 4.6e. Note that this difference is not related to the strain at break and the stiffness of the samples, as these parameters are independent of the microgel size, as shown in chapter 3. These results qualitatively suggest that the size of reinforcing microgels influences the crack propagation mechanism in MRHs.

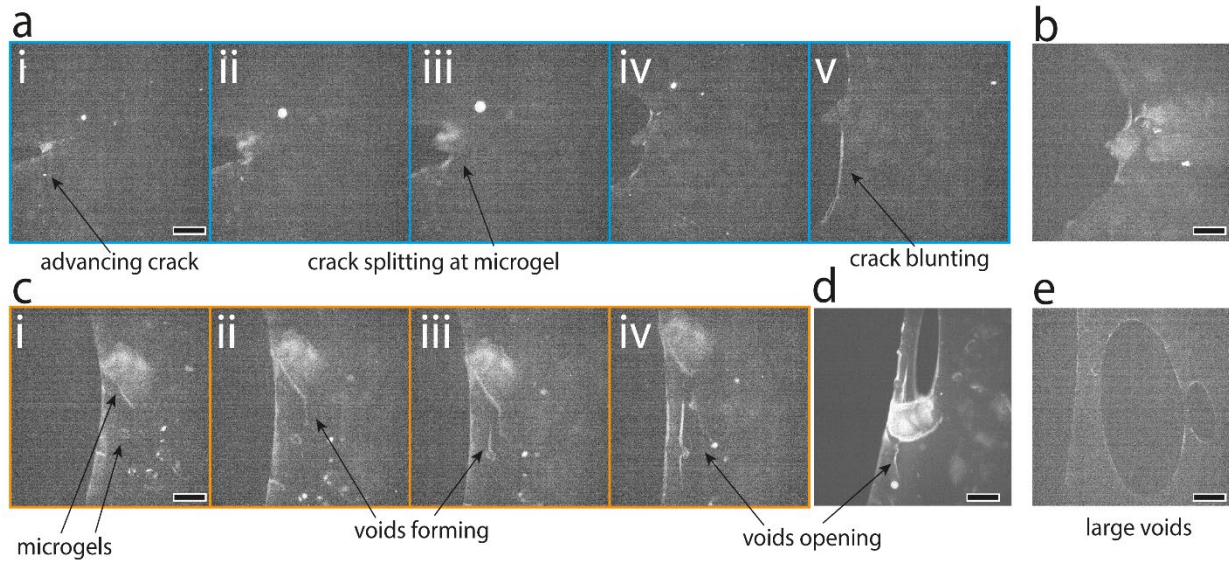


Figure 4.6: Micrographs of catastrophic failure events of microgel-reinforced hydrogels (MRHs). The microgels are visualized using a fluorescent dye and appear brighter than the matrix. (a-b) Crack splitting events. (ai-av) Time-lapse of a crack that (ai) is initiated and (aii-aiiv) splits when encountering a microgel. (av) The crack blunts. (b) Another example of a crack that splits at a microgel. (c-e) Formation of voids. (c) Time-lapse of a blunted crack (ci) meeting microgels from where (cii-ciii) voids open up, which are visible as white lines, before they (civ) grow. (d) Another example of voids forming and opening up at the edge of a large microgel. (e) A MRH sample that is reinforced with much smaller microgels where large voids start to form before they coalesce. Scale bars represent (a,e) 500 μm and (b,c,d) 200 μm .

To investigate if the microgel size influences the crack propagation and the resulting fracture energy of MRHs, we perform simple-extension tests (SET) on MRH samples reinforced with large or small microgels; the size distribution of the employed small and large microgels is shown in Figure 4.7a. Indeed, the crack propagation in MRHs containing $\phi_{init} = 40$ vol% microgels is much smoother if they are reinforced with small microgels compared to MRHs reinforced with large microgels, as summarized in Figure 4.7bi and detailed in Figure 4.8a and 4.8b. To more quantitatively analyse to what extent cracks are deflected while propagating through our samples, we analyse the amplitudes of the deflections of the SET curves from their plateau values. The deflections in MRHs reinforced with small microgels are on average smaller than those in MRHs reinforced with large microgels, as summarized in Figure 4.7c and 4.7d for large and small microgels, respectively. However, our batch of large microgels also contains small ones, as shown in Figure 4.7a. To determine whether the strong deflections observed for MRHs reinforced with large microgels are indeed caused by the size of the microgels, we reinforce hydrogels with large, monodisperse microgels. Indeed, SET curves of MRHs reinforced with large monodisperse microgels show a similar trend as the ones reinforced with large, non-spherical counterparts, as shown in Figure 4.8c and 4.8e. This confirms that the microgel size influences the crack propagation in MRHs at low ϕ_{init} . By contrast, we do not observe any influence of the microgel size on the crack propagation in MRHs reinforced with $\phi_{init} = 80$ vol%. At these high volume fractions, microgels are jammed such that propagating cracks do not conceive them as individual obstacles any more. Interestingly, cracks in bicontinuous double network hydrogels propagate very smoothly, as shown in Figure 4.7bii and Figure 4.8d. This comparison suggests that the crack propagation is dependent on the homogeneity of the first network. However, note that due to differences in the processing of these samples, DN samples are 1-2

fold thicker compared to the MRH counterparts. The thickness difference may be a contributing factor to the smoother curves. Moreover, our spatial resolution is limited by the tensile tester to $\sim 120 \mu\text{m}$ such that the smallest features that can be distinguished from the noise are $\sim 500 \mu\text{m}$. This dimension is much larger than the employed microgels. We hence describe the propagation of the cracks more macroscopically, yet, we can relate its propagation to the employed microstructure.

To assess whether the microgel size and hence the crack tortuosity influences the fracture energy, we compare the measured T of MRHs reinforced with small and large microgels for a wide range of ϕ_{init} . In a first approximation, the fracture energy is independent of the microgel size, as shown in Figure 4.7e. This finding excellently matches our previous results where we demonstrated that the fracture energy is independent of the connectivity of the first network. While cracks are more deflected by large microgels at $\phi_{init} = 40 \text{ vol}\%$, this crack deflection does not measurably influence the fracture energy of MRHs. This finding confirms that the effective microgel volume fraction is indeed determining the fracture energy of MRHs.

Note that we observe a dependence of T on the test velocity, as shown in Figure 4.8f. This has been reported before [53], [55] and is due to an increased size of the damage zone around the crack for higher velocities [48], [55], due to inertial effects in the material and a more efficient stress transfer between the two networks at higher testing velocities. However, while we vary the testing speed over two orders of magnitude the result only changes twofold.

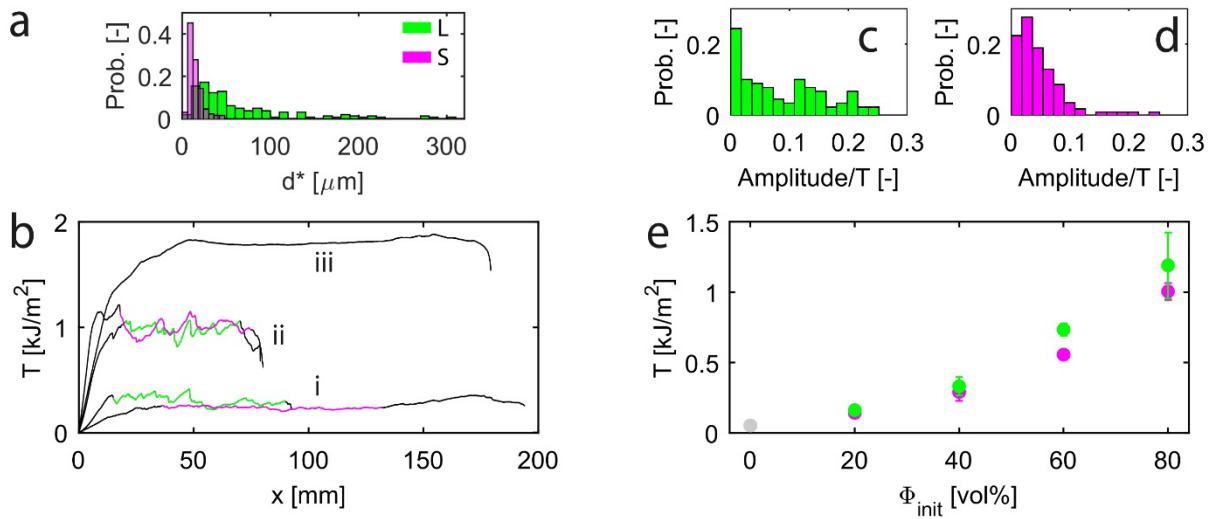


Figure 4.7: Influence of the microgel size on the crack propagation and fracture energy of MRHs. (a) Size distribution of large and small microgels. d^* corresponds to the diameter of a circle with the same area as the one measured for the non-spherical microgels employed here. (b) Representative force-displacement curves of simple extension tests (SET) for swollen (i-ii) MRH samples reinforced with (i) $\phi_{init} = 40 \text{ vol}\%$ or (ii) $\phi_{init} = 80 \text{ vol}\%$ small (green) or large (magenta) microgels, and for (iii) bulk double networks. (c-d) The amplitude distribution of the deflections in the force-displacement curves, normalized by their corresponding plateau value T with $\phi_{init} = 40 \text{ vol}\%$, for (c) large and (d) small microgels. (e) The fracture energy T of MRHs reinforced with large (green) and small (magenta) microgels as a function of ϕ_{init} . (b-e) Note that for simplicity the curves and amplitudes were not corrected for the stretch of the legs, as for swollen samples no major difference is found between the corrected and simplified datasets.

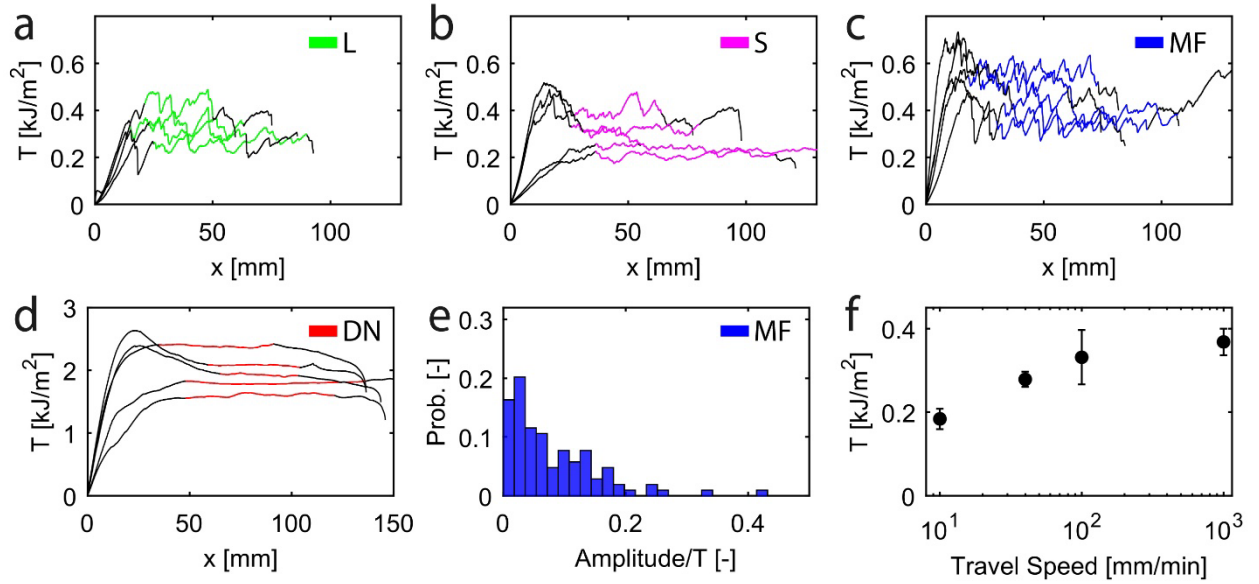


Figure 4.8: Simple Extension Tests (SET). (a-c) SET curves for MRH samples reinforced with (a) large, (b) small, and (c) large monodisperse microgels. (d) SET curves for double networks (DN). (e) The amplitude distribution of the deflections in the force-displacement curves, normalized by their corresponding plateau value T , with $\phi_{init} = 40$ vol% for large monodisperse microgels. (f) Fracture energy T of MRHs reinforced with $\phi_{init} = 40$ vol% large microgels as a function of the testing speed. (a-f) Note that for simplicity the plotted data was not corrected for the stretch of the legs, as for swollen samples no major difference is found between the corrected and simplified datasets.

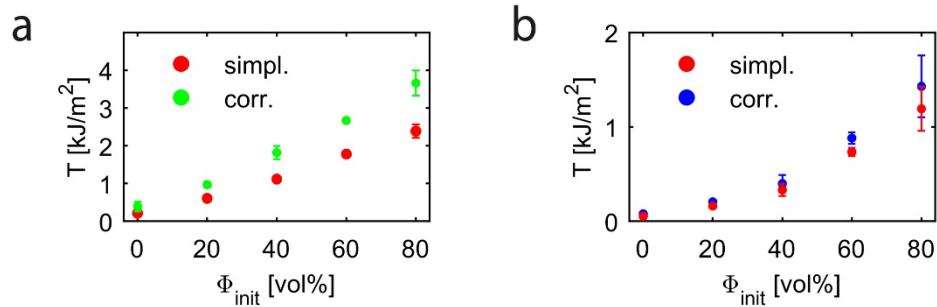


Figure 4.9: Evaluation of the fracture energy T of MRHs using SET tests. (a-b) Fracture energy T in their (a) as-prepared and (b) fully swollen state as a function of ϕ_{init} . For the datasets analysed using the simplified equation (4.2) (red) the stretch of the legs is neglected, while for the datasets analysed using equation (4.1) (green in (a), blue in (b)), it is corrected for it.

4.5 Conclusion

The mechanical properties of conventional hydrogels such as their stiffness and fracture energy decrease with increasing degree of swelling. Here, we demonstrate that hydrogels that are reinforced with high volume fractions of microgels swell much less than what would be expected from the rule of mixture. We assign this deviation from linearity to strong inter-microgel connections that form if the microgels touch during the polymerization of the matrix, thereby restricting the degree of swelling of the bulk MRHs. These firm inter-microgel links strongly increase

the stiffness of MRHs upon swelling, in stark contrast to conventional hydrogels. In contrast, the fracture energy decreases with increasing degree of swelling and is linearly related to the effective microgel volume fraction present in the material. These observations are directly applicable to design tough hydrogels that stiffen upon swelling.

Chapter 5

Everything in its Right Place: Controlling the Local Composition of Hydrogels Using Microfluidic Traps

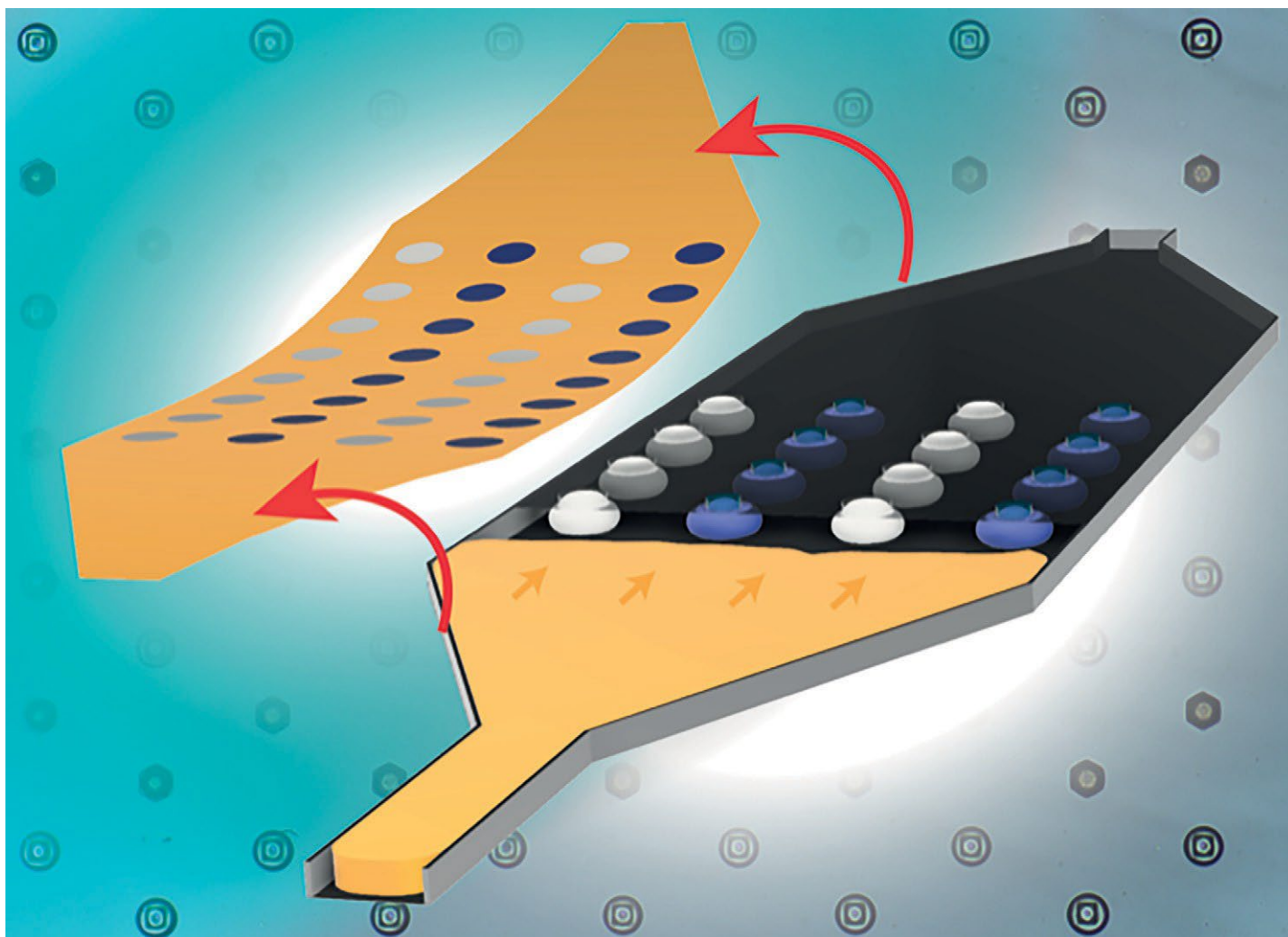
In this chapter I present a microfluidic device for the fabrication of hydrogel sheets with locally varying compositions. Capillary traps with different trapping strengths can controllably immobilize different types of water-in-oil drops at well-defined locations before they are converted into microgels. The oil is subsequently replaced by the aqueous matrix precursor solution, which is polymerized to form a continuous hydrogel sheet possessing locally varying compositions.

The chapter is adapted from the published paper “Kessler, M. *et al.* (2020) ‘Everything in its right place: controlling the local composition of hydrogels using microfluidic traps’, *Lab on a Chip*, 20(24), pp. 4572–4581.”, authored by Michael Kessler, Hervé Elettro, Isabelle Heimgartner, Soujanya Madasu, Kenneth Brakke, François Gallaire, and Esther Amstad.

Michael Kessler and Esther Amstad designed the study with inputs from François Gallaire. Michael Kessler, Isabelle Heimgartner, and Soujanya Madasu performed the experiments, Michael Kessler and Hervé Elettro did the modelling, Michael Kessler and Soujanya Madasu performed simulations with the help of Kenneth Brakke. Michael Kessler and Esther Amstad analyzed the data and wrote the manuscript.

We would like to thank Nicolas Burnand for experimental help.

The paper was featured in the themed collection “Lab on a Chip Recent HOT Articles” due to receiving particularly high scores at peer review.



Showcasing research from the Soft Materials Laboratory SMaL of Professor Esther Amstad, Institute of Materials, EPFL, Switzerland.

Everything in its right place: controlling the local composition of hydrogels using microfluidic traps

We introduce a microfluidic Hele-Shaw trapping cell that enables the fabrication of hydrogel sheets with locally varying compositions. With the presented microfluidic device, we can abruptly change the composition of materials on a $100\ \mu\text{m}$ length scale. The abrupt compositional changes are achieved by selectively immobilizing different types of drops at well-defined locations using traps possessing varying trapping strengths. The drops are subsequently converted into microparticles before the matrix material is injected into the microfluidic chamber and solidified to form an integral hydrogel sheet.

As featured in:



See Esther Amstad *et al.*,
Lab Chip, 2020, 20, 4572.

5.1 Abstract

Many natural materials display locally varying compositions that impart unique mechanical properties to them which are still unmatched by manmade counterparts. Synthetic materials often possess structures that are well-defined on the molecular level, but poorly defined on the microscale. A fundamental difference that leads to this dissimilarity between natural and synthetic materials is their processing. Many natural materials are assembled from compartmentalized reagents that are released in well-defined and spatially confined regions, resulting in locally varying compositions. By contrast, synthetic materials are typically processed in bulk. Inspired by nature, we introduce a drop-based technique that enables the design of soft hydrogel sheets with locally varying compositions and offers an excellent spatial resolution. This is achieved with a microfluidic Hele-Shaw cell that possesses traps with varying trapping strengths to selectively immobilize different types of drops. This modular platform is not limited to the fabrication of hydrogels but can be employed for any material that can be processed into drops and solidified within them. It likely opens up new possibilities for the long-term characterization of reactions that occur under confinement within drops and the design of structured, load-bearing hydrogels, as well as for the next generation of soft actuators and sensors.

5.2 Introduction

Many natural materials display unique mechanical properties that are, at least in parts, a result of their locally varying composition. A prominent example is the mussel byssus cuticle, a stiff, but extensible coating that is five-fold harder than the fibrous core and hence protects it from abrasion. [98] The cuticle is composed of granules that are embedded in a matrix. These granules are responsible for the abrupt changes in the composition and hence, the excellent mechanical properties of the cuticle. [100], [101], [179] The ability of nature to controllably and abruptly change the composition of materials is related to their processing: Natural materials are often produced from compartmentalized reagents that can be released into well-defined and spatially confined regions. [99] To mimic such assembly as observed in nature, a large variety of bottom-up processes have been developed to fabricate synthetic soft materials with locally varying compositions. Well-defined micrometer-sized structures with feature sizes down to 10 μm can be introduced into soft materials using direct laser writing [180] or lithography techniques that take advantage of digital micro-mirror devices (DMD's). [90] However, these techniques are often limited to sample sizes below 100 μm . Macroscopic materials possessing feature sizes down to 200 μm can be produced with optical projection lithography, using a laser and DMD. [181] Similarly, direct ink writing allows the fabrication of macroscopic samples that optionally can be composed of multiple materials with a resolution of 100-200 μm . [182] Resolutions of 200 μm [183], 100 μm [127] or even 35 μm [184] can be obtained if supporting matrices consisting of granular microgels or shear-thinning self-healing hydrogels are employed. However, the composition of materials made with these methods cannot be abruptly changed. Abrupt changes in the composition have been reported for 3D-printed continuous filaments, yet with a reduced resolution. [185] Methods

to fabricate composites made of multiple different materials that possess well-defined microstructures and whose composition can be abruptly and controllably changed remain to be established.

A possibility to gain true control over the local composition of soft materials is the immobilization and solidification of reagent-loaded drops in obstacle-free microfluidic devices. Drops can be immobilized in obstacle-free Hele-Shaw cells for example using acoustic waves [186] or electrostatic potentials. [187], [188] However, such active methods rely on complicated microfabrication methods and require external energy sources, such that up-scaling becomes tedious. An elegant, passive method to immobilize drops in an obstacle-free Hele-Shaw cell is the use of microfluidic traps. This method relies on the minimization of the surface energy of drops: When drops with a diameter larger than the channel height are squeezed into the cell, they deform into pancakes, thereby increasing their surface area and hence total energy, $E = \gamma A$; here γ is the interfacial tension and A the surface area. Squeezed drops can relax if they encounter a trap; a restricted area where the channel height is locally increased. In this case, the surface energy of drops decreases. The gradient in surface energy between the squeezed and partially relaxed state of drops leads to a trapping force that opposes the drag force and hence, enables immobilization of drops. Studies conducted in Hele-Shaw cells demonstrated that larger traps produce larger trapping forces while larger drops experience larger drag forces. [189] Devices that immobilize drops in microfluidic traps have been employed to monitor the evolution of cells, [190], [191] chemical reactions, [190] or to investigate cross-talk between emulsion drops. [192], [193] However, this strategy has never been employed to design macroscopic materials with well-defined locally varying compositions.

In this chapter, we introduce a microfluidic trapping device that enables the design of hydrogel sheets with locally varying compositions. To achieve this goal, we study the influence of the geometry of traps on their trapping strengths. We demonstrate that the trapping strength depends on the depth, area, and in-plane geometry of the trap. Based on these experimental results we introduce a mathematical model and perform simulations to predict the trapping strength. These tools facilitate the design of Hele-Shaw cells containing traps with different trapping strengths that enable the immobilization of different types of drops at well-defined locations. To demonstrate the potential of this device, we fabricate different examples of hydrogel sheets with locally varying compositions and controlled microstructures.

5.3 Experimental Section

5.3.1 Fabrication of the Microfluidic Devices

Microfluidic devices are produced from poly(dimethyl siloxane) (PDMS, Sylgard 184, Dow Corning, USA) using soft photolithography. [194] The PDMS mold is bonded to a glass slide using oxygen plasma (Plasma Harrick, UK) to close the chamber. To render the surfaces fluorophilic, we inject a HFE7500-based solution (Novec, 3M, USA) containing 2% (v/v) trichloro- (1H,1H,2H,2H-perfluorooctyl)silane (Sigma-Aldrich, USA). The solution is kept in the channels for 15 minutes before the channels are dried with compressed nitrogen. To render the surfaces hydrophilic

we inject a polyelectrolyte solution containing 2% (w/w) PDADMAC poly(Diallyldimethylammoniumchloride) (Sigma-Aldrich, USA) in a 2M sodium chloride solution. The solution is kept inside the channels for 1 hour before the solution is removed with compressed nitrogen. The channel height h is kept constant at $55 \pm 3 \mu\text{m}$ for all the experiments. Its variation was measured using a VK-X360K 3D Laser Scanning Confocal Microscope (Keyence, Belgium). To study the influence of the trap dimensions on the trapping strength, we employ a 1.5 mm wide and 5.1 mm long microfluidic channel. The center-to-center distance between the traps is $800 \mu\text{m}$. Our polygonal traps have an area of $7854 \mu\text{m}^2$, equivalent to the area of circular traps with diameter $W = 100 \mu\text{m}$. To fabricate hydrogel sheets, we use a 4 mm wide and 19.3 mm long Hele-Shaw cell that contains 570 traps. Hexagonal traps with an area of $7854 \mu\text{m}^2$ and square traps with an area of $3849 \mu\text{m}^2$ are used for strong and weak traps, respectively. These areas are equivalent to the areas of circular traps with diameters $W = 100 \mu\text{m}$ and $70 \mu\text{m}$, respectively. For the second and third applications we employ hexagonal traps with an area of $7854 \mu\text{m}^2$ to ensure strong trapping.

5.3.2 Formation of Water-In-Oil Emulsion Drops

Water-in-oil drops are produced using a microfluidic flow focusing device whose main channel is $100 \mu\text{m}$ wide and $55 \mu\text{m}$ tall. [195] We employ an aqueous solution containing 15% (w/w) poly(ethylene glycol) (PEG, $M_W = 6 \text{ kDa}$) as a dispersed phase and HFE7500 as a continuous phase. To ensure that drops do not break during any of the liquid exchange steps, we add 1% (w/w) of a fluorinated triblock surfactant (DiFSHJeffamine900) to the oil phase. [196] The interfacial tension between the water and the oil phase is 5 mN/m , as measured with the pendant drop method (Krüss, DSA30, Germany). The two phases are injected into the device at $100 \mu\text{l/h}$ and $500 \mu\text{l/h}$ for the water and oil phase, respectively, using two volume-controlled syringe pumps (Cronus Sigma 1000, Labhut, UK).

5.3.3 Measuring Critical Flow Rates of Traps

For every data point, experiments are performed on at least 2 different microfluidic chips to exclude that observed differences in trapping strength are related to surface treatments. In every device, at least 6 drops are measured per geometry, resulting in at least 12 data points from which we calculate the average and standard deviation.

5.3.4 Fabrication of Structured Hydrogel Sheets

Hydrogel sheets with locally varying compositions are fabricated using aqueous solutions containing 50% (w/w) PEGDA (PEG700-DA, $M_W \approx 700 \text{ Da}$, Sigma-Aldrich, USA) and 2% (w/w) 2-hydroxy-2-methylpropiophenone (97%, Sigma-Aldrich, USA), a photoinitiator. 33% (v/v) of fluorescent, red food colorant (Migros, CH), or 0.8 mg/ml fluorescein disodium salt (Carl Roth, Germany) are added to label different batches of drops. Drops are trapped before reagents contained in them are polymerized by exposing the device to UV light ($320 \text{ nm} < \lambda < 500 \text{ nm}$) (Omnicure S 1000, Lumen Dynamics, Canada). We keep the distance between the optical fiber, which has a diameter of 8 mm , and the microfluidic device constant at 5 cm and expose the sample to UV light for 3 minutes to ensure complete curing of the hydrogel. The matrix, composed of the same polymer and photoinitiator, is inserted using a syringe pump and crosslinked with UV light as described above. The device is opened using a surgical blade

and the resulting hydrogel sheet is removed from the device. Hydrogel sheets are observed under a fluorescent microscope (Eclipse Ti-S, Nikon, Japan).

For the sheets with selective absorption, we use an aqueous solution containing 20% (w/w) AMPS (2-Acrylamido-2-methylpropane sulfonic acid, Sigma-Aldrich, USA) as a monomer, 3% (w/w) N,N'-Methylenebisacrylamide (Sigma-Aldrich, USA) as a crosslinker, and 11 $\mu\text{l/ml}$ 2-hydroxy-2-methylpropiophenone (Sigma-Aldrich, USA) as a photoinitiator. The sheets were stained using an aqueous solution containing 0.8 mg/ml cresyl violet perchlorate (Sigma-Aldrich, USA).

For the fabrication of porous hydrogel sheets, we render all surfaces hydrophilic. We employ the fluorinated oil phase described above as the dispersed phase and an aqueous phase containing 50% (w/w) PEGDA700, 2% (w/w) 2-hydroxy-2-methylpropiophenone, and 1% (w/w) Pluronic F127 Krill, a surfactant, as the continuous phase. The surface profile of the pore was recorded using a VK-X360K 3D Laser Scanning Confocal Microscope (Keyence, Belgium).

5.3.5 Surface Evolver Simulations

Equilibrium states of drops in traps in steady state are evaluated using the Surface Evolver software. [197] Surface Evolver is an efficient numerical solver that relaxes the shape of fluid interfaces in space-dependent energy landscapes under different constraints, such as conservation of volume or presence of solid boundaries. The contact angle was put to 179° for non-wetting conditions and gravity was neglected. Drops have a volume of 0.9 nL except if stated otherwise. The channel height is kept constant at 55 μm for all simulations. The evolution of the simulations is monitored using a built-in surface energy evolution diagram.

5.4 Results

The fabrication of materials whose composition can be locally tuned with a tight control over the type and location of the different components requires means to selectively immobilize drops. To achieve this goal, we design traps with different trapping strengths. Different types of traps with varying trapping strengths can then be arranged on the same Hele-Shaw cell to selectively immobilize different types of drops, as schematically shown in Figure 5.1a. We take the minimum flow rate where immobilized drops are released from their trap, the critical flow rate Q_C , as a measure of the trapping strength. To quantify Q_C , we design a 5.1 mm long, 1.5 mm wide, and 55 μm high microfluidic chamber that contains four traps in a row, as schematically shown in Figure 5.1b. Water-in-oil drops with an average volume of 0.9 ± 0.04 nL are produced in a flow focusing junction that is located upstream the main chamber. We produce drops with a diameter much larger than the channel height h . These drops remain squeezed and attain a pancake-shape when entering the main chamber. When they encounter a trap, they relax into it to minimize their surface energy, as schematically shown in the steady-state Surface Evolver simulation [197] in Figure 5.1c. As a result of the decreased surface energy, the drops remain trapped. When all four traps are occupied with drops, we stop their production and set the flow of the continuous phase to zero, as shown in the optical micrograph

in Figure 5.1di. When we increase the flow rate of the surrounding oil but keep $Q < Q_c$, drops deform in the direction of the flow but find an equilibrium position such that they remain trapped, as shown in Figure 5.1dii. When $Q > Q_c$, drops are removed from their trap, as shown in Figure 5.1diii.

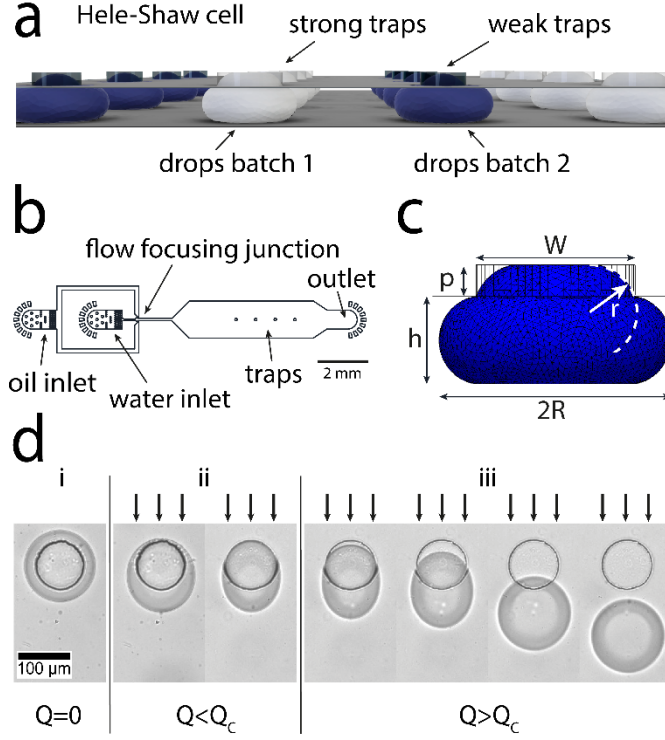


Figure 5.1: Microfluidic traps with different trapping forces. (a) Schematic illustration of proposed device that contains two types of traps with different trapping strengths to selectively immobilize drops from different batches. (b) Sketch of a microfluidic device used to measure the critical flow rate of traps, composed of a flow focusing junction that is connected to a main chamber containing 4 identical traps. (c) Side view of a trap occupied by a drop that is simulated with Surface Evolver. The relevant dimensions are defined as channel height h , trap depth p , trap width W , radius of the drop in the channel R , and radius of curvature of the drop r . (d) Time-lapse optical microscopy images of a trapped drop (i) under static conditions and when the surrounding oil flows at a rate (ii) below and (iii) above Q_c . Reproduced from [198] with permission.

5.4.1 Influence of Trap Width

To design traps with varying trapping strengths, we investigate the influence of the dimensions of traps on their trapping strength. We employ circular traps, which have been shown to efficiently trap drops, [189], [199] and vary their width W . The critical flow rate increases with increasing trap diameter for traps with $W \leq 100 \mu\text{m}$ and reaches a plateau thereafter, as summarized in Figure 5.2a. To investigate the origin of the independence of the critical flow rate with respect to the trap diameter for large trap diameters, we image the drops in the traps. Only a fraction of the projected drop area occupies the trap if $W \leq 100 \mu\text{m}$. This is in stark contrast to traps with diameters exceeding $100 \mu\text{m}$ where the entire projected drop area is contained within the trap such that the trapping force, F_y , remains within experimental error constant, as shown in Figure 5.2a and 5.2b.

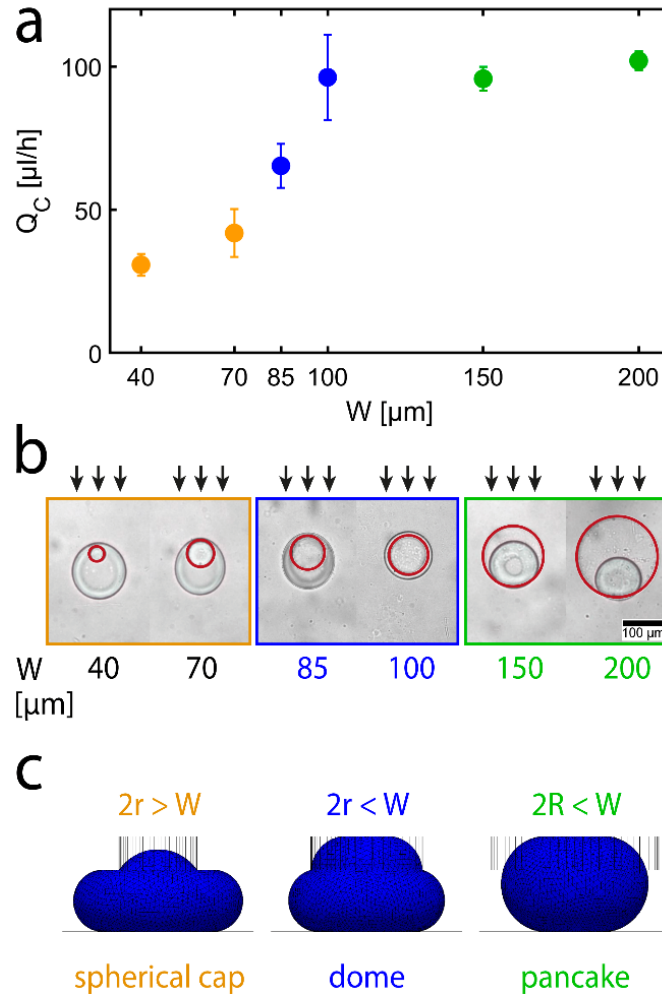


Figure 5.2: Trapping regimes. (a) Critical flow rates Q_C as function of the trap diameter W for trap depth $p = 30 \mu\text{m}$. (b) Optical microscopy images of drops that are immobilized through traps with increasing W . The traps are highlighted with a red circle for better visibility. (c) Surface Evolver renderings for the three trapping regimes. Reproduced from [198] with permission.

5.4.2 Simulations of Drop Shapes at Equilibrium

The magnitude of the trapping force is related to the shape drops attain when relaxing into traps. [199] To investigate this parameter, we simulate trapped drops in steady state using Surface Evolver. At equilibrium, the pressure jump ΔP across the interface of a drop must be constant throughout the drop surface. According to the Laplace equation, the curvature scales inversely with ΔP such that ΔP must also be constant throughout the drop surface. The equilibrium curvature of the in-trap drop interface is hence equal to the curvature of the drop interface inside the channel. For $R \gg h$, this can be approximated as $r = 8hR/(8R + \pi h)$; [200]–[202] with R the radius of the pancake in the channel. We herein consider this approximation to be also valid for $R \sim h$.

Our simulations reveal three different trapping regimes that depend on the ratio of W to the radius of curvature r : If $r > W/2$, the part of the drop that relaxes into the trap forms a spherical cap, as shown in Figure 5.2c to the left; we color-coded this regime orange. In this case, the deformation of the drop into the trap is limited by r , as has been described earlier. [199] By contrast, if $r < W/2$, the trap is wide enough for the drop to fully enter such

that it touches the trap ceiling and flattens against it. The part of the drop contained in this type of traps attains a shape what we call a dome, shown in Figure 5.2c in the middle; we color-coded this regime blue. In this regime, the deformation of the drop into the trap is limited by the trap depth p . If $R < W/2$, the projected area of the drop fully lies inside the trap and the drop attains the shape of a pancake that is much more relaxed compared to that in the channel, as shown in Figure 5.2c to the right; we color-coded this regime green.

5.4.3 Influence of Trap Depth

To test the validity of our categorization of the trapping regimes, we vary the trap depth p and evaluate the critical flow rate Q_c as a function of W . We expect Q_c to be independent of p if the drops form a spherical cap where $2r > W$. By contrast, we expect Q_c to increase with the trap depth p if $2r < W$ and $2R < W$ as in these cases the degree of relaxation of drops into traps increases with increasing trap depth. Indeed, if $2r > W$, we do not observe any influence of p on Q_c , as shown by the orange curves in Figure 5.3a. By contrast, if $2r < W$ and $2R < W$, Q_c increases with increasing p , as shown by the green and blue curves in Figure 5.3a. These results are in excellent agreement with our expectation and support our proposed trapping regimes.

Our and others [199] results suggest that the trapping force is influenced by the decrease of the surface energy of a drop upon its relaxation into a trap. An interesting physical proxy to quantify the drop deformation into the trap is to determine the volume fraction of the drop contained in the trap. Although this parameter has a priori no direct physical meaning and its relation to Q_c cannot be generalized, it allows to determine to what extent a drop relaxes into a trap of a given depth. This information is acquired by imaging a drop when it is squeezed in the Hele-Shaw cell and while it is trapped. We calculate the volume of the pancake contained in the Hele-Shaw cell with our model by measuring its radius R from optical microscopy images and taking the known value of the channel height h , as detailed in the Supporting Information. The volume of the drop contained in the trap is calculated from the volume difference of the pancakes located in the channel between the trapped and untrapped states. For $2r > W$, the drop volume contained in traps is independent of p , as shown by the orange solid symbols in Figure 5.3b. By contrast, if $2r < W$, the drop volume contained in traps increases with p , as shown by the blue solid symbols in Figure 5.3b. To test our findings, we evaluate the volume fraction of drops contained in traps with varying p using Surface Evolver simulations and a mathematical model, which is described in more details in chapter 5.4.5. The simulation and modelling results are in excellent agreement with our experimental ones, as shown in Figure 5.3b by empty symbols and crosses for simulations and modelling, respectively. They confirm that the extent of relaxation of drops in traps is independent of p if $2r > W$, but it increases with increasing p if $2r < W$. Further, the volume fraction of the drop in the trap scales with the change of the surface area of the drop for a fixed trap in-plane geometry. As a result, for a fixed in-plane trap geometry, the critical flow rate and the volume fraction of the drop in the trap do show similar slopes, as exemplified in blue for large, circular-shaped traps in Figures 3a and 3b. From this finding, we deduce that the range over which the trapping strength can be varied is much wider if the

diameter of traps exceeds $2r$. Note that this condition is not valid for very shallow traps, as detailed in chapter 5.4.5.

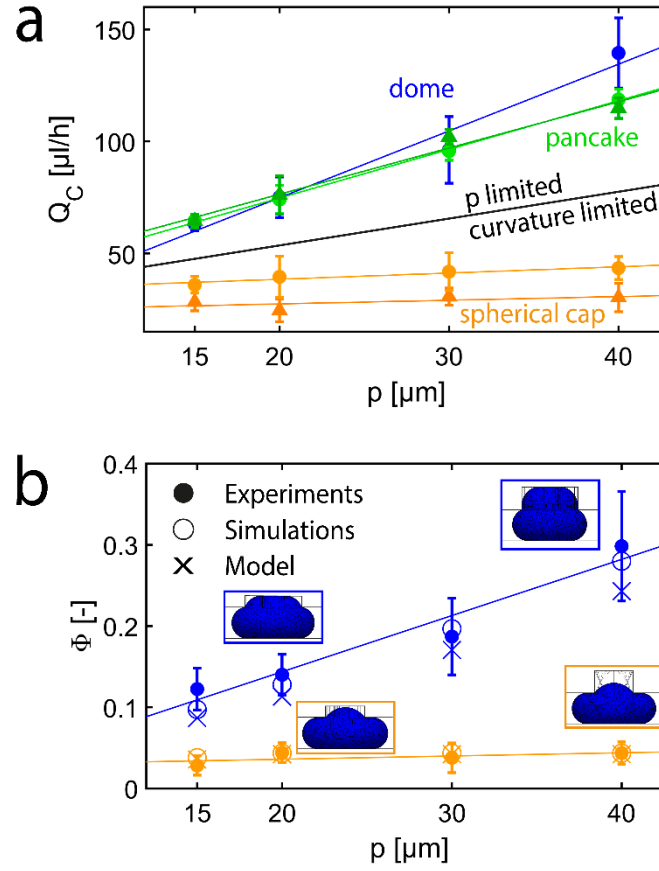


Figure 5.3: Influence of trap depth p on trapping. (a) Experimentally measured critical flow rates as a function of p for $W = 40$ (orange triangles) and $70 \mu\text{m}$ (orange circles), where trapped drops form spherical caps, $W = 100 \mu\text{m}$, where trapped drops form domes (blue), and $W = 150 \mu\text{m}$ (green circles) and $200 \mu\text{m}$ (green triangles), where trapped drops form pancakes. The solid lines represent linear fits to the results. (b) Volume fraction of the drop in the trap as a function of p for $W = 70 \mu\text{m}$ (orange) and $100 \mu\text{m}$ (blue). Filled symbols represent experimental results, empty symbols result from Surface Evolver simulations, and crosses result from the mathematical model for a drop volume that is equal to the one used for simulations. The solid lines are linear fits to the experimental results. Insets: Surface Evolver renderings of trapped drops for $p = 20 \mu\text{m}$ (left) and $40 \mu\text{m}$ (right) and $W = 100 \mu\text{m}$ (top) and $70 \mu\text{m}$ (bottom). Reproduced from [198] with permission.

5.4.4 Calculations of Surface Area Change Upon Trapping

To facilitate the design of traps possessing different trapping strengths it would be beneficial to predict Q_C for different trap geometries and drop sizes. This would require means to estimate the change in surface area that drops undergo when they enter a trap. To do so, we initially only consider the untrapped, squeezed pancakes located in the channel. Different models have been proposed to calculate the surface area and volume of drops squeezed into a pancake shape within a Hele-Shaw cell. [203], [204] These models provide accurate results of the surface area either for heavily [203] or minimally squeezed drops, [204] but not for both cases. To predict Q_C , we need a model that captures the drop shape for a wide range of aspect ratios. To achieve this goal, we describe the

drop as a cylinder surrounded by a half-torus, as sketched in the inset of Figure 5.4a. The volume of the drop is calculated as

$$V = 2\pi \int_0^r (\sqrt{r^2 - z^2} + x_a)^2 dz = \frac{\pi}{6} h^3 + \frac{\pi^2}{4} x_a h^2 + \pi x_a^2 h, \quad (5.1)$$

and the surface area is calculated as

$$A = 4\pi \int_0^r (\sqrt{r^2 - z^2} + x_a) \frac{r}{\sqrt{r^2 - z^2}} dz + 2\pi x_a^2 = \pi^2 x_a h + \pi h^2 + 2\pi x_a^2, \quad (5.2)$$

here, r is defined as the channel height divided by two, $h/2$, and x_a as the difference between R and r . For simplicity, we consider a constant radius of curvature r . Our model is in excellent agreement with the surface area data obtained from Surface Evolver simulations: The deviation of these two data sets is below 0.3% for channel heights varying between 10 μm , where drops are deformed to extremely high aspect ratios, and 120 μm , where drops are not confined and attain a spherical shape, as shown in Figure 5.4b. Indeed, this simple model shows excellent agreement over a wide range of channel heights that has not been achieved with the previously reported models, as shown in Figure 5.4a.

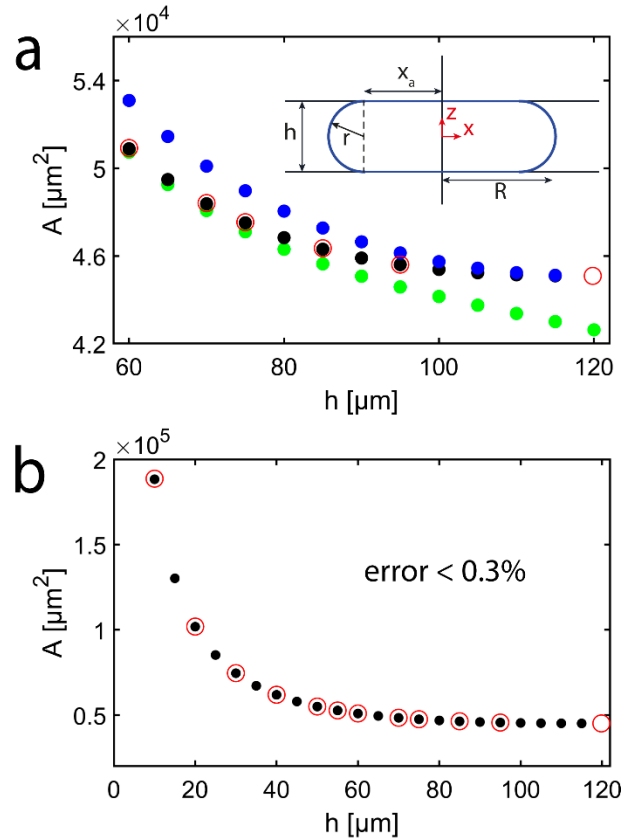


Figure 5.4: Surface area model for drops squeezed in a Hele-Shaw cell. (a) Surface area as a function of the channel height for the model proposed by Lv [203] using elliptic integrals (green), the model proposed by Nie et al. [204] using a truncated sphere (blue), the model proposed in this chapter using a disk with surrounding half-torus (black), and Surface Evolver simulation data (red, empty symbols). Inset: Schematic illustration of a drop squeezed in a channel of height

h with indicated radius of the resulting pancake R , the length of contact between drop and channel x_a , and the radius of curvature r . (b) A comparison of our model (black, solid symbols) with simulation data obtained from Surface Evolver (red, empty symbols) shows excellent agreement of the two data sets with errors below 0.3% over a wide range of channel heights. Reproduced from [198] with permission.

To describe the total surface area of trapped drops, that includes the surface area of the pancake and the cap that resides in the traps, we extend our model using geometric arguments. The calculated values are in excellent agreement with values obtained from Surface Evolver simulations, as shown in Figure 5.5a. These estimations greatly facilitate the design of optimized traps. The agreement between our model and simulations further indicates that the approximation for r is justified to describe the relaxation of drops into traps, even for cases where $R \sim h$.

5.4.5 Description of Model for Drops Relaxing into Spherical Microfluidic Traps

To describe the change in surface area of drops upon their trapping and the volume of the drop located in the trap, we model all parts of the drop with the same curvature. Note that the curvature is conserved in 3D, such that it is the product of the curvatures along two planes e.g. the xz -plane and the xy -plane. To describe the shape of the trapped drop, we integrate a curve revolving around the central z -axis of the trap along the z -direction. All the calculations for different trap geometries are given in Figure 5.5c. We compare the resulting surface areas of our model to simulations, initially starting with a drop volume of 0.9 nL, as shown in Figure 5.5a. Our model is in excellent agreement with the Surface Evolver simulation data for traps with widths of 40 μm and 70 μm , as shown by the orange filled squares and triangles in Figure 5.5a, respectively. We also calculate the surface area of drops trapped in traps with $W = 100 \mu\text{m}$ and $p \leq 40 \mu\text{m}$. Also in this case, the model predictions agree well with the simulations, as shown by the blue filled circles in Figure 5.5a.

To extend our model we increase the trap depth p to 55 μm , even though we did not experimentally address these cases. In these cases, $r < p$, such that the dome fully lies inside the trap; we color-coded this case purple. To describe the shape of drops in these traps, we add a cylinder with radius $W/2$ and height $(p - r)$ below the dome. A large volume fraction of the drops is located inside these deep traps such that the pancake in the channel starts to disappear; these cases are not captured properly by the model anymore. Although the error remains within 1% for $p = 55 \mu\text{m}$ compared to simulations the surface area found with the model is underestimated and the results diverge, as shown in Figure 5.5a. To test the validity of our model for deep traps that immobilize larger drops, we increase the drop volume two-fold to 1.8 nL, while keeping the trap geometry unchanged. As long as the fraction of the drop located in the Hele-Shaw cell attains a pancake shape, our model shows excellent agreement with simulations, even if traps are as deep as 55 μm , as shown in Figure 5.5b. The error between the calculations and simulations for larger drops in deep traps remains below 0.3%.

We introduce a calculation tree that enables the quantification of both the surface area change between the trapped and untrapped state of drops and the volume located in the trap. This information enables the prediction of the trapping force solely based on geometrical parameters h, p, W, R , as shown in Figure 5.5c. This part of the model is based on three different trapping regimes: Large and deep traps where $r < p$ such that drops are

described with a dome and a cylinder added below the dome, large traps where $r > p$ such that the part of the drop contained in the trap forms a dome, and small traps where the part of the drop that relaxes into the trap forms a spherical cap. The three regimes are labeled as 1, 2, and 3, and are color-coded in purple, blue, and orange, respectively in Figure 5.5c.

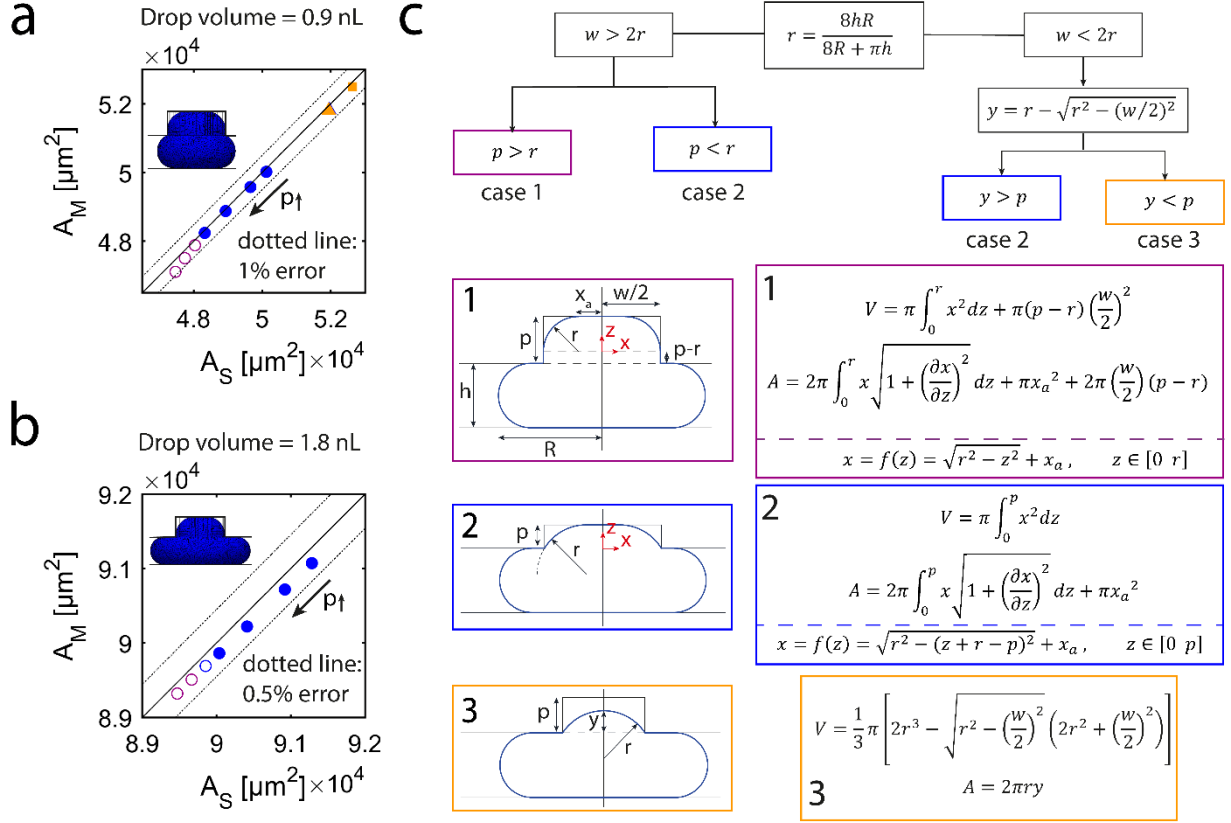


Figure 5.5: Model for quantifying the surface area change of drops between the trapped and untrapped state and the drop volume. (a-b) Surface area obtained from the model A_M compared to the surface area obtained from Surface Evolver simulations A_S for a drop volume of (a) 0.9 nL and (b) 1.8 nL for spherical traps with $W = 40 \mu\text{m}$ (squares), $W = 70 \mu\text{m}$ (triangles), $W = 100 \mu\text{m}$ (circles). Different data points with the same symbol indicate different trap depths p . The color code differentiates the different trapping regimes; dome with underlying cylinder (regime 1, purple), dome (regime 2, blue), and spherical cap (regime 3, orange). Empty symbols correspond to traps that were not experimentally addressed. The channel height was kept constant at $h = 55 \mu\text{m}$. Insets: Surface Evolver renderings of drops in traps with $W = 100 \mu\text{m}$ and $p = 40 \mu\text{m}$. The straight line indicates $y = x$, and dotted lines indicate (a) 1% error and (b) 0.5% error. (c) Three different trapping regimes. A calculation tree is presented to evaluate V and A . At first the radius of curvature r is calculated as a function of the pancake radius R and the channel height h . If $r > W/2$ a spherical cap deforms into the trap. The spherical cap can either freely deform into the trap, which leads to case 3, or is limited by the trap top, which leads to a flattening of the spherical cap and the formation of a dome, regime 2. If $r < W/2$ the drop forms a dome if $r > p$, case 2, or a dome with a cylinder below if $r < p$, case 1. Reproduced from [198] with permission.

5.4.6 Influence of the In-Plane Trap Geometry on the Critical Flow Rate

We expect the in-plane trap geometry to be another parameter to critically influence the trapping strength. To test this hypothesis, we quantify Q_C as a function of the number of corners of the trap, N . We design five different polygonal traps that have identical surface areas and $N = 3, 4, 5, 6$, or ∞ corners, as shown in optical micrographs in Figure 5.6a. We consider the initial circular trap as a limiting case with an infinite number of corners. For traps with a depth of $p = 15 \mu\text{m}$, the critical flow rate increases by 39% from $45.3 \pm 4.8 \mu\text{L/h}$ for $N = 3$ to $63.1 \pm 3.0 \mu\text{L/h}$ for $N = \infty$, as indicated by the green symbols in Figure 5.6b. The increase in Q_C with increasing N becomes even more pronounced for deeper traps: If p is increased to $40 \mu\text{m}$, Q_C increases by 60% from $86.9 \pm 8.3 \mu\text{m}$ to $139.4 \pm 15.6 \mu\text{m}$ for $N = 3$ and ∞ respectively, as shown in Figure 5.6b. To test if the stronger increase in Q_C for traps with $p = 40 \mu\text{m}$ is related to the higher absolute values of Q_C of deeper traps, we normalize all values of Q_C with the ones measured for the circular trap with the same p , Q_C/Q_C^∞ . Indeed, all normalized data falls onto a master curve where the critical flow rates Q_C of triangular and square traps is approximately 30% lower than that of circular and hexagonal counterparts, as shown in Figure 5.6c.

To investigate the reason for the measured increase in Q_C with increasing number of corners of the traps, we simulate the relaxation of drops into traps with different in-plane geometries in steady state using Surface Evolver. Drops that are immobilized in triangular traps strongly retract from the corners to maximize the radius of curvature and hence, to minimize the Laplace pressure within the drops, as shown in Figure 5.6d. The interface position can be understood as an equilibrium location in a geometrical singularity, in this case the corners, where the Laplace pressure within the drop is minimized. As a result of this retraction, the decrease in surface area is much smaller for drops immobilized in triangular traps than that of drops immobilized in circular traps, as shown in Figure 5.6e. The difference in surface area between trapped and untrapped drops increases with increasing N and is most likely a contributing factor for the observed increase in Q_C .

We hypothesize that another contributing reason for the observed decrease in Q_C with decreasing N could arise from increased drag forces. The size of gutters that form when drops retract from the trap corners increases with decreasing number of sides. As the size of gutters increases, more continuous phase can flow into them. We expect this effect to impart higher drag forces on the drop, thereby decreasing Q_C . To test this hypothesis, we artificially add gutters to the polygonal traps with $N = 4, 6, \infty$ by increasing their length threefold, as exemplified in the inset of Figure 5.6f for the circular trap. For these trap geometries, we use N^* to refer to the number of corners of the polygons and modified, elongated geometries. Additional gutters do not measurably influence Q_C of square traps. By contrast, they significantly decrease Q_C of hexagonal and circular traps, as shown in Figure 5.6f. Triangular and

square traps possess relatively large gutters and hence increased drag forces compared to circular traps, such that the addition of even larger gutters does not measurably alter Q_C . By contrast, hexagonal and circular traps possess gutters that are too small to significantly increase the drag force exerted on drops. If large gutters are added to these geometries, the drag force increases and hence, Q_C decreases. These results indicate that the lower values of Q_C for triangular and square traps can at least partially be assigned to the drag force exerted on drops by the continuous phase flowing into the gutters. Note that the orientation of triangular and square traps relative to the flow of the continuous phase does not measurably influence Q_C , as shown in Figure 5.7. These results demonstrate that Q_C can also be tuned over a considerable range with the in-plane geometry of traps.

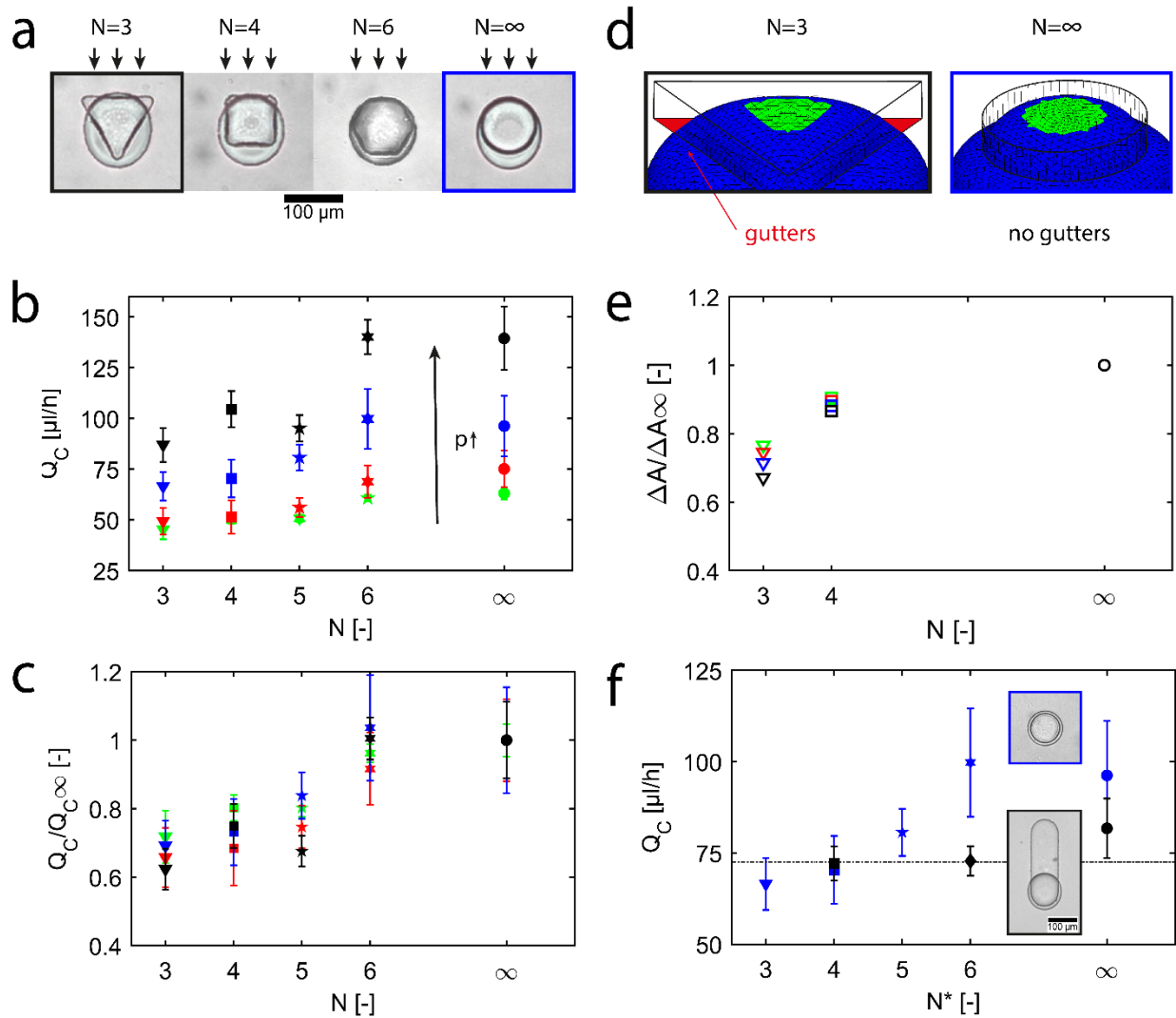


Figure 5.6: Influence of the in-plane geometry on the critical flow rates of microfluidic traps. (a) Optical micrographs of polygonal traps with $N = 3, 4, 6$, and ∞ sides, each one immobilizing a drop. (b) Q_C as a function of N for trap depths $p = 15$ μm (green), 20 μm (red), 30 μm (blue), and 40 μm (black). (c) Q_C normalized by $Q_{C\infty}$ for different trap heights. (d) Surface Evolver renderings of a triangular and a spherical trap holding drops in steady state. Drops in triangular traps retract from the sharp corners. The renderings are for illustration purposes only and are not to scale. (e) Surface Evolver simulation data of the surface area difference between the trapped and untrapped state normalized

by the value obtained for the circular trap for $p = 15 \mu\text{m}$ (green), $20 \mu\text{m}$ (red), $30 \mu\text{m}$ (blue), and $40 \mu\text{m}$ (black). (f) Q_C as a function of the modified number of sides N^* for traps with a depth $p = 30 \mu\text{m}$ with (black) and without (blue) artificial gutters. The black dotted line provides guidance to the eye. Insets: Optical micrographs of traps with (black) and without (blue) additional gutters for $N^* = \infty$. Reproduced from [198] with permission.

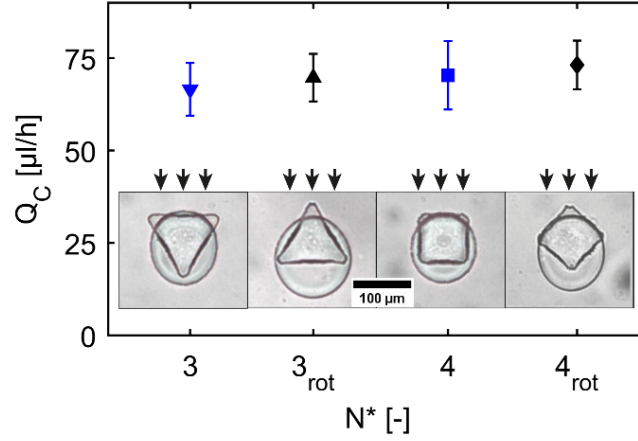


Figure 5.7: Influence of the orientation of triangular and square traps on Q_C . Q_C as a function of the number of corners of the polygonal trap N^* for two different orientations of traps. Insets: Micrographs of polygonal traps with different orientations relative to the flow of the continuous phase. Error bars represent the standard deviation and are calculated from at least 12 measurements. Reproduced from [198] with permission.

5.5 Discussion

The trapping force, $F_\gamma = \gamma \Delta A / d$, scales linearly with the change in surface area between trapped and untrapped drops, ΔA ; here d is the characteristic length scale over which the surface area changes. [199] To test if this scaling applies to the traps investigated here, we calculate ΔA using the model derived in chapter 5.4.5 and divide it by d , which we take as the length of the trap in the direction of flow for drops that are not entirely contained in the traps. For drops whose projected area is fully inside the trap, we take d as the sum of the pancake radius R of a drop inside the trap and that of a drop squeezed in the channel. The surface tension γ is kept constant and measured to be 4.5 mN/m for all experiments. Hence, we only consider the geometric components of $F_\gamma = \gamma \Delta A / d$. All our measured data points fall reasonably well onto a Master curve when we plot Q_C as a function of $\Delta A / d$, as shown in Figure 5.8, justifying our approach. This result indicates that we can predict Q_C using simple geometric arguments, thereby significantly facilitating the design of microfluidic trapping devices.

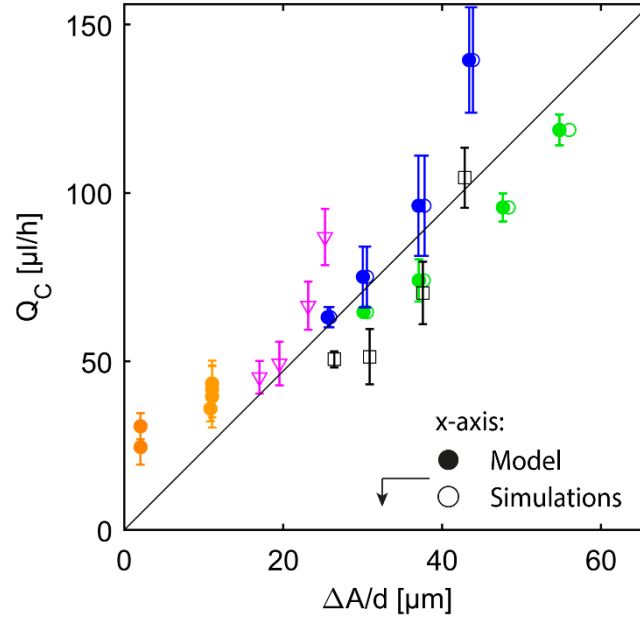


Figure 5.8: Influence of the trapping force on the critical flow rate Q_C . Q_C as a function of the surface area change ΔA divided by the characteristic length over which the change in surface energy takes place, d for circular traps with $W = 40 \mu\text{m}$ (dark orange circles), $70 \mu\text{m}$ (light orange circles), $100 \mu\text{m}$ (blue circles), and $150 \mu\text{m}$ (green circles), triangular traps with $W = 100 \mu\text{m}$ (magenta triangles), and square traps (black squares) with $W = 100 \mu\text{m}$. Filled symbols represent $\Delta A/d$ values obtained from the model and empty symbols represent $\Delta A/d$ results obtained from Surface Evolver simulations. Reproduced from [198] with permission.

5.5.1 Application to the Design of Hydrogels with Locally Varying Compositions

To demonstrate the potential of microfluidic trapping to design materials with locally varying compositions, we fabricate a microfluidic device with a 4 mm wide and 19.3 mm long Hele-Shaw cell that contains 570 traps. The device features two different types of traps, larger hexagonal traps with a critical flow rate $Q_{C,H} = 100 \pm 15 \mu\text{l/h}$ and smaller square traps with a critical flow rate $Q_{C,S} = 34 \pm 4 \mu\text{l/h}$. We form a first batch of aqueous drops that is labelled with a red fluorescing dye and immobilize the drops in all traps, as shown in Figure 5.9a. We subsequently rinse the Hele-Shaw cell at a flow rate $Q_{C,S} < Q < Q_{C,H}$, so that all drops that are immobilized in hexagonal traps remain trapped while the ones immobilized by square traps are removed, as shown in Figure 5.9b. We convert the trapped drops into hydrogel particles by exposing the device to UV light. A second batch of aqueous drops labelled with fluorescein is formed and these drops are immobilized in the remaining traps, as shown in Figure 5.9c. Untrapped drops are removed by rinsing the Hele-Shaw cell with $Q < Q_{C,S}$. The trapped drops are again converted into hydrogel microparticles through UV illumination, as shown in Figure 5.9d. Finally, we exchange the continuous oil phase with an aqueous phase containing poly(ethylene glycol) diacrylate (PEGDA) and a photoinitiator, as shown in Figure 5.9e. Note that our microgels are very stiff such that we do not observe any deformation of these particles during the introduction of the matrix precursor. We solidify this solution through UV illumination to obtain an intact hydrogel sheet whose composition can be deliberately changed with a high spatial precision, as shown in Figure 5.9f and 5.9g.

Hydrogel sheets fabricated in such microfluidic devices are mechanically stable and can be further processed and tested, as exemplified in Figure 5.9h.

To demonstrate the power and versatility of our platform to fabricate functional hydrogel sheets possessing well-defined microstructures, we design hydrogel sheets encompassing polyelectrolyte microgels. To achieve this goal, we produce aqueous drops loaded with the monomer AMPS (2-Acrylamido-2-methylpropane sulfonic acid), a crosslinker and a photoinitiator, and immobilize them in large hexagonal traps as used above. Untrapped drops are removed before the immobilized drops are converted into PAMPS particles by illuminating them with UV light to initiate the polymerization reaction within them, as shown in Figure 5.10a. The oil is subsequently replaced with an aqueous matrix solution containing PEGDA and a photoinitiator. During this solution exchange, the polyelectrolyte particles swell by at least a factor three in in-plane diameter, as indicated with the red circles in Figure 5.10a and 5.10b. After the matrix precursor is polymerized, the integral hydrogel sheet is removed from the microfluidic chip. To demonstrate its functionality, we immerse the microstructured sheet in a solution containing cresyl violet perchlorate, a positively charged dye. The dye is selectively adsorbed within the polyelectrolyte particles, as indicated by their color change in Figure 5.10c. This example demonstrates the versatility of this device in terms of materials that can be used to introduce micropatterns and functionality into hydrogel sheets.

Our results demonstrate that our device is well-suited to fabricate micropatterned hydrogel sheets. However, this technology is not limited to trapping water-in-oil emulsions but can also be used to trap oil-in-water emulsions. To demonstrate this feature, we form drops composed of a fluorinated oil that encompasses surfactants. These drops are dispersed in an aqueous solution containing PEGDA and a photoinitiator. After the traps are occupied by oil drops and untrapped drops are removed, we polymerize the PEGDA to obtain a hydrogel sheet possessing well-defined highly regular micro-pores, as shown in Figure 5.11.

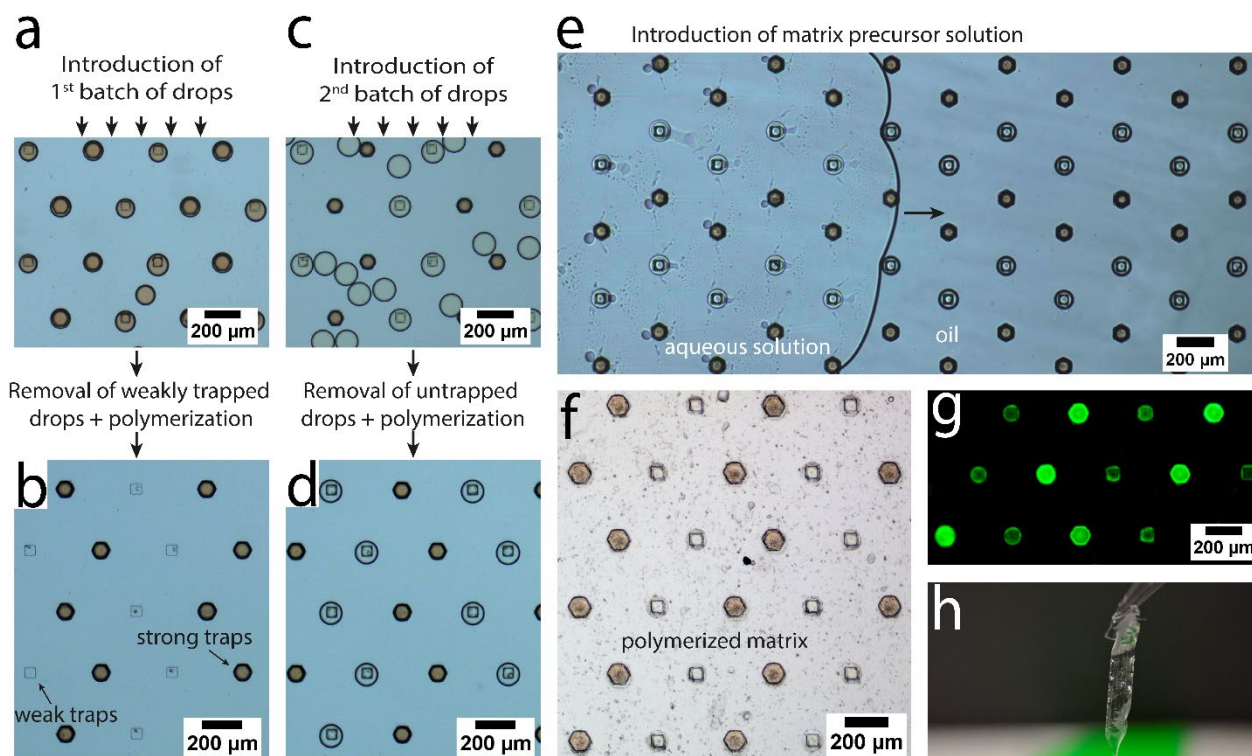


Figure 5.9: Fabrication of a hydrogel sheet with locally varying compositions. Optical micrographs of a microfluidic trapping device (a) as it is filled with a first batch of drops containing a red fluorescing label, (b) after the excessive drops have been rinsed out and the trapped drops have been converted into particles, (c) as it is filled with the second batch of drops, (d) after the excessive drops have been rinsed out and the trapped drops have been converted into particles, (e) as the continuous oil phase is replaced with an aqueous phase containing precursors of the matrix and (f) after the matrix material has been solidified to result in an integral hydrogel with locally varying compositions. (g) Fluorescence micrograph of an integral hydrogel sheet encompassing two different types of microgels. (h) Free-standing macroscopic hydrogel sheet. Reproduced from [198] with permission.

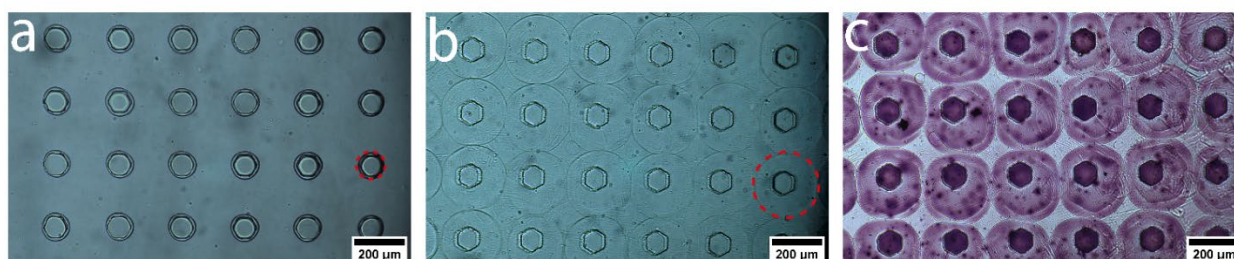


Figure 5.10: Fabrication of a selectively adsorbing hydrogel sheet. Optical micrographs of (a) polymerized PAMPS particles that are surrounded by an oil phase and (b) PAMPS particles swollen in the matrix precursor that was subsequently polymerized. (c) Integral hydrogel sheet that has been removed from the device and immersed in a cresyl violet-containing solution. Cresyl violet is electrostatically attracted by the anionic microparticles, as indicated by the selective staining. The red circles in (a) and (b) highlight the borders of the PAMPS microgels (a) before and (b) after they have been swollen in the matrix precursor solution. Reproduced from [198] with permission.

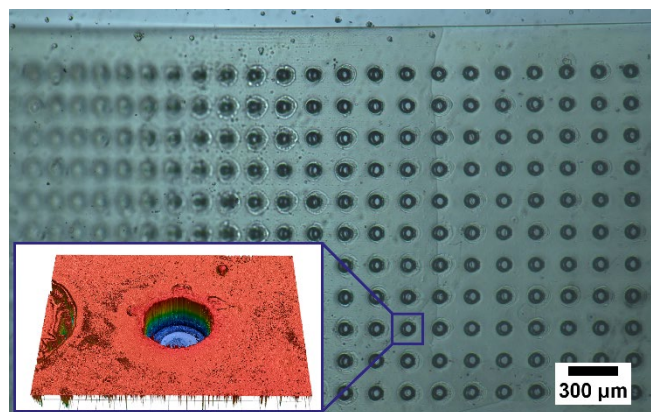


Figure 5.11: Fabrication of a porous hydrogel sheet from oil-in-water drops. Optical micrograph of a porous hydrogel sheet after it has been removed from the microfluidic device with the surface profile of a pore as an inset. Reproduced from [198] with permission.

5.6 Conclusion

We introduce a microfluidic Hele-Shaw trapping cell that enables the fabrication of hydrogel sheets with locally varying compositions. Importantly, our method enables tunable, abrupt changes in material composition on the $100\ \mu\text{m}$ length scale, in stark contrast to most additive manufacturing techniques that rely on the continuous deposition of filaments. The abrupt compositional changes are achieved by selectively immobilizing different types of drops at well-defined locations using traps possessing varying trapping strengths. We demonstrate that the trapping force strongly depends on the area, depth, and in-plane geometry of the traps and hence can be tuned over a wide range. Importantly, this method is not limited to the fabrication of hydrogels but can be extended to many other types of materials whose precursors can be processed into emulsion drops.

I believe that this platform opens up new possibilities to study how the mechanical properties of MRHs, such as stiffness and strength, depend on the position and distribution of microgels contained within quasi-2D hydrogel sheets. While I have shown in chapters 3 and 4 that these properties indeed depend on the architecture of the first network, its microstructure was only partially controllable, by means of varying the size, shape and volume fraction of the reinforcing microgels. However, the actual microstructure of the MRHs was still random. With the microfluidic Hele-Shaw cell I present in this chapter, we gain control over the precise spatial arrangement of different types of microgels. I hence believe that the presented device allows to elucidate design rules for stiff and strong hydrogels by precisely controlling their position and hence the microstructure of MRHs. This will provide design guidelines that will have direct implications for other, large-scale processing techniques, such as 3D printing. Additionally, the device may, by adding stimuli-responsive microgels to strategic locations within the sheet, enable the fabrication of the next generation of sensors and actuators. Further, conductive polymers could be employed in spatially well-defined regions in the hydrogel sheets to fabricate hydrogel sheets with abrupt alterations between conductive and insulating regions, which will likely find use in soft electronic switches or hydrogel batteries.

Chapter 6

Conclusion & Outlook

Many rapidly growing research areas including biomedical engineering or soft robotics continuously demand for new advanced, soft materials that better withstand fracture and deformation than their predecessors. An almost infinite source of inspiration for the development of new materials is the natural world, that provides us with many time-tested reinforcing strategies. In the field of soft materials, these natural models, such as tendons or the mussel byssus cuticle, often show superior stiffness and toughness compared to their synthetic counterparts. A contributing reason for this shortcoming of synthetic materials is their lacking microstructure. While many natural materials are structured on different length scales, synthetic hydrogels are often homogeneous and possess a well-defined structure only on the molecular level. A promising, bio-inspired route to design tough and load-bearing synthetic hydrogels is hence to introduce microstructures into them.

In this dissertation, I investigate how the microstructure of microgel-reinforced hydrogels influences their stiffness and fracture energy. I show that overall, the microgel volume fraction is the most important design parameter in MRHs. It determines firstly, alongside the microgel size, their shape and polydispersity, the rheological properties of the MRH precursors and whether they can be 3D printed, if the microgels contained in them are jammed, or if they are well suited for molding, if their viscosity is low. I show that the fracture energy of MRHs is independent of the microgel size, but linearly depends on the effective microgel volume fraction regardless of their degree of swelling. In contrast, the strength of MRHs depends on the microgel size, while the stiffness of fully swollen gels, as well as the work of extension depend on the microgel connectivity. I believe that the field of soft materials will greatly benefit from these insights, which provide design rules for the engineering of stiff and tough hydrogels, paired with advanced processability.

In chapters 3 and 4, I controlled the microstructure of bulk MRHs by varying the size, shape and volume fraction of the reinforcing microgels. However, the actual resulting microstructure was still random. To gain direct control over the microstructure in hydrogels, I introduce a microfluidic trapping device. It enables the introduction of spatially well-defined, periodic microstructures consisting of different types of reinforcing microgels into quasi-2D hydrogel sheets. By employing capillary traps with different trapping strengths and by positioning them at well-controlled locations, different types of drops containing microgel precursors are selectively immobilized on-chip, and are subsequently

polymerized to form microgels. I then insert the matrix precursor solution into the microfluidic chip and polymerize it to produce a hydrogel sheet that contains different types of microgels at well-defined locations. I believe that the presented microfluidic platform will allow, in the future, to elucidate more advanced design rules on how the stiffness and strength can be engineered in MRHs by precisely controlling the connectivity and arrangement of the microgels. These findings will be directly applicable to other, large-scale processing techniques, such as 3D printing.

I further envision that this device can be utilized to fabricate the next generation of hydrogel actuators. By positioning stimuli-responsive microgels at strategic locations within the hydrogel sheet, the latter can fold upon stimuli. The introduced device bears the advantage that a wide variety of materials and chemistries can be employed, if their precursors can be processed into emulsion drops. Additionally, by adding conductive polymers to the matrix, but not to the microgels, or vice-versa, hydrogels with abrupt alterations between conductive and insulating regions can be fabricated, which will likely advance the development of soft electronic switches or hydrogel batteries.

Bibliography

- [1] O. Wichterle und D. Lím, „Hydrophilic Gels for Biological Use“, *Nature*, Bd. 185, Nr. 4706, Art. Nr. 4706, Jan. 1960, doi: 10.1038/185117a0.
- [2] X. Zhao, X. Chen, H. Yuk, S. Lin, X. Liu, und G. Parada, „Soft Materials by Design: Unconventional Polymer Networks Give Extreme Properties“, *Chem. Rev.*, Bd. 121, Nr. 8, S. 4309–4372, Apr. 2021, doi: 10.1021/acs.chemrev.0c01088.
- [3] C. Creton und M. Ciccotti, „Fracture and adhesion of soft materials: a review“, *Rep. Prog. Phys.*, Bd. 79, Nr. 4, S. 046601, Apr. 2016, doi: 10.1088/0034-4885/79/4/046601.
- [4] T. Sakai, „Definition of Polymer Gels and Rubber Elasticity“, in *Physics of Polymer Gels*, John Wiley & Sons, Ltd, 2020, S. 45–75. doi: 10.1002/9783527346547.ch3.
- [5] W. Kuhn, „Dependence of the average transversal on the longitudinal dimensions of statistical coils formed by chain molecules“, *Journal of Polymer Science*, Bd. 1, Nr. 5, S. 380–388, 1946, doi: 10.1002/pol.1946.120010505.
- [6] H. M. James und E. Guth, „Simple presentation of network theory of rubber, with a discussion of other theories“, *Journal of Polymer Science Part B: Polymer Physics*, Bd. 34, Nr. 1, S. 7–36, 1996, doi: 10.1002/polb.1996.883.
- [7] G. J. Lake, A. G. Thomas, und D. Tabor, „The strength of highly elastic materials“, *Proceedings of the Royal Society of London. Series A. Mathematical and Physical Sciences*, Bd. 300, Nr. 1460, S. 108–119, Aug. 1967, doi: 10.1098/rspa.1967.0160.
- [8] R. Long, C.-Y. Hui, J. P. Gong, und E. Bouchbinder, „The Fracture of Highly Deformable Soft Materials: A Tale of Two Length Scales“, *Annu. Rev. Condens. Matter Phys.*, Bd. 12, Nr. 1, S. 71–94, März 2021, doi: 10.1146/annurev-conmatphys-042020-023937.
- [9] C. Creton, „50th Anniversary Perspective: Networks and Gels: Soft but Dynamic and Tough“, S. 20, 2017.
- [10] M. Shibayama, „Universality and Specificity of Polymer Gels Viewed by Scattering Methods“, *BCSJ*, Bd. 79, Nr. 12, S. 1799–1819, Dez. 2006, doi: 10.1246/bcsj.79.1799.
- [11] M. Shibayama, „Spatial inhomogeneity and dynamic fluctuations of polymer gels“, *Macromolecular Chemistry and Physics*, Bd. 199, Nr. 1, S. 1–30, 1998, doi: 10.1002/(SICI)1521-3935(19980101)199:1<1::AID-MACP1>3.0.CO;2-M.
- [12] C. Yang, T. Yin, und Z. Suo, „Polyacrylamide hydrogels. I. Network imperfection“, *Journal of the Mechanics and Physics of Solids*, Bd. 131, S. 43–55, Okt. 2019, doi: 10.1016/j.jmps.2019.06.018.
- [13] M. Zhong, R. Wang, K. Kawamoto, B. D. Olsen, und J. A. Johnson, „Quantifying the impact of molecular defects on polymer network elasticity“, *Science*, Bd. 353, Nr. 6305, S. 1264–1268, Sep. 2016, doi: 10.1126/science.aag0184.
- [14] M. Rubinstein und R. H. Colby, *Polymer Physics*, 1. Aufl. Oxford: Oxford University Press, 2003.
- [15] T. Sakai u. a., „Design and Fabrication of a High-Strength Hydrogel with Ideally Homogeneous Network Structure from Tetrahedron-like Macromonomers“, *Macromolecules*, Bd. 41, Nr. 14, S. 5379–5384, Juli 2008, doi: 10.1021/ma800476x.
- [16] M. Shibayama, X. Li, und T. Sakai, „Precision polymer network science with tetra-PEG gels—a decade history and future“, *Colloid Polym Sci*, Bd. 297, Nr. 1, S. 1–12, Jan. 2019, doi: 10.1007/s00396-018-4423-7.
- [17] H. Kamata, Y. Akagi, Y. Kayasuga-Kariya, U. Chung, und T. Sakai, „“Nonswellable” Hydrogel Without Mechanical Hysteresis“, *Science*, Bd. 343, Nr. 6173, S. 873–875, Feb. 2014, doi: 10.1126/science.1247811.
- [18] S. C. Grindy u. a., „Control of hierarchical polymer mechanics with bioinspired metal-coordination dynamics“, *Nature Mater*, Bd. 14, Nr. 12, S. 1210–1216, Dez. 2015, doi: 10.1038/nmat4401.

- [19] Y. Okumura und K. Ito, „The Polyrotaxane Gel: A Topological Gel by Figure-of-Eight Cross-links“, *Advanced Materials*, Bd. 13, Nr. 7, S. 485–487, 2001, doi: 10.1002/1521-4095(200104)13:7<485::AID-ADMA485>3.0.CO;2-T.
- [20] J. E. Mark, „Elastomeric Networks with Bimodal Chain-Length Distributions“, *Acc. Chem. Res.*, Bd. 27, Nr. 9, S. 271–278, Sep. 1994, doi: 10.1021/ar00045a003.
- [21] X. Liang u. a., „Anisotropically Fatigue-Resistant Hydrogels“, *Advanced Materials*, Bd. 33, Nr. 30, S. 2102011, 2021, doi: 10.1002/adma.202102011.
- [22] C. M. Hassan und N. A. Peppas, „Structure and Morphology of Freeze/Thawed PVA Hydrogels“, *Macromolecules*, Bd. 33, Nr. 7, S. 2472–2479, Apr. 2000, doi: 10.1021/ma9907587.
- [23] A. Kumar und S. S. Han, „PVA-based hydrogels for tissue engineering: A review“, *International Journal of Polymeric Materials and Polymeric Biomaterials*, Bd. 66, Nr. 4, S. 159–182, März 2017, doi: 10.1080/00914037.2016.1190930.
- [24] Z. Liu, Y. Faraj, X.-J. Ju, W. Wang, R. Xie, und L.-Y. Chu, „Nanocomposite smart hydrogels with improved responsiveness and mechanical properties: A mini review“, *Journal of Polymer Science Part B: Polymer Physics*, Bd. 56, Nr. 19, S. 1306–1313, 2018, doi: 10.1002/polb.24723.
- [25] J. Fu, „Strong and tough hydrogels crosslinked by multi-functional polymer colloids“, *Journal of Polymer Science Part B: Polymer Physics*, Bd. 56, Nr. 19, S. 1336–1350, 2018, doi: 10.1002/polb.24728.
- [26] S. Merino, C. Martín, K. Kostarelos, M. Prato, und E. Vázquez, „Nanocomposite Hydrogels: 3D Polymer–Nanoparticle Synergies for On-Demand Drug Delivery“, *ACS Nano*, Bd. 9, Nr. 5, S. 4686–4697, Mai 2015, doi: 10.1021/acsnano.5b01433.
- [27] P. Schexnailder und G. Schmidt, „Nanocomposite polymer hydrogels“, *Colloid Polym Sci*, Bd. 287, Nr. 1, S. 1–11, Jan. 2009, doi: 10.1007/s00396-008-1949-0.
- [28] T. M. Atanackovic und A. (Ardéshir) Guran, *Theory of Elasticity for Scientists and Engineers [electronic resource]*. Boston, MA : Birkhäuser Boston : Imprint: Birkhäuser, 2000. Zugegriffen: 5. Juni 2022. [Online]. Verfügbar unter: <http://archive.org/details/theoryelasticity00atan>
- [29] „Elasticity (physics)“, *Wikipedia*. 21. April 2022. Zugegriffen: 5. Juni 2022. [Online]. Verfügbar unter: [https://en.wikipedia.org/w/index.php?title=Elasticity_\(physics\)&oldid=1083886093](https://en.wikipedia.org/w/index.php?title=Elasticity_(physics)&oldid=1083886093)
- [30] Z. P. BAŽANT, „Scaling of quasibrittle fracture: asymptotic analysis“, *International Journal of Fracture*, Bd. 83, Nr. 1, S. 19, Jan. 1997, doi: 10.1023/A:1007387823522.
- [31] R. E. Webber, C. Creton, H. R. Brown, und J. P. Gong, „Large Strain Hysteresis and Mullins Effect of Tough Double-Network Hydrogels“, *Macromolecules*, Bd. 40, Nr. 8, S. 2919–2927, Apr. 2007, doi: 10.1021/ma062924y.
- [32] L. Mullins, „Softening of Rubber by Deformation“, *Rubber Chemistry and Technology*, Bd. 42, Nr. 1, S. 339–362, März 1969, doi: 10.5254/1.3539210.
- [33] J. Diani, B. Fayolle, und P. Gilormini, „A review on the Mullins effect“, *European Polymer Journal*, Bd. 45, Nr. 3, S. 601–612, März 2009, doi: 10.1016/j.eurpolymj.2008.11.017.
- [34] J. P. Gong, Y. Katsuyama, T. Kurokawa, und Y. Osada, „Double-Network Hydrogels with Extremely High Mechanical Strength“, *Advanced Materials*, Bd. 15, Nr. 14, S. 1155–1158, 2003, doi: <https://doi.org/10.1002/adma.200304907>.
- [35] J. P. Gong, „Why are double network hydrogels so tough?“, *Soft Matter*, Bd. 6, Nr. 12, S. 2583, 2010, doi: 10.1039/b924290b.
- [36] J.-Y. Sun u. a., „Highly stretchable and tough hydrogels“, *Nature*, Bd. 489, Nr. 7414, S. 133–136, Sep. 2012, doi: 10.1038/nature11409.
- [37] T. Nakajima, H. Furukawa, Y. Tanaka, T. Kurokawa, Y. Osada, und J. P. Gong, „True Chemical Structure of Double Network Hydrogels“, *Macromolecules*, Bd. 42, Nr. 6, S. 2184–2189, März 2009, doi: 10.1021/ma802148p.
- [38] M. Huang, H. Furukawa, Y. Tanaka, T. Nakajima, Y. Osada, und J. P. Gong, „Importance of Entanglement between First and Second Components in High-Strength Double Network Gels“, *Macromolecules*, Bd. 40, Nr. 18, S. 6658–6664, Sep. 2007, doi: 10.1021/ma062482q.

- [39] T. Nakajima, T. Kurokawa, S. Ahmed, W. Wu, und J. P. Gong, „Characterization of internal fracture process of double network hydrogels under uniaxial elongation“, *Soft Matter*, Bd. 9, Nr. 6, S. 1955–1966, Jan. 2013, doi: 10.1039/C2SM27232F.
- [40] T. Tominaga u. a., „The molecular origin of enhanced toughness in double-network hydrogels: A neutron scattering study“, *Polymer*, Bd. 48, Nr. 26, S. 7449–7454, Dez. 2007, doi: 10.1016/j.polymer.2007.10.016.
- [41] H. R. Brown, „A Model of the Fracture of Double Network Gels“, *Macromolecules*, Bd. 40, Nr. 10, S. 3815–3818, Mai 2007, doi: 10.1021/ma062642y.
- [42] P. Millereau u. a., „Mechanics of elastomeric molecular composites“, *Proceedings of the National Academy of Sciences*, Bd. 115, Nr. 37, S. 9110–9115, Sep. 2018, doi: 10.1073/pnas.1807750115.
- [43] Y. Chen, G. Sanoja, und C. Creton, „Mechanochemistry unveils stress transfer during sacrificial bond fracture of tough multiple network elastomers“, *Chemical Science*, Bd. 12, Nr. 33, S. 11098–11108, 2021, doi: 10.1039/d1sc03352b.
- [44] R. Long und C.-Y. Hui, „Fracture toughness of hydrogels: measurement and interpretation“, *Soft Matter*, Bd. 12, Nr. 39, S. 8069–8086, 2016, doi: 10.1039/C6SM01694D.
- [45] S. Lin, Y. Zhou, und X. Zhao, „Designing extremely resilient and tough hydrogels via delayed dissipation“, *Extreme Mechanics Letters*, Bd. 1, S. 70–75, Dez. 2014, doi: 10.1016/j.eml.2014.11.002.
- [46] E. Ducrot, Y. Chen, M. Bulters, R. P. Sijbesma, und C. Creton, „Toughening Elastomers with Sacrificial Bonds and Watching Them Break“, *Science*, Bd. 344, Nr. 6180, S. 186–189, Apr. 2014, doi: 10.1126/science.1248494.
- [47] Y. Qi, Z. Zou, J. Xiao, und R. Long, „Mapping the nonlinear crack tip deformation field in soft elastomer with a particle tracking method“, *Journal of the Mechanics and Physics of Solids*, Bd. 125, S. 326–346, Apr. 2019, doi: 10.1016/j.jmps.2018.12.018.
- [48] I. Kolvin, J. M. Kolinski, J. P. Gong, und J. Fineberg, „How Supertough Gels Break“, *Phys. Rev. Lett.*, Bd. 121, Nr. 13, S. 135501, Sep. 2018, doi: 10.1103/PhysRevLett.121.135501.
- [49] C. Chen, Z. Wang, und Z. Suo, „Flaw sensitivity of highly stretchable materials“, *Extreme Mechanics Letters*, Bd. 10, S. 50–57, Jan. 2017, doi: 10.1016/j.eml.2016.10.002.
- [50] A. G. Thomas, „Rupture of rubber. V. Cut growth in natural rubber vulcanizates“, *Journal of Polymer Science*, Bd. 31, Nr. 123, S. 467–480, 1958, doi: 10.1002/pol.1958.1203112324.
- [51] A. Livne, E. Bouchbinder, I. Svetlizky, und J. Fineberg, „The Near-Tip Fields of Fast Cracks“, *Science*, Bd. 327, Nr. 5971, S. 1359–1363, März 2010, doi: 10.1126/science.1180476.
- [52] T. Zhang, S. Lin, H. Yuk, und X. Zhao, „Predicting fracture energies and crack-tip fields of soft tough materials“, *Extreme Mechanics Letters*, Bd. 4, S. 1–8, Sep. 2015, doi: 10.1016/j.eml.2015.07.007.
- [53] Y. Tanaka, R. Kuwabara, Y.-H. Na, T. Kurokawa, J. P. Gong, und Y. Osada, „Determination of Fracture Energy of High Strength Double Network Hydrogels“, *J. Phys. Chem. B*, Bd. 109, Nr. 23, S. 11559–11562, Juni 2005, doi: 10.1021/jp0500790.
- [54] Y. Tanaka, „A local damage model for anomalous high toughness of double-network gels“, *EPL*, Bd. 78, Nr. 5, S. 56005, Mai 2007, doi: 10.1209/0295-5075/78/56005.
- [55] Q. M. Yu, Y. Tanaka, H. Furukawa, T. Kurokawa, und J. P. Gong, „Direct Observation of Damage Zone around Crack Tips in Double-Network Gels“, *Macromolecules*, Bd. 42, Nr. 12, S. 3852–3855, Juni 2009, doi: 10.1021/ma900622s.
- [56] A. S. Argon, *The Physics of Deformation and Fracture of Polymers*. Cambridge: Cambridge University Press, 2013. doi: 10.1017/CBO9781139033046.
- [57] R. M. McMECKING und A. g. Evans, „Mechanics of Transformation-Toughening in Brittle Materials“, *Journal of the American Ceramic Society*, Bd. 65, Nr. 5, S. 242–246, 1982, doi: 10.1111/j.1151-2916.1982.tb10426.x.
- [58] J. R. Rice und R. Thomson, „Ductile versus brittle behaviour of crystals“, *The Philosophical Magazine: A Journal of Theoretical Experimental and Applied Physics*, Bd. 29, Nr. 1, S. 73–97, Jan. 1974, doi: 10.1080/14786437408213555.

- [59] P. K. Mallick, *Fiber-Reinforced Composites: Materials, Manufacturing, and Design, Third Edition*, 3. Aufl. Boca Raton: CRC Press, 2007. doi: 10.1201/9781420005981.
- [60] *Biomechanics*. Zugegriffen: 6. Juni 2022. [Online]. Verfügbar unter: <https://link.springer.com/book/10.1007/978-1-4757-2257-4>
- [61] X. Zhao, „Multi-scale multi-mechanism design of tough hydrogels: building dissipation into stretchy networks“, *Soft Matter*, Bd. 10, Nr. 5, S. 672–687, 2014, doi: 10.1039/C3SM52272E.
- [62] Y. Zheng u. a., „How chain dynamics affects crack initiation in double-network gels“, *PNAS*, Bd. 118, Nr. 49, Dez. 2021, doi: 10.1073/pnas.2111880118.
- [63] S. Liang, Z. L. Wu, J. Hu, T. Kurokawa, Q. M. Yu, und J. P. Gong, „Direct Observation on the Surface Fracture of Ultrathin Film Double-Network Hydrogels“, *Macromolecules*, Bd. 44, Nr. 8, S. 3016–3020, Apr. 2011, doi: 10.1021/ma2000527.
- [64] L. F. Gockowski u. a., „Engineering crack tortuosity in printed polymer–polymer composites through ordered pores“, *Mater. Horiz.*, Bd. 7, Nr. 7, S. 1854–1860, 2020, doi: 10.1039/D0MH00331J.
- [65] F. Meng u. a., „Tree Frog-Inspired Structured Hydrogel Adhesive with Regulated Liquid“, *Advanced Materials Interfaces*, Bd. 8, Nr. 18, S. 2100528, 2021, doi: 10.1002/admi.202100528.
- [66] S. Baik, J. Kim, H. J. Lee, T. H. Lee, und C. Pang, „Highly Adaptable and Biocompatible Octopus-Like Adhesive Patches with Meniscus-Controlled Unfoldable 3D Microtips for Underwater Surface and Hairy Skin“, *Advanced Science*, Bd. 5, Nr. 8, S. 1800100, 2018, doi: 10.1002/advs.201800100.
- [67] P. Rao u. a., „Tough Hydrogels with Fast, Strong, and Reversible Underwater Adhesion Based on a Multiscale Design“, *Adv. Mater.*, Bd. 30, Nr. 32, S. 1801884, Aug. 2018, doi: 10.1002/adma.201801884.
- [68] P. Fratzl, O. Kolednik, F. D. Fischer, und M. N. Dean, „The mechanics of tessellations – bioinspired strategies for fracture resistance“, *Chem. Soc. Rev.*, Bd. 45, Nr. 2, S. 252–267, 2016, doi: 10.1039/C5CS00598A.
- [69] A. R. Studart, „Additive manufacturing of biologically-inspired materials“, *Chemical Society Reviews*, Bd. 45, Nr. 2, S. 359–376, 2016, doi: 10.1039/c5cs00836k.
- [70] Y. Gu, L. Yu, J. Mou, D. Wu, P. Zhou, und M. Xu, „Mechanical properties and application analysis of spider silk bionic material“, *e-Polymers*, Bd. 20, Nr. 1, S. 443–457, Jan. 2020, doi: 10.1515/epoly-2020-0049.
- [71] Q. Wang und H. C. Schniepp, „Strength of Recluse Spider’s Silk Originates from Nanofibrils“, *ACS Macro Lett.*, Bd. 7, Nr. 11, S. 1364–1370, Nov. 2018, doi: 10.1021/acsmacrolett.8b00678.
- [72] J. Sun und B. Bhushan, „Hierarchical structure and mechanical properties of nacre: a review“, *RSC Adv.*, Bd. 2, Nr. 20, S. 7617–7632, Aug. 2012, doi: 10.1039/C2RA20218B.
- [73] A. R. Studart und R. M. Erb, „Bioinspired materials that self-shape through programmed microstructures“, *Soft Matter*, Bd. 10, Nr. 9, S. 1284–1294, 2014, doi: 10.1039/c3sm51883c.
- [74] H. Thérien-Aubin, Z. L. Wu, Z. Nie, und E. Kumacheva, „Multiple Shape Transformations of Composite Hydrogel Sheets“, *J. Am. Chem. Soc.*, Bd. 135, Nr. 12, S. 4834–4839, März 2013, doi: 10.1021/ja400518c.
- [75] Z. L. Wu u. a., „Three-dimensional shape transformations of hydrogel sheets induced by small-scale modulation of internal stresses“, *Nat Commun*, Bd. 4, Nr. 1, S. 1586, Juni 2013, doi: 10.1038/ncomms2549.
- [76] M. Badaoui, G. Kresge, C. Ushay, J. Marthelot, und P.-T. Brun, „Formation of Pixelated Elastic Films via Capillary Suction of Curable Elastomers in Templated Hele–Shaw Cells“, *Advanced Materials*, Bd. n/a, Nr. n/a, S. 2109682, doi: 10.1002/adma.202109682.
- [77] H. Du, A. Cont, M. Steinacher, und E. Amstad, „Fabrication of Hexagonal-Prismatic Granular Hydrogel Sheets“, *Langmuir*, Bd. 34, Nr. 11, S. 3459–3466, März 2018, doi: 10.1021/acs.langmuir.7b04163.
- [78] U. N. Lee u. a., „Layer-by-layer fabrication of 3D hydrogel structures using open microfluidics“, *Lab Chip*, Bd. 20, Nr. 3, S. 525–536, 2020, doi: 10.1039/C9LC00621D.

- [79] T. J. Hinton, A. Lee, und A. W. Feinberg, „3D bioprinting from the micrometer to millimeter length scales: Size does matter“, *Current Opinion in Biomedical Engineering*, Bd. 1, S. 31–37, 2017, doi: 10.1016/j.cobme.2017.02.004.
- [80] Y. S. Zhang und A. Khademhosseini, „Advances in engineering hydrogels“, *Science*, Bd. 356, Nr. 6337, S. eaaf3627, Mai 2017, doi: 10.1126/science.aaf3627.
- [81] A. Navaei, N. Moore, R. T. Sullivan, D. Truong, R. Q. Migrino, und M. Nikkhah, „Electrically conductive hydrogel-based micro-topographies for the development of organized cardiac tissues“, *RSC Advances*, Bd. 7, Nr. 6, S. 3302–3312, 2017, doi: 10.1039/C6RA26279A.
- [82] G. C. Engelmayr, M. Cheng, C. J. Bettinger, J. T. Borenstein, R. Langer, und L. E. Freed, „Accordion-like honeycombs for tissue engineering of cardiac anisotropy“, *Nature Mater*, Bd. 7, Nr. 12, Art. Nr. 12, Dez. 2008, doi: 10.1038/nmat2316.
- [83] D. C. Duffy, J. C. McDonald, O. J. A. Schueller, und G. M. Whitesides, „Rapid Prototyping of Microfluidic Systems in Poly(dimethylsiloxane)“, *Anal. Chem.*, Bd. 70, Nr. 23, S. 4974–4984, Dez. 1998, doi: 10.1021/ac980656z.
- [84] M. S. Hahn, L. J. Taite, J. J. Moon, M. C. Rowland, K. A. Ruffino, und J. L. West, „Photolithographic patterning of polyethylene glycol hydrogels“, *Biomaterials*, Bd. 27, Nr. 12, S. 2519–2524, Apr. 2006, doi: 10.1016/j.biomaterials.2005.11.045.
- [85] S. Nemir, H. N. Hayenga, und J. L. West, „PEGDA hydrogels with patterned elasticity: Novel tools for the study of cell response to substrate rigidity“, *Biotechnol. Bioeng.*, Bd. 105, Nr. 3, S. 636–644, Feb. 2010, doi: 10.1002/bit.22574.
- [86] M. S. Hahn, J. S. Miller, und J. L. West, „Three-dimensional biochemical and biomechanical patterning of hydrogels for guiding cell behavior“, *Advanced Materials*, Bd. 18, Nr. 20, S. 2679–2684, 2006, doi: 10.1002/adma.200600647.
- [87] R. G. Wylie, S. Ahsan, Y. Aizawa, K. L. Maxwell, C. M. Morshead, und M. S. Shoichet, „Spatially controlled simultaneous patterning of multiple growth factors in three-dimensional hydrogels“, *Nature Mater*, Bd. 10, Nr. 10, Art. Nr. 10, Okt. 2011, doi: 10.1038/nmat3101.
- [88] R. M. Erb, J. S. Sander, R. Grisch, und A. R. Studart, „Self-shaping composites with programmable bioinspired microstructures“, *Nat Commun*, Bd. 4, Nr. 1, S. 1712, Juni 2013, doi: 10.1038/ncomms2666.
- [89] J. Kim, J. A. Hanna, M. Byun, C. D. Santangelo, und R. C. Hayward, „Designing Responsive Buckled Surfaces by Halftone Gel Lithography“, *Science*, Bd. 335, Nr. 6073, S. 1201–1205, März 2012, doi: 10.1126/science.1215309.
- [90] B. Özkale u. a., „Modular soft robotic microdevices for dexterous biomanipulation“, *Lab on a Chip*, Bd. 19, Nr. 5, S. 778–788, 2019, doi: 10.1039/c8lc01200h.
- [91] X. Ma u. a., „Deterministically patterned biomimetic human iPSC-derived hepatic model via rapid 3D bioprinting“, *Proc Natl Acad Sci USA*, Bd. 113, Nr. 8, S. 2206–2211, Feb. 2016, doi: 10.1073/pnas.1524510113.
- [92] H. Jia u. a., „Universal Soft Robotic Microgripper“, *Small*, S. 8, 2019.
- [93] H. S. Hele-Shaw, „Flow of Water“, *Nature*, Bd. 58, Nr. 1509, Art. Nr. 1509, Sep. 1898, doi: 10.1038/058520a0.
- [94] W. Sun u. a., „The bioprinting roadmap“, *Biofabrication*, Bd. 12, Nr. 2, S. 022002, Feb. 2020, doi: 10.1088/1758-5090/ab5158.
- [95] J. Li, C. Wu, P. K. Chu, und M. Gelinsky, „3D printing of hydrogels: Rational design strategies and emerging biomedical applications“, *Materials Science and Engineering: R: Reports*, Bd. 140, S. 100543, Apr. 2020, doi: 10.1016/j.mser.2020.100543.
- [96] A. Sydney Gladman, E. A. Matsumoto, R. G. Nuzzo, L. Mahadevan, und J. A. Lewis, „Biomimetic 4D printing“, *Nature Mater*, Bd. 15, Nr. 4, S. 413–418, Apr. 2016, doi: 10.1038/nmat4544.
- [97] M. Champeau, D. A. Heinze, T. N. Viana, E. R. de Souza, A. C. Chinellato, und S. Titotto, „4D Printing of Hydrogels: A Review“, *Adv. Funct. Mater.*, Bd. 30, Nr. 31, S. 1910606, Aug. 2020, doi: 10.1002/adfm.201910606.
- [98] M. J. Harrington, A. Masic, und N. Holten-Andersen, „Iron-clad fibers : A metal-based biological strategy for hard flexible coatings“, *Science*, Bd. 328, Nr. April, S. 216–220, 2010.

- [99] T. Priemel, E. Degtyar, M. N. Dean, und M. J. Harrington, „Rapid self-assembly of complex biomolecular architectures during mussel byssus biofabrication“, *Nature Communications*, Bd. 8, S. 14539, 2017, doi: 10.1038/ncomms14539.
- [100] N. Holten-Andersen, G. E. Fantner, S. Hohlbauch, J. H. Waite, und F. W. Zok, „Protective coatings on extensible biofibres“, *Nat Mater*, Bd. 6, Nr. 9, S. 669–672, 2007, doi: 10.1038/nmat1956.
- [101] N. Holten-Andersen, T. E. Mates, M. S. Toprak, G. D. Stucky, F. W. Zok, und J. H. Waite, „Metals and the integrity of a biological coating: The cuticle of mussel byssus“, *Langmuir*, Bd. 25, Nr. 6, S. 3323–3326, 2009, doi: 10.1021/la8027012.
- [102] C. A. Monnier, D. G. DeMartini, und J. H. Waite, „Intertidal exposure favors the soft-studded armor of adaptive mussel coatings“, *Nat Commun*, Bd. 9, Nr. 1, S. 3424, Dez. 2018, doi: 10.1038/s41467-018-05952-5.
- [103] D. E. Fullenkamp, D. G. Barrett, D. R. Miller, J. W. Kurutz, und P. B. Messersmith, „pH-dependent cross-linking of catechols through oxidation via Fe^{3+} and potential implications for mussel adhesion“, *RSC Adv.*, Bd. 4, Nr. 48, S. 25127–25134, 2014, doi: 10.1039/C4RA03178D.
- [104] D. G. Barrett, D. E. Fullenkamp, L. He, N. Holten-Andersen, K. Y. C. Lee, und P. B. Messersmith, „pH-Based Regulation of Hydrogel Mechanical Properties Through Mussel-Inspired Chemistry and Processing“, *Adv. Funct. Mater.*, Bd. 23, Nr. 9, S. 1111–1119, März 2013, doi: 10.1002/adfm.201201922.
- [105] J. H. Waite, „Mussel adhesion – essential footwork“, *J Exp Biol*, Bd. 220, Nr. 4, S. 517–530, Feb. 2017, doi: 10.1242/jeb.134056.
- [106] F. Jehle, E. Macías-Sánchez, S. Sviben, P. Fratzl, L. Bertinetti, und M. J. Harrington, „Hierarchically-structured metalloprotein composite coatings biofabricated from co-existing condensed liquid phases“, *Nat Commun*, Bd. 11, Nr. 1, S. 862, Dez. 2020, doi: 10.1038/s41467-020-14709-y.
- [107] T. I. U. of P. and A. Chemistry (IUPAC), „IUPAC - microgel (M03901)“. <https://goldbook.iupac.org/terms/view/M03901> (zugegriffen 10. Juni 2022).
- [108] A. C. Daly, L. Riley, T. Segura, und J. A. Burdick, „Hydrogel microparticles for biomedical applications“, *Nature Reviews Materials*, Bd. 5, Nr. 1, Art. Nr. 1, Jan. 2020, doi: 10.1038/s41578-019-0148-6.
- [109] A. S. Caldwell, B. A. Aguado, und K. S. Anseth, „Designing Microgels for Cell Culture and Controlled Assembly of Tissue Microenvironments“, *Adv. Funct. Mater.*, Bd. 30, Nr. 37, S. 1907670, Sep. 2020, doi: 10.1002/adfm.201907670.
- [110] H. Yuk u. a., „Rapid and coagulation-independent haemostatic sealing by a paste inspired by barnacle glue“, *Nat Biomed Eng*, Bd. 5, Nr. 10, Art. Nr. 10, Okt. 2021, doi: 10.1038/s41551-021-00769-y.
- [111] S. Moser u. a., „Hydroelastomers: soft, tough, highly swelling composites“, arXiv, arXiv:2203.17131, März 2022. doi: 10.48550/arXiv.2203.17131.
- [112] F. G. Downs u. a., „Multi-responsive hydrogel structures from patterned droplet networks“, *Nat. Chem.*, Bd. 12, Nr. 4, S. 363–371, Apr. 2020, doi: 10.1038/s41557-020-0444-1.
- [113] Q. Li, Y. Zhang, C. Wang, D. A. Weitz, und S. Chen, „Versatile Hydrogel Ensembles with Macroscopic Multidimensions“, *Adv. Mater.*, Bd. 30, Nr. 52, S. 1803475, Dez. 2018, doi: 10.1002/adma.201803475.
- [114] V. G. Muir, T. H. Qazi, J. Shan, J. Groll, und J. A. Burdick, „Influence of Microgel Fabrication Technique on Granular Hydrogel Properties“, *ACS Biomater. Sci. Eng.*, Feb. 2021, doi: 10.1021/acsbiomaterials.0c01612.
- [115] S. L. Anna, N. Bontoux, und H. A. Stone, „Formation of dispersions using “flow focusing” in microchannels“, *Appl. Phys. Lett.*, Bd. 82, Nr. 3, S. 364–366, Jan. 2003, doi: 10.1063/1.1537519.
- [116] E. Amstad, M. Chemama, M. Eggersdorfer, L. R. Arriaga, M. P. Brenner, und D. A. Weitz, „Robust scalable high throughput production of monodisperse drops“, *Lab Chip*, Bd. 16, Nr. 21, S. 4163–4172, 2016, doi: 10.1039/C6LC01075J.
- [117] A. G. Håti, T. R. Szymborski, M. Steinacher, und E. Amstad, „Production of monodisperse drops from viscous fluids“, *Lab Chip*, Bd. 18, Nr. 4, S. 648–654, 2018, doi: 10.1039/C7LC01322A.

- [118] J. C. Rose, M. Cámara-Torres, K. Rahimi, J. Köhler, M. Möller, und L. De Laporte, „Nerve Cells Decide to Orient inside an Injectable Hydrogel with Minimal Structural Guidance“, *Nano Lett.*, Bd. 17, Nr. 6, S. 3782–3791, Juni 2017, doi: 10.1021/acs.nanolett.7b01123.
- [119] S. Ma, N. Mukherjee, E. Mikhailova, und H. Bayley, „Gel Microrods for 3D Tissue Printing“, *Adv. Biosys.*, Bd. 1, Nr. 8, S. 1700075, Aug. 2017, doi: 10.1002/adbi.201700075.
- [120] Y. Du, E. Lo, S. Ali, und A. Khademhosseini, „Directed assembly of cell-laden microgels for fabrication of 3D tissue constructs“, *Proceedings of the National Academy of Sciences*, Bd. 105, Nr. 28, S. 9522–9527, Juli 2008, doi: 10.1073/pnas.0801866105.
- [121] F. Xu u. a., „The assembly of cell-encapsulating microscale hydrogels using acoustic waves“, *Biomaterials*, Bd. 32, Nr. 31, S. 7847–7855, Nov. 2011, doi: 10.1016/j.biomaterials.2011.07.010.
- [122] S. Tasoglu, E. Diller, S. Guven, M. Sitti, und U. Demirci, „Untethered micro-robotic coding of three-dimensional material composition“, *Nat Commun*, Bd. 5, Nr. 1, Art. Nr. 1, Jan. 2014, doi: 10.1038/ncomms4124.
- [123] S. E. Chung, W. Park, S. Shin, S. A. Lee, und S. Kwon, „Guided and fluidic self-assembly of microstructures using railed microfluidic channels“, *Nature Mater*, Bd. 7, Nr. 7, Art. Nr. 7, Juli 2008, doi: 10.1038/nmat2208.
- [124] L. Riley, L. Schirmer, und T. Segura, „Granular hydrogels: emergent properties of jammed hydrogel microparticles and their applications in tissue repair and regeneration“, *Current Opinion in Biotechnology*, Bd. 60, S. 1–8, Dez. 2019, doi: 10.1016/j.copbio.2018.11.001.
- [125] M. Hirsch, A. Charlet, und E. Amstad, „3D Printing of Strong and Tough Double Network Granular Hydrogels“, *Advanced Functional Materials*, Bd. 31, Nr. 5, S. 2005929, 2021, doi: 10.1002/adfm.202005929.
- [126] C. B. Highley, K. H. Song, A. C. Daly, und J. A. Burdick, „Jammed Microgel Inks for 3D Printing Applications“, *Advanced Science*, Bd. 6, Nr. 1, S. 1801076, 2019, doi: 10.1002/adv.201801076.
- [127] T. Bhattacharjee u. a., „Writing in the granular gel medium“, *Science Advances*, Bd. 1, Nr. 8, S. 4–10, 2015, doi: 10.1126/sciadv.1500655.
- [128] T. J. Hinton u. a., „Three-dimensional printing of complex biological structures by freeform reversible embedding of suspended hydrogels“, *Sci. Adv.*, Bd. 1, Nr. 9, S. e1500758, Okt. 2015, doi: 10.1126/sciadv.1500758.
- [129] J. Hu, K. Hiwatashi, T. Kurokawa, S. M. Liang, Z. L. Wu, und J. P. Gong, „Microgel-Reinforced Hydrogel Films with High Mechanical Strength and Their Visible Mesoscale Fracture Structure“, *Macromolecules*, Bd. 44, Nr. 19, S. 7775–7781, Okt. 2011, doi: 10.1021/ma2016248.
- [130] J. Saito u. a., „Robust bonding and one-step facile synthesis of tough hydrogels with desirable shape by virtue of the double network structure“, *Polym. Chem.*, Bd. 2, Nr. 3, S. 575–580, Feb. 2011, doi: 10.1039/C0PY00272K.
- [131] J. Hu u. a., „Structure Optimization and Mechanical Model for Microgel-Reinforced Hydrogels with High Strength and Toughness“, *Macromolecules*, Bd. 45, Nr. 12, S. 5218–5228, Juni 2012, doi: 10.1021/ma3003664.
- [132] J. Hu u. a., „High Fracture Efficiency and Stress Concentration Phenomenon for Microgel-Reinforced Hydrogels Based on Double-Network Principle“, *Macromolecules*, Bd. 45, Nr. 23, S. 9445–9451, Dez. 2012, doi: 10.1021/ma301933x.
- [133] L. Ionov, „Biomimetic Hydrogel-Based Actuating Systems“, *Adv. Funct. Mater.*, Bd. 23, Nr. 36, S. 4555–4570, Sep. 2013, doi: 10.1002/adfm.201203692.
- [134] X. Zhang u. a., „The Pathway to Intelligence: Using Stimuli-Responsive Materials as Building Blocks for Constructing Smart and Functional Systems“, *Advanced Materials*, Bd. 31, Nr. 11, S. 1–48, 2019, doi: 10.1002/adma.201804540.
- [135] J. M. McCracken, B. R. Donovan, und T. J. White, „Materials as Machines“, *Advanced Materials*, Bd. 32, Nr. 20, S. 1–48, 2020, doi: 10.1002/adma.201906564.
- [136] M. Sitti, „Physical intelligence as a new paradigm“, *Extreme Mechanics Letters*, Bd. 46, S. 101340, Juli 2021, doi: 10.1016/j.eml.2021.101340.
- [137] P. Calvert, „Hydrogels for Soft Machines“, *Adv. Mater.*, S. 15, 2009.

- [138] X. Liu, J. Liu, S. Lin, und X. Zhao, „Hydrogel machines“, *Materials Today*, Bd. 36, S. 102–124, Juni 2020, doi: 10.1016/j.mattod.2019.12.026.
- [139] S. E. Bakarich, R. Gorkin III, M. in het Panhuis, und G. M. Spinks, „4D Printing with Mechanically Robust, Thermally Actuating Hydrogels“, *Macromolecular Rapid Communications*, Bd. 36, Nr. 12, S. 1211–1217, 2015, doi: 10.1002/marc.201500079.
- [140] X. He u. a., „Synthetic homeostatic materials with chemo-mechano-chemical self-regulation“, *Nature*, Bd. 487, Nr. 7406, S. 214–218, 2012, doi: 10.1038/nature11223.
- [141] H. Warren, M. in het Panhuis, G. M. Spinks, und D. L. Officer, „Thermal actuation of hydrogels from PNIPAm, alginate, and carbon nanofibres“, *Journal of Polymer Science Part B: Polymer Physics*, Bd. 56, Nr. 1, S. 46–52, Jan. 2018, doi: 10.1002/polb.24430.
- [142] Y. Shi, C. Ma, L. Peng, und G. Yu, „Conductive “Smart” Hybrid Hydrogels with PNIPAM and Nanostructured Conductive Polymers“, *Adv. Funct. Mater.*, Bd. 25, Nr. 8, S. 1219–1225, Feb. 2015, doi: 10.1002/adfm.201404247.
- [143] E. Palleau, D. Morales, M. D. Dickey, und O. D. Velev, „Reversible patterning and actuation of hydrogels by electrically assisted ionoprinting“, *Nat Commun*, Bd. 4, Nr. 1, Art. Nr. 1, Aug. 2013, doi: 10.1038/ncomms3257.
- [144] D. J. Beebe u. a., „Functional hydrogel structures for autonomous flow control inside microfluidic channels“, *Nature*, Bd. 404, Nr. 6778, S. 588–590, 2000, doi: 10.1038/35007047.
- [145] H.-W. Huang, F. E. Uslu, P. Katsamba, E. Lauga, M. S. Sakar, und B. J. Nelson, „Adaptive locomotion of artificial microswimmers“, *Sci. Adv.*, Bd. 5, Nr. 1, S. eaau1532, Jan. 2019, doi: 10.1126/sciadv.aau1532.
- [146] H.-W. Huang, M. S. Sakar, A. J. Petruska, S. Pané, und B. J. Nelson, „Soft micromachines with programmable motility and morphology“, *Nat Commun*, Bd. 7, Nr. 1, S. 12263, Nov. 2016, doi: 10.1038/ncomms12263.
- [147] W. J. Zheng, N. An, J. H. Yang, J. Zhou, und Y. M. Chen, „Tough Al-alginate/Poly(N-isopropylacrylamide) Hydrogel with Tunable LCST for Soft Robotics“, *ACS Appl. Mater. Interfaces*, Bd. 7, Nr. 3, S. 1758–1764, Jan. 2015, doi: 10.1021/am507339r.
- [148] M. Cianchetti, C. Laschi, A. Menciassi, und P. Dario, „Biomedical applications of soft robotics“, *Nat Rev Mater*, Bd. 3, Nr. 6, Art. Nr. 6, Juni 2018, doi: 10.1038/s41578-018-0022-y.
- [149] W. Sun, S. Schaffer, K. Dai, L. Yao, A. Feinberg, und V. Webster-Wood, „3D Printing Hydrogel-Based Soft and Biohybrid Actuators: A Mini-Review on Fabrication Techniques, Applications, and Challenges“, *Frontiers in Robotics and AI*, Bd. 8, 2021, Zugegriffen: 13. Juni 2022. [Online]. Verfügbar unter: <https://www.frontiersin.org/article/10.3389/frobt.2021.673533>
- [150] S. Fusco u. a., „An Integrated Microrobotic Platform for On-Demand, Targeted Therapeutic Interventions“, *Adv. Mater.*, Bd. 26, Nr. 6, S. 952–957, Feb. 2014, doi: 10.1002/adma.201304098.
- [151] H. Yuk, B. Lu, und X. Zhao, „Hydrogel bioelectronics“, *Chem. Soc. Rev.*, Bd. 48, Nr. 6, S. 1642–1667, März 2019, doi: 10.1039/C8CS00595H.
- [152] F. Fu, J. Wang, H. Zeng, und J. Yu, „Functional Conductive Hydrogels for Bioelectronics“, *ACS Materials Lett.*, Bd. 2, Nr. 10, S. 1287–1301, Okt. 2020, doi: 10.1021/acsmaterialslett.0c00309.
- [153] H. Yuk u. a., „Dry double-sided tape for adhesion of wet tissues and devices“, *Nature*, Bd. 575, Nr. 7781, Art. Nr. 7781, Nov. 2019, doi: 10.1038/s41586-019-1710-5.
- [154] J. Kim, G. Zhang, M. Shi, und Z. Suo, „Fracture, fatigue, and friction of polymers in which entanglements greatly outnumber cross-links“, *Science*, Okt. 2021, doi: 10.1126/science.abg6320.
- [155] J. Hu, T. Kurokawa, T. Nakajima, Z. L. Wu, S. M. Liang, und J. P. Gong, „Fracture Process of Microgel-Reinforced Hydrogels under Uniaxial Tension“, *Macromolecules*, Bd. 47, Nr. 11, S. 3587–3594, Juni 2014, doi: 10.1021/ma5008545.
- [156] C. S. Wyss, P. Karami, P.-E. Bourban, und D. P. Pioletti, „Hybrid granular hydrogels: combining composites and microgels for extended ranges of material properties“, *Soft Matter*, Bd. 16, Nr. 15, S. 3769–3778, 2020, doi: 10.1039/D0SM00213E.
- [157] C. Li u. a., „Tough hybrid microgel-reinforced hydrogels dependent on the size and modulus of the microgels“, *Soft Matter*, Bd. 17, Nr. 6, S. 1566–1573, Feb. 2021, doi: 10.1039/D0SM01703E.

- [158] R. Takahashi u. a., „Tough Particle-Based Double Network Hydrogels for Functional Solid Surface Coatings“, *Advanced Materials Interfaces*, Bd. 5, Nr. 23, S. 1801018, 2018, doi: 10.1002/admi.201801018.
- [159] A. J. Gravelle, R. A. Nicholson, S. Barbut, und A. G. Marangoni, „Considerations for readdressing theoretical descriptions of particle-reinforced composite food gels“, *Food Research International*, Bd. 122, S. 209–221, Aug. 2019, doi: 10.1016/j.foodres.2019.03.070.
- [160] S. Xin u. a., „Generalizing hydrogel microparticles into a new class of bioinks for extrusion bioprinting“, *Science Advances*, Bd. 7, Nr. 42, S. eabk3087, 2021, doi: 10.1126/sciadv.abk3087.
- [161] K. Sklodowska und S. Jakiela, „Enhancement of bacterial growth with the help of immiscible oxygenated oils“, *RSC Adv.*, Bd. 7, Nr. 65, S. 40990–40995, Aug. 2017, doi: 10.1039/C7RA07095K.
- [162] K. Krutkramelis, B. Xia, und J. Oakey, „Monodisperse polyethylene glycol diacrylate hydrogel microsphere formation by oxygen-controlled photopolymerization in a microfluidic device“, *Lab Chip*, Bd. 16, Nr. 8, S. 1457–1465, Apr. 2016, doi: 10.1039/C6LC00254D.
- [163] M. Kessler, Q. Nassisi, und E. Amstad, „Does the Size of Microgels Influence the Toughness of Microgel-Reinforced Hydrogels?“, *Macromolecular Rapid Communications*, Bd. n/a, Nr. n/a, S. 2200196, doi: 10.1002/marc.202200196.
- [164] I. L. H. Ong und E. Amstad, „Selectively Permeable Double Emulsions“, *Small*, Bd. 15, Nr. 44, S. 1903054, 2019, doi: <https://doi.org/10.1002/smll.201903054>.
- [165] P. F. Luckham und M. A. Ukeje, „Effect of Particle Size Distribution on the Rheology of Dispersed Systems“, *Journal of Colloid and Interface Science*, Bd. 220, Nr. 2, S. 347–356, Dez. 1999, doi: 10.1006/jcis.1999.6515.
- [166] C. B. Highley, K. H. Song, A. C. Daly, und J. A. Burdick, „Jammed Microgel Inks for 3D Printing Applications“, *Advanced Science*, Bd. 6, Nr. 1, S. 1801076, 2019, doi: 10.1002/adv.201801076.
- [167] L. R. G. Treloar, *The physics of rubber elasticity: by L.R.G. Treloar*, 3rd ed. Oxford : New York: Clarendon Press ; Oxford University Press, 2005.
- [168] P. J. Flory, *Principles of polymer chemistry*. Cornell university press, 1953.
- [169] K. Hoshino, T. Nakajima, T. Matsuda, T. Sakai, und J. Ping Gong, „Network elasticity of a model hydrogel as a function of swelling ratio: from shrinking to extreme swelling states“, *Soft Matter*, Bd. 14, Nr. 47, S. 9693–9701, 2018, doi: 10.1039/C8SM01854E.
- [170] M. C. Boyce und E. M. Arruda, „Constitutive Models of Rubber Elasticity: A Review“, *Rubber Chemistry and Technology*, Bd. 73, Nr. 3, S. 504–523, Juli 2000, doi: 10.5254/1.3547602.
- [171] Y. Akagi, H. Sakurai, J. P. Gong, U. Chung, und T. Sakai, „Fracture energy of polymer gels with controlled network structures“, *The Journal of Chemical Physics*, Bd. 139, Nr. 14, S. 144905, Okt. 2013, doi: 10.1063/1.4823834.
- [172] E. Ducrot und C. Creton, „Characterizing Large Strain Elasticity of Brittle Elastomeric Networks by Embedding Them in a Soft Extensible Matrix“, *Advanced Functional Materials*, Bd. 26, Nr. 15, S. 2482–2492, 2016, doi: 10.1002/adfm.201504536.
- [173] T. Matsuda, R. Kawakami, T. Nakajima, und J. P. Gong, „Crack Tip Field of a Double-Network Gel: Visualization of Covalent Bond Scission through Mechanoradical Polymerization“, *Macromolecules*, Bd. 53, Nr. 20, S. 8787–8795, Okt. 2020, doi: 10.1021/acs.macromol.0c01485.
- [174] M. Hirsch, A. Charlet, und E. Amstad, „3D Printing of Strong and Tough Double Network Granular Hydrogels“, *Adv. Funct. Mater.*, S. 2005929, Okt. 2020, doi: 10.1002/adfm.202005929.
- [175] T. Matsuda u. a., „Yielding Criteria of Double Network Hydrogels“, *Macromolecules*, Bd. 49, Nr. 5, S. 1865–1872, März 2016, doi: 10.1021/acs.macromol.5b02592.
- [176] D. R. King u. a., „Extremely tough composites from fabric reinforced polyampholyte hydrogels“, *Mater. Horiz.*, Bd. 2, Nr. 6, S. 584–591, Okt. 2015, doi: 10.1039/C5MH00127G.
- [177] A. J. Gravelle, S. Barbut, und A. G. Marangoni, „Influence of particle size and interfacial interactions on the physical and mechanical properties of particle-filled myofibrillar protein gels“, *RSC Advances*, Bd. 5, Nr. 75, S. 60723–60735, 2015, doi: 10.1039/C5RA07254A.
- [178] T. Zhang, S. Lin, H. Yuk, und X. Zhao, „Predicting fracture energies and crack-tip fields of soft tough materials“, *Extreme Mechanics Letters*, Bd. 4, S. 1–8, Sep. 2015, doi: 10.1016/j.eml.2015.07.007.

- [179] L. V. Zuccarello, „Ultrastructural and cytochemical study on the enzyme gland of the foot of a mollusc“, *Tissue and Cell*, Bd. 13, Nr. 4, S. 701–713, 1981, doi: 10.1016/S0040-8166(81)80007-9.
- [180] Y. Hu u. a., „Botanical-Inspired 4D Printing of Hydrogel at the Microscale“, *Advanced Functional Materials*, Bd. 30, Nr. 4, S. 1907377, Jan. 2020, doi: 10.1002/adfm.201907377.
- [181] P. Kunwar u. a., „High-Resolution 3D Printing of Stretchable Hydrogel Structures Using Optical Projection Lithography“, *ACS Applied Materials and Interfaces*, Bd. 12, Nr. 1, S. 1640–1649, Jan. 2020, doi: 10.1021/acsami.9b19431.
- [182] W. Liu u. a., „Rapid Continuous Multimaterial Extrusion Bioprinting“, *Advanced Materials*, Bd. 29, Nr. 3, S. 1–8, 2017, doi: 10.1002/adma.201604630.
- [183] T. J. Hinton u. a., „Three-dimensional printing of complex biological structures by freeform reversible embedding of suspended hydrogels“, *Science Advances*, Bd. 1, Nr. 9, 2015, doi: 10.1126/sciadv.1500758.
- [184] C. B. Highley, C. B. Rodell, und J. A. Burdick, „Direct 3D Printing of Shear-Thinning Hydrogels into Self-Healing Hydrogels“, *Advanced Materials*, Bd. 27, Nr. 34, S. 5075–5079, 2015, doi: 10.1002/adma.201501234.
- [185] L. Ouyang, C. B. Highley, W. Sun, und J. A. Burdick, „A Generalizable Strategy for the 3D Bioprinting of Hydrogels from Nonviscous Photo-crosslinkable Inks“, *Advanced Materials*, Bd. 29, Nr. 8, 2017, doi: 10.1002/adma.201604983.
- [186] A. Fornell, C. Johannesson, S. S. Searle, A. Happstadius, J. Nilsson, und M. Tenje, „An acoustofluidic platform for non-contact trapping of cell-laden hydrogel droplets compatible with optical microscopy“, *Biomicrofluidics*, Bd. 13, Nr. 4, S. 044101, 2019, doi: 10.1063/1.5108583.
- [187] R. De Ruiter, A. M. Pit, V. M. De Oliveira, M. H. G. Duits, D. Van Den Ende, und F. Mugele, „Electrostatic potential wells for on-demand drop manipulation in microchannels“, *Lab on a Chip*, Bd. 14, Nr. 5, S. 883–891, 2014, doi: 10.1039/c3lc51121a.
- [188] A. M. Pit, M. H. G. Duits, und F. Mugele, „Droplet manipulations in two phase flow microfluidics“, *Micromachines*, Bd. 6, Nr. 11, S. 1768–1793, 2015, doi: 10.3390/mi6111455.
- [189] P. Abbyad, R. Dangla, A. Alexandrou, und C. N. Baroud, „Rails and anchors: guiding and trapping droplet microreactors in two dimensions“, *Lab on a Chip*, Bd. 11, Nr. 5, S. 813–821, 2011, doi: 10.1039/C0LC00104J.
- [190] E. Fradet, C. McDougall, P. Abbyad, R. Dangla, D. McGloin, und C. N. Baroud, „Combining rails and anchors with laser forcing for selective manipulation within 2D droplet arrays“, *Lab on a Chip*, Bd. 11, Nr. 24, S. 4228, 2011, doi: 10.1039/c1lc20541b.
- [191] S. Sart, R. F. X. Tomasi, G. Amselem, und C. N. Baroud, „Multiscale cytometry and regulation of 3D cell cultures on a chip“, *Nature Communications*, Bd. 8, Nr. 1, 2017, doi: 10.1038/s41467-017-00475-x.
- [192] G. Etienne, A. Vian, M. Biočanin, B. Deplancke, und E. Amstad, „Cross-talk between emulsion drops: How are hydrophilic reagents transported across oil phases?“, *Lab on a Chip*, Bd. 18, Nr. 24, S. 3903–3912, 2018, doi: 10.1039/c8lc01000e.
- [193] P. Gruner u. a., „Controlling molecular transport in minimal emulsions“, *Nature Communications*, Bd. 7, Nr. January, 2016, doi: 10.1038/ncomms10392.
- [194] Y. Xia und G. Whitesides, „Soft lithography“, *Annual Review of Materials Science*, Bd. 28, Nr. 12, S. 153–184, 1998, doi: 10.1146/annurev.matsci.28.1.153.
- [195] S. L. Anna, N. Bontoux, und H. A. Stone, „Formation of dispersions using ‘flow focusing’ in microchannels“, *Applied Physics Letters*, Bd. 82, Nr. 3, S. 364–366, 2003, doi: 10.1063/1.1537519.
- [196] G. Etienne, M. Kessler, und E. Amstad, „Influence of Fluorinated Surfactant Composition on the Stability of Emulsion Drops“, *Macromolecular Chemistry and Physics*, S. 1–10, 2016, doi: 10.1002/macp.201600365.
- [197] K. A. Brakke, „The surface evolver“, *Experimental Mathematics*, Bd. 1, Nr. 2, S. 141–165, 1992, doi: 10.1080/10586458.1992.10504253.
- [198] M. Kessler u. a., „Everything in its right place: controlling the local composition of hydrogels using microfluidic traps“, *Lab Chip*, Bd. 20, Nr. 24, S. 4572–4581, Dez. 2020, doi: 10.1039/D0LC00691B.

- [199] R. Dangla, S. Lee, und C. N. Baroud, „Trapping microfluidic drops in wells of surface energy“, *Physical Review Letters*, Bd. 107, Nr. 12, S. 1–4, 2011, doi: 10.1103/PhysRevLett.107.124501.
- [200] C. W. Park und G. M. Homsy, „Two-Phase displacement in hele shaw cells: theory“, *Journal of Fluid Mechanics*, Bd. 139, S. 291–308, 1984, doi: 10.1017/S0022112084001725.
- [201] R. Dangla, S. C. Kayi, und C. N. Baroud, „Droplet microfluidics driven by gradients of confinement“, *Proceedings of the National Academy of Sciences*, Bd. 110, Nr. 3, S. 853–858, 2013, doi: 10.1073/pnas.1209186110.
- [202] M. Nagel, P. T. Brun, und F. Gallaire, „A numerical study of droplet trapping in microfluidic devices“, *Physics of Fluids*, Bd. 26, Nr. 3, 2014, doi: 10.1063/1.4867251.
- [203] C. Lv, „Effects of geometric confinement on a droplet between two parallel planes“, S. 1–21, 2017.
- [204] Z. Nie u. a., „Emulsification in a microfluidic flow-focusing device: Effect of the viscosities of the liquids“, *Microfluidics and Nanofluidics*, Bd. 5, Nr. 5, S. 585–594, 2008, doi: 10.1007/s10404-008-0271-y.